2021

A Framework for the Design and Characterization of Advanced Gaskets

Sannmit Shinde
University of Central Florida

A FRAMEWORK FOR THE DESIGN AND CHARACTERIZATION OF ADVANCED GASKETS

by

SANNMIT SHINDE
B.S. University of Central Florida, 2020

A thesis submitted in partial fulfillment of the requirements
for the degree of Master of Science
in the Department of Mechanical and Aerospace Engineering
in the College of Engineering and Computer Science
at the University of Central Florida
Orlando, Florida

Fall Term
2021

Major Professor: Ali P. Gordon

ABSTRACT

Most industrial manufacturing or processing plants use bolted connections between pipes that transfer media from one location to another. Gaskets are often used to seal these systems as they offer elevated levels of leak mitigation; however, despite their nearly universal usage, the current understanding of gasket mechanics at the meso-scale is still limited. Contemporary gaskets feature viscoelastic materials, fillers, textures, and are fabricated at various thicknesses. They are used in a wide range of thermal, mechanical, chemical, and temporal conditions. The current work characterizes polytetrafluoroethylene (PTFE) gaskets made with several different filler materials and having vastly different geometries. The chemically inert properties of this material and its relatively superior load retention properties make it appropriate for use in gaskets that are expected to retain load over hundreds of hours. As the degree to which certain factors influence gasket performance is still relatively unknown, several Analysis of Variance (ANOVA) studies are conducted to discover to what extent certain factors influence gasket load retention. Using a novel efficiency parameter (η) that compares experimental behavior to the behavior of an ideal gasket, these studies describe the impact of factors such as gasket texture, thickness, filler material, flange temperature, and the internal pressure of the flange. Additionally, component scale gasket behavior during service conditions is investigated via Finite Element Modeling. This model simulates the viscoelastic load retention behavior of these gaskets with a high degree of accuracy by using a Prony series approximation of Burger's model to characterize the viscoelastic properties of the material. A material database is used to verify and correct the model using experimental data. This collection contains data from gaskets of various textures, thicknesses and filler materials. Parameters for this model are obtained by using

regression fits on a large number of data sets in the database and averaging the values of the parameters across the multiple tests. The collection of these research activities establishes a new framework that future engineers may use to characterize and even design new gaskets.

ACKNOWLEDGEMENTS

I would like to thank my mentor Dr. Ali P. Gordon for his support and guidance in this research project and many others. I am also grateful to the other members of my committee, Dr. Georgios Apostolakis and Dr. Jihua Gou, for their time and advice.

I would also like to thank the other members of the Mechanics of Materials Research Group who helped perform the experiments listed in this thesis.

Finally, I would also like to thank my family for their continued support during my academic career.

TABLE OF CONTENTS

LIST OF FIGURES

LIST OF TABLES

CHAPTER 1 INTRODUCTION

Most industries depend on gaskets to seal and enhance the overall effectiveness of joints in their pipelines. Oil and gas plants, chemical manufacturers, power stations, food and beverage producers, as well as many others all depend on proper gasket application to efficiently transfer media across various lengths of interconnected pipelines. To maximize the benefits of gasket usage, proper torquing and gasket selection techniques need to be used. Figure 1 shows a simple schematic of an ideal gasketed flange.

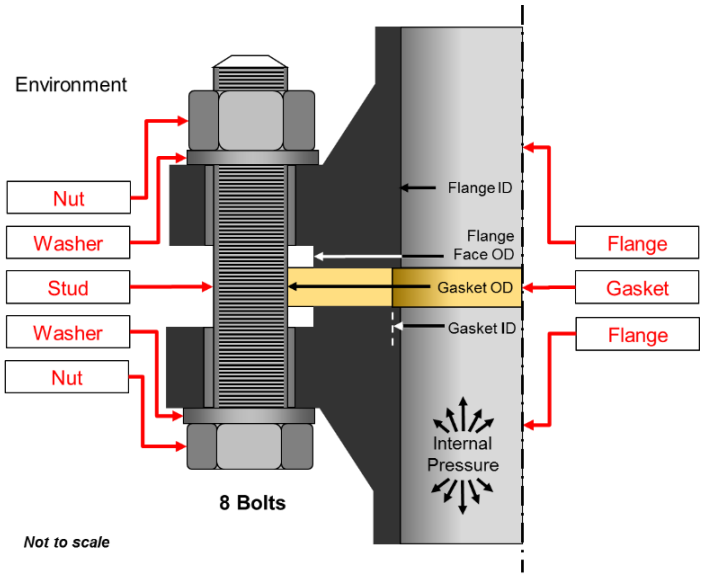

Figure 1: Gasketed Flange Profile

A gasket's primary purpose is maintaining a tight seal throughout its service, including during periods when it is exposed to extreme temperatures and high pressures. Since many commercially available gaskets display viscoelastic behavior, most gasketed flanges experience some creep relaxation and load loss over their lifetimes. When a gasket is first placed into service, it is fully compressed so as to conform to all of the microscopic imperfections in the flange surface and create a tight seal. However, as time passes, the

gaskets, bolts, and flanges start to relax and reduce the compressive load on the gasket. In most cases, the gaskets that achieve optimal performance are those that display a balance of time-dependent behavior and a high level of strength across a range of internal pressures and temperatures. As such, two of the most important properties of gaskets are conformability and load retention. Conformability is a measure of how well a gasket will conform to the flange faces and load retention is the ability of the gasket to maintain the initially applied load over a long period. Standardized mechanical test protocols, described in [1] and [2], are used to quantify these properties.

The current work focuses on using statistical and finite element methods to characterize the overall performance of gaskets. As many processes in various industries rely on gaskets to create proper seals, it is essential to be able to predict the behavior of gasket materials under various conditions. To that end, the majority of this work focuses on describing the behavior of various PTFE gaskets at several different temperatures and pressures. An explanation of various concepts, such as the statistical methods used in this case study, as well as a breakdown of the prior studies in this area are provided in Chapter 2. Chapter 3 describes the procedures and outcomes of some of the preliminary studies that served as a basis for the current series of experiments. Chapter 4 describes the motivations and approach behind the current series of experiments, while Chapter 5 contains the results of these experiments. Chapter 6 deals with the data analysis and describes the results of that analysis. Meanwhile the attempts at modeling gasket behavior using Finite Element Methods are described in Chapter 7. Finally, Chapter 8 presents the conclusions of this work, as well as avenues for further study.

CHAPTER 2 BACKGROUND

2.1 Mechanics of Bolted Connections

As this thesis discusses the performance of certain elements of bolted gasketed flanges, it is first imperative to understand the principles behind their operation. As such this chapter will cover the principles behind the mechanics of gasketed flanges, the gasket materials used in this study, some of the constitutive modeling methods for viscoelastic materials, the modeling efforts that have been conducted so far, and conclude with a discussion of the statistical methods used in this thesis.

The purpose of a bolted joint is to create a clamping force between two or more objects, called joint members, to be able to resist shear and tensile forces acting on the joint. As the vast majority of gasketed flanges deal with joints loaded in tension, this section will focus on the mechanics of tensile joints. A sketch of a gasketed tensile joint is shown in Fig. 2.

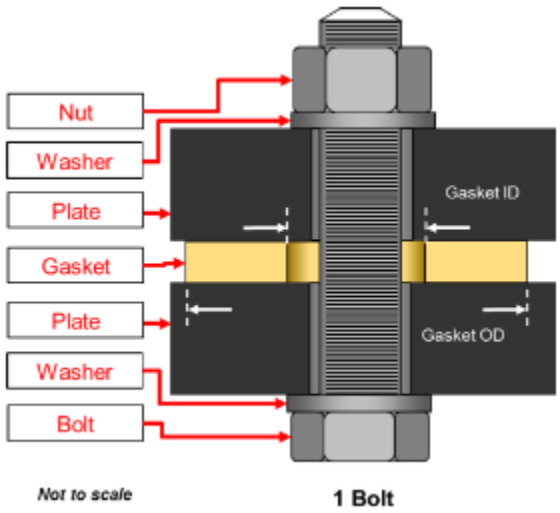

Figure 2: Sketch of an ideal gasketed joint

In tensile joints, it is imperative that the bolts should clamp the joint members together with enough force to prevent them from separating and thus leaking the contents of the pipe. The tension in the bolts must also be high enough to prevent the bolt from loosening as it undergoes cycles of vibrations, shocks, or changes in temperature. To this end, it is generally advisable to load a tensile joint so that it exerts as much force as the bolt and joint members can stand [3].

Bolted joints can retain loads because all of the materials act like a series of stiff springs, with the bolts in tension and the joint members acting in compression. A representation of this behavior is shown in Fig. 3.

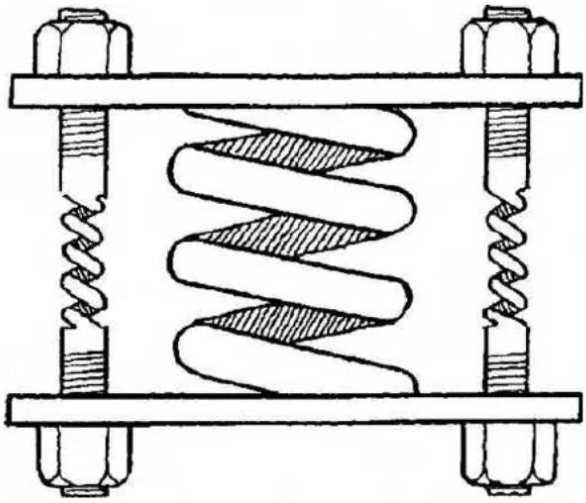

Figure 3: Representation of elastic material behavior.

Due to the spring-like properties of the joint members and bolts, the elements are able to store potential energy. If the bolts and members were released just after tightening, they would quickly return to their original dimensions. However, as the energy is stored in the flange elements, it allows the joint to maintain the clamping force between joint members and thus form a proper seal.

2.2 Materials

Several different types of Polytetrafluoroethylene (PTFE) based gaskets are presented in this study. These materials, including silica-filled (tan), barium-sulfate filled (white), and aluminosilicate microsphere-filled (blue) PTFE, referred to by the manufacturer as 3500, 3510, and 3504 respectively, have become standard in the industry as they exhibit superior load retention behavior while retaining desirable sealability and the chemical resistance properties of PTFE. Silica and barium sulfate particles in PTFE composites help maximize load retention, while the addition of glass microspheres in PTFE offers improved compressibility and lowers sealability requirements.

There are also three different gasket styles that were tested. Traditional flat gaskets with thicknesses of 1/8” and 1/16” were compared to a novel textured gasket with a honeycomb pattern. The gasket style with 1/8” thickness offers improved compressibility at the expense of load retention and 1/16” displays improved load retention and sealability at the expense of compressibility. The textured styles incorporate a fully connected prominent hexagonal (or honeycomb) structure elevated from the flat face of the gasket. These textured gaskets offer similar levels of load retention to the thinner gaskets while requiring less force to seal. The materials used in this study are listed in Table 1 and cross sections of various gaskets are shown in Figure 4.

Table 1: Candidate Gasket Materials

Material Composition	*Texture*	*Thickness (in)*
Silica Filled PTFE Composite	Flat	1/8”
Silica Filled PTFE Composite	Flat	1/16”
Silica Filled PTFE Composite	Textured	3/32”
Glass Microsphere Filled PTFE Composite	Flat	1/8”
Glass Microsphere Filled PTFE Composite	Flat	1/16”
Glass Microsphere Filled PTFE Composite	Textured	3/32”
Barium Sulfate Filled PTFE Composite	Flat	1/8”
Barium Sulfate Filled PTFE Composite	Flat	1/16”
Barium Sulfate Filled PTFE Composite	Textured	3/32”

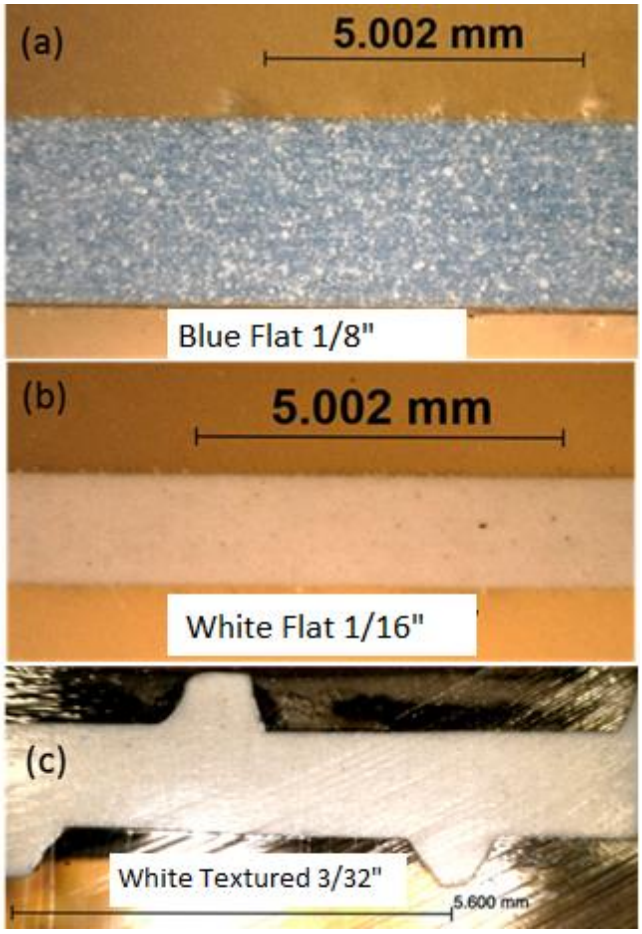

Figure 4: Cross-sections of the particle-reinforced gasket materials used in the study. (a) Glass microsphere filled (Blue, 3504) flat PTFE gasket with a thickness of 1/8”, (b) Barium sulfate filled (White, 3510) flat PTFE gasket with a thickness of 1/16”, (c) Barium sulfate filled (White, 3510) textured PTFE gasket with a thickness of 3/32”

Another important property of gaskets is the minimum compressive stresses needed to maintain a seal, termed sealability. These values are provided in Table 2 for each gasket product. It should be noted that while sealability has been determined for various gasket styles and internal pressures, a sealability study of these gaskets at different temperatures has not yet been conducted. The table shows that increasing the internal pressure of a flange leads to increased compressive stress requirements for the gasket and that in most cases, the force required to seal textured gaskets is 45% of the analogous Legacy material.

Table 2: Sealability Requirements

Sealability requirements (ID= 50mm OD= 90mm)

	Style					
	Textured		1/8”		1/16”	
Material	Stress (psi)	Force (lbs.)	Stress (psi)	Force (lbs.)	Stress (psi)	Force (lbs.)
Blue	800	5453	9600	65443	8000	54536
White	700	4771	2500	17042	2100	14315
Tan	900	6135	8600	58626	6200	42265

2.3 Constitutive Modeling

There are 4 main constitutive models that can be used to model viscoelastic gasket behavior. These are the Maxwell, Voigt (Kelvin), Linear and Burger models. The maxwell model attempts to mimic viscoelastic behavior using a purely viscous damper and an elastic spring connected in series. The setup is shown in Figure 5.

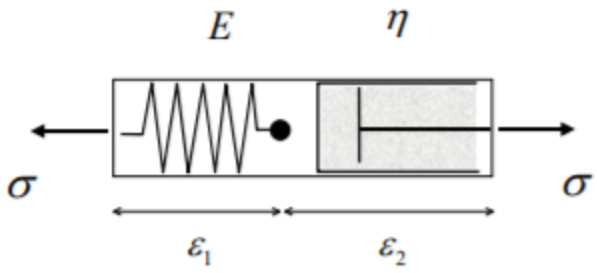

Figure 5: Representation of Maxwell's model [4]

In this model, the total strain is split up into two separate strains (one for the spring and one for the dashpot) which are considered individually. Using Hooke's law and some mathematical processes such as Laplace transforms and differentiation, a relationship between the applied stress and the total strain can be derived, i.e.,

$$\sigma + \frac{\eta}{E}\dot{\sigma} = \eta\dot{\varepsilon} \tag{1}$$

Here, σ represents the applied stress, η is the damping coefficient, E is young's modulus, $\dot{\sigma}$ is the rate of change of the stress, and $\dot{\varepsilon}$ represents the rate of change of the strain. Using this equation, a reaction to a sudden load can be predicted and the time dependent behavior of the material can be approximated. However, this method does yield a more linear load curve than most materials experience during compression, which is why other methods were created to try to describe this behavior.

The second model common to viscoelastic solids is the Kelvin model. This model also uses a single spring-dashpot system to approximate viscoelastic behavior, but instead of having the elements in series, they are placed in parallel. A visualization of the model is shown in Fig. 6.

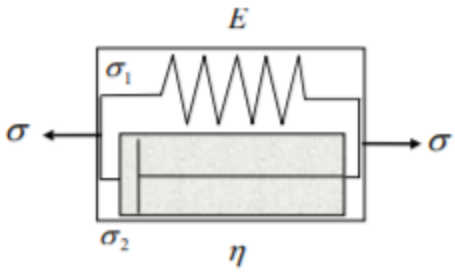

Figure 6: Representation of the Kelvin model

The model assumes that there is no bending, so the strain experienced by the spring is always the same as that experienced by the dashpot. However, this does not necessarily mean that the stresses in both elements are equal. Again, by using a combination of Hooke's law and some mathematical reorganization, the constitutive law for this model can be defined as

$$\sigma = E\varepsilon + \eta\dot{\varepsilon} \tag{2}$$

This model produces a less linear response than that of the Maxwell model, allowing for the modeling of transient-type creep and anelastic recovery. However, instantaneous and permanent strain is not captured by this model. Hence, two other models have been developed to remedy this.

The standard linear model is a modified version of the Kelvin model. This model is the most realistic model of those discussed so far and consists of a spring in series with a kelvin unit (the spring and dashpot setup shown in Fig. 6). A representation of the standard linear model is shown in Fig. 7.

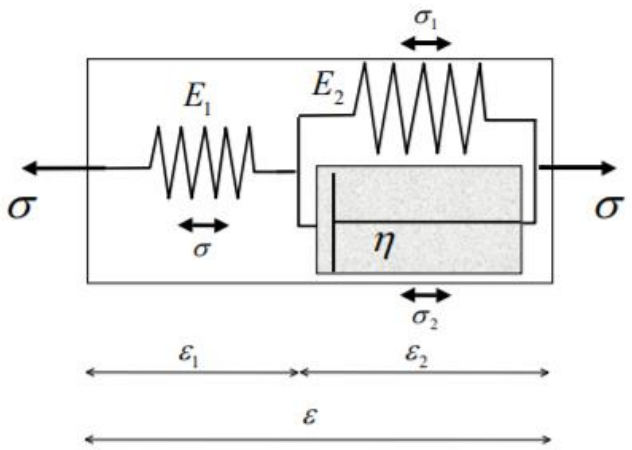

Figure 7: Representation of the Standard Linear model of viscoelasticity

This model assumes that there is no bending in the system, either between the solitary spring and the Kelvin unit, or between the Kelvin spring and dashpot. Upon encountering a stress, the spring will stretch immediately, with the kelvin unit taking longer to respond due to the influence of the dashpot. This same pattern is seen upon unloading as the spring relaxes almost immediately while the Kelvin unit taking longer to contract. By using the boundary conditions, Hooke's law, and some mathematical manipulation, the constitutive equation can be derived, i.e.,

$$\sigma + \frac{\eta}{E_1+E_2}\dot{\sigma} = \frac{E_1E_2}{E_1+E_2}\varepsilon + \frac{E_1\eta}{E_1+E_2} \tag{3}$$

As expected, the new constitutive equation is more complex than either of the previous versions. However, this increased complexity does yield increased accuracy. This model closely mimics the behavior of a real material. During the loading and unloading steps, the model closely mimics the shape of the load curve, meaning the time dependent load behavior is fully captured. However, this model still does not capture the permanent strain most materials experience. To fully capture this behavior, Burger's method is required.

The final and most comprehensive model is Burger's model. This model combines both Kelvin and Maxwell units in order to create an approximation of viscoelastic behavior. Broadly speaking, these units are combined in one of two ways: the Maxwell or Kelvin representation. Visualizations of both arrangements are shown in Fig. 8.

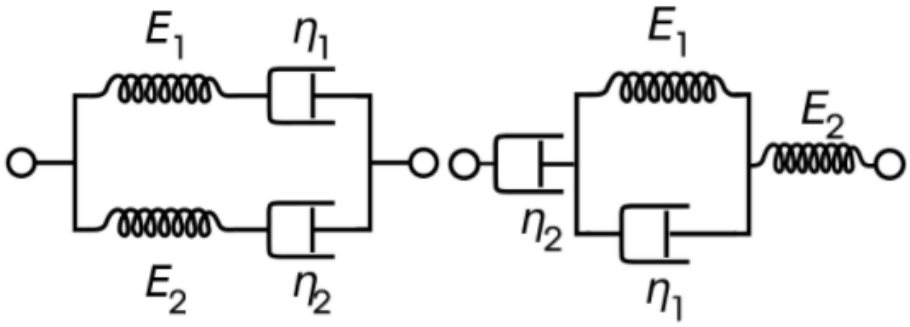

Figure 8: Maxwell (left) and Kelvin (right) representations of Burger's model

The Maxwell arrangement consists of two maxwell units connected in parallel while the Kelvin representation has a single Kelvin unit sandwiched between the spring and dashpot of a Maxwell unit. As with all of the other models discussed so far, Burger's model assumes that there is no bending present in the system as the springs and dashpots arranged in parallel experience the same strain [4]. Using the boundary conditions and the generalized elasticity equation, constitutive equations for both representations can be derived as

$$\sigma + \left(\frac{\eta_1}{E_1} + \frac{\eta_2}{E_2}\right)\dot{\sigma} + \frac{\eta_1\eta_2}{E_1E_2}\ddot{\sigma} = (\eta_1 + \eta_2)\dot{\varepsilon} + \frac{\eta_1\eta_2(E_1+E_2)}{E_1E_2}\ddot{\varepsilon} \tag{4}$$

or

$$\sigma + \left(\frac{\eta_1}{E_1} + \frac{\eta_2}{E_2} + \frac{\eta_2}{E_1}\right)\dot{\sigma} + \frac{\eta_1\eta_2}{E_1E_2}\ddot{\sigma} = \eta_2\dot{\varepsilon} + \frac{\eta_1\eta_2}{E_1}\ddot{\varepsilon} \tag{5}$$

These equations are more complex than that of the standard linear model, but they capture all aspects of viscoelastic behavior. The load relaxation curves for this model are more accurate

than those of any other, and this model does manage to capture the permanent strain behavior that most real materials exhibit. For that reason, despite its relative computational intensity, Burger's model will be used to create the gasket model discussed in Chapter 7. Prior studies have already calculated some of the material constants for PTFE based on the Kelvin representation of Burger's model, which are as follows. E_1, the elastic modulus for the spring inside the Kelvin unit has a value of 12.94 N/mm while E_2 the spring associated with the Maxwell unit, has a value of 4.435 N/mm. As for the damping coefficients, η_1 has a value of 20506 N-s/mm, while η_2 has a value of 1016 N-s/mm. These values will help develop some of the viscoelastic constants for the model presented in this thesis.

2.4 Modeling of PTFE-based Materials

In order to develop the modeling methods discussed in Sections 7.2 and 7.3 it was necessary to first understand the methods and limitations of previous modeling approaches. As of writing, several models have been produced that attempt to simulate the behavior of PTFE under several different conditions. Table 3 presents different modeling approaches from recent years. Each approach was developed for different materials and conditions as shown. The limitations of each method are presented as well.

One of the earliest attempts at modeling gasket behavior came from Alkelani and his colleagues (2008), who used MATLAB to find the relaxation coefficients of the power-law creep model for use with styrene butadiene rubber gaskets. The limitations of this approach were that while the model was versatile in predicting both clamp loads and gasket deformations, it required a great deal of computational power and often produced results that were higher than the experimental values. As such, different approaches were developed to rectify these issues.

Table 3: Review of modeling approaches

Author, Year	Material	Experiment	Modeling	Limitations
Alkelani et al., 2008 [5]	Styrene-butadiene rubber gasket sample	Applied force to gasket and observed deformation	Modeled gasket behavior using power-law creep model directly	Modeled stresses were higher than experimental results
Stan & Fetecau, 2013 [6]	Rectangular PTFE samples with varying amounts of additives	Carried out macro-indentation tests on rectangular PTFE samples	Used Prony series approximation of power-law creep model to simulate relaxation behavior	Only modeled relaxation behavior
Williams et al., 2015 [7]	PTFE composite fiberglass reinforced gasket	Initial torque and relaxation followed by re-torque	Used a two-step process in FORTRAN to model loading, unloading and re-torque behavior	Very computationally intensive
Bharadwaj et al., 2017 [8]	Pure PTFE gasket	Applied initial deformation followed by material relaxation	Used Prony Series approximation of Burger's model to model relaxation behavior	Did not include loading step in model, model was inaccurate near middle of test duration

The next model was developed by the team of Stan and Fetecau (2013), who used a Prony series approximation of the power-law creep model to simulate the relaxation behavior of macro-indented PTFE samples. This was the first approach that modeled the viscoelastic behavior of PTFE materials using a Prony series approximation and served as the foundation of some of the later approaches. The limitations of this study were that the models for the loading and unloading behavior were separated, and that the model for the loading behavior was somewhat inaccurate. Their approach was then built on by Bharadwaj and his colleagues (2017) who used a Prony series approximation of Burger's model in an attempt to fully

model the relaxation behavior of gaskets. However, this model fell prey to the same limitations that plagued the model of Stan and Fetecau in that the models for the loading and unloading steps were separated. In addition, the model became somewhat inaccurate towards the middle of the simulation.

The final model was developed by Williams (2015), who used a two-step approach in NASTRAN to capture the loading, unloading, and re-torque behavior of PTFE gaskets. This model used Burgers' method directly, and while this resolved may of the issues of the other models faced, it also made the model far more computationally intensive than its counterparts.

2.5 Efficiency Parameter

One of the primary goals of this series of experiments was to compare the load retention behavior of different types of gaskets under a variety of different conditions. As such, it was necessary to define a parameter that quantified the overall performance of a gasket product by incorporating measures of load retention and sealability. As such, it was important to take measures from load relaxation curves in order to create a parameter that could capture all of these characteristics. These measures include the maximum force achieved upon torque application, F_{max}, the sealability of the gasket product F_s, the test duration t_d, and the force at any given time during the test F(t). A sample force relaxation curve, with all of the quantities labeled, can be found in Fig 9.

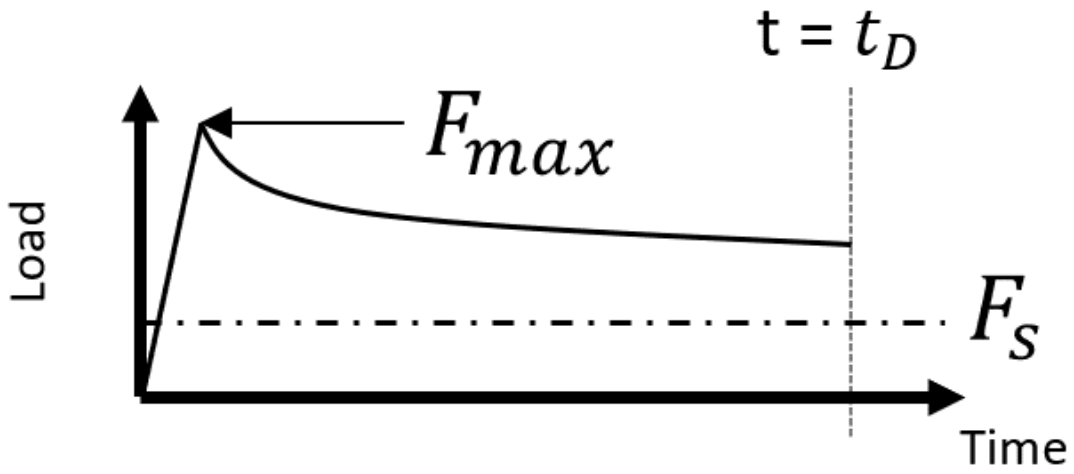

Figure 9: Sample relaxation curve

Here, F_{max} is the maximum load experienced by the gasket which in this case would be about 13000 lbs. F_s is the sealability force at 4000 lbs, and t_d is the test duration at 72000 seconds. Finally, *F(t)* is given by the value of the average load curve. Using these values, the efficiency parameter can be defined.

The gasket efficiency parameter, referred to as $\eta\%$ is defined as a measure that compares the behavior of the tested gasket to that of an ideal gasket. The formula for the parameter is given in Equation 6.

$$\eta\% = \left(1 - \frac{F_{max} * t_d - \int_0^{t_d} F(t)dt}{t_d * (F_{max} - F_s)}\right) * 100\% \quad (6)$$

As mentioned previously, it incorporates measures such as the maximum force achieved, F_{max}, the sealability of the gasket product F_s, the test duration t_d, and the force at any given time during the test F(t). For this parameter to yield a usable result the value of F_{max} must exceed F_s, otherwise the gasket would not seal properly, and the efficiency value obtained from Eq. 6 would be over 100%. This result would obviously be incorrect as this result would mean that the load on the gasket would increase over time, which is impossible under

these conditions. Based on the experimental conditions and Eq. 6, an ideal gasket would form a proper seal and display negligible load decay behavior (i.e., F(t)= F_{max}) regardless of the test duration or the value of F_{max}. An example of ideal gasket behavior is shown in the top right corner of Fig. 10. However, in real gaskets, the gasket experiences load decay behavior as it conforms to the flange faces to increase sealability. This behavior is shown on the top left side of Fig. 10. Finally, if the load history of a clamped gasket is equal to or beneath the sealability for most of the test duration t_d, the efficiency of the gasket will either converge to zero or be negative, meaning that the gasket is unsuitable for use.

For all the tests described in this paper, the efficiency is calculated over the entire duration of the test, including the initial torque and retorque (if applicable). By using the efficiency parameter in conjunction with the ANOVA procedure introduced in Section 2.6, it is possible to evenly compare the performance of several different types of gaskets under various conditions.

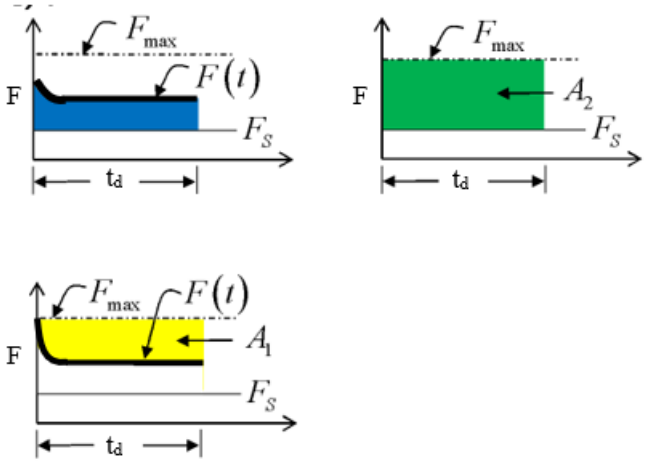

Figure 10: Graphical depiction of the efficiency parameter

2.6 Statistical Methods

In this study, statistical methods are necessary to help collate the data and draw meaningful conclusions from it. Using these methods on the efficiency data discussed earlier, it will be possible to determine to what extent certain factors have an impact on the efficiency of a gasket. Based on a review of some of the prominent literature in this field, there have been few studies that seek to use statistical methods such as these to characterize gasket behavior. Hopefully, the use of these methods will help fully characterize certain aspects of gasket mechanics and allow for the design of better performing gaskets.

The main statistical method used in this study was Analysis of Variance (henceforth referred to as ANOVA). It is a statistical method that analyzes data sets to show how much each factor contributes to the output results [9]. All of the basic formulas for ANOVA are provided in Table 4. A basic outline of the ANOVA procedure is also included.

Here, *SS* stands for the Sum of Squares for a factor or measure, which is a measure of how far each measurement is from the mean. Meanwhile, df represents the degrees of freedom, a measure of the differences in treatments allowed by the test matrix. The Mean of Squares, represented by MS, is the variation between sample means for that particular factor. The indices (*i, j, and k*) represent the number of different treatments for a factor. As for the independent variables in the equations, *n* is the total number of experiments in the study, *m* is the number of replications, and the lowercase factors (*a*, *b* and *c*) represent the number of levels for each factor. Using variables for the *i*th index as an example, X_i is the value of one observation, $\bar{X}_i$ is the mean for that particular treatment, and X is the grand mean for all data points in the experiment. Using these terms, ANOVA's methodology can now be explained.

Table 4: Analysis of Variance equations

	Sum of Squares	*Degrees of Freedom*	*Mean of Squares*
Total	$SS_T = \sum_l \sum_k \sum_j \sum_i \left(x_{ijkl} - \bar{x}\right)^2$	$dof = n - 1$	$MS_T = \frac{SS_T}{df}$
Factor A	$SS_A = mbc \sum_i (\bar{x_i} - \bar{x})^2$	$dof_A = a - 1$	$MS_A = \frac{SS_A}{df_A}$
Factor B	$SS_B = mac \sum_j \left(\bar{x_j} - \bar{x}\right)^2$	$dof_B = b - 1$	$MS_B = \frac{SS_B}{df_B}$
Factor C	$SS_C = mab \sum_k (\bar{x_k} - \bar{x})^2$	$dof_C = c - 1$	$MS_C = \frac{SS_C}{df_C}$
Comb. AB	$SS_{AB} = mc \sum_j \sum_i \left(\bar{x_{ij}} - \bar{x}_i - \bar{x}_j + \bar{x}\right)^2$	$dof_{AB} = (a-1)(b-1)$	$MS_{AB} = \frac{SS_{AB}}{df_{AB}}$
Comb. AC	$SS_{AC} = mb \sum_k \sum_i (\bar{x_{ik}} - \bar{x}_i - \bar{x}_k + \bar{x})^2$	$dof_{AC} = (a-1)(c-1)$	$MS_{AB} = \frac{SS_{AC}}{df_{AC}}$
Comb. BC	$SS_{BC} = ma \sum_k \sum_j \left(\bar{x_{jk}} - \bar{x}_j - \bar{x}_k + \bar{x}\right)^2$	$dof_{BC} = (b-1)(c-1)$	$MS_{BC} = \frac{SS_{BC}}{df_{BC}}$
Comb. ABC	$SS_{ABC} = m \sum_k \sum_j \sum_i \left(\bar{x}_{ijk} - \bar{x}_i - \bar{x}_j - \bar{x}_k + \bar{x}\right)^2$	$dof_{ABC} = (a-1) * (b-1) * (c-1)$	$MS_{ABC} = \frac{SS_{ABC}}{df_{ABC}}$
Within	$SS_W = \sum_l \sum_k \sum_j \sum_i \left(x_{ijkl} - \bar{x}_{ijkl}\right)^2$	$dof_W = n - abc$	$MS_W = \frac{SS_W}{df_W}$

The first step in the ANOVA procedure is to find the degree of freedom for each factor or combination. Next, the sum of squares is calculated for each factor and combination. After that, the Sum of Squares within can be found to calculate the error. Finally, the total Sum of Squares is found. Using the values found in the steps above, the relative importance of any factor or combination of factors can be found by using Eq. 7.

$$\% = \frac{SS}{SS_T} \tag{7}$$

For this paper, ANOVA was used on the efficiency parameter to find the factors that contributed most to the efficiency.

2.7 Knowledge Gaps

Even with all of the information discussed in the previous sections, there were still several areas where additional engineering analysis was needed. Presently, very few studies have been done that compare the behavior of different types of gasket materials under a re-torque. Of the studies that have been done, the majority of them focus on the behavior of the flange as a whole by measuring quantities such as bolt elongation instead of focusing on the response of the gaskets themselves. Additionally, most of the studies that have been performed up until this point have focused on characterizing the behavior of gaskets under ambient conditions. However, this is not entirely realistic as gaskets are often subjected to elevated temperatures and pressures in an industry setting. Also, in terms of finite element modeling, there exists no finite element model that can be both accurately simulate gasket loading and unloading behavior and be used to optimize the design of gaskets for various different applications. Therefore, this thesis will present a framework that attempts to rectify all of these issues.

CHAPTER 3 PRELIMINARY STUDIES

3.1 Experimental Setup

Initial studies have been conducted to address some of the knowledge gaps identified in Chapter 2. To this end, gasket behavior was characterized by using a component scale multi-bolt test platform, which was constructed in accordance with ASTM standards [10]. The platform tested gasket samples with an outer diameter of 8.75” and an inner diameter of 6.62”, leading to a cross sectional area of 25.71 in^2. The assembled test platform is shown in Fig. 11. It consisted of two identical flanges, each containing 6” bores and holes for eight bolts. The bottom flange was supported by a mock pipe that is fixed to an isolation table. Four of the bolts were connected to load cells that collected load data over the duration of the test. Analog signals from each of the load cells were transmitted to a National Instruments data acquisition device via a USB cable. This data could then be read and processed using a custom-built Graphical User Interface (GUI).

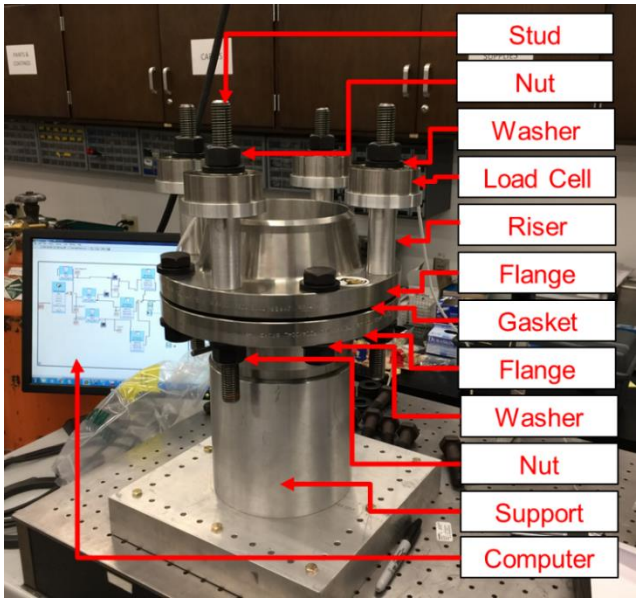

Figure 11: Test Platform for ambient temperature experiments

The test procedure for one of these experiments is as follows. To start the test, a virgin gasket sample was installed between the flange faces. The flange was then reassembled and the bolts were tightened using a digital torque wrench. Using the star pattern, the load was sequentially raised to 33%, 66%, and 99% of the desired value. The bolts were then fully torqued to their final value of 150 ft-lbs. in a counterclockwise pattern. After a dwell period of either 1 hour or 12 hours, a re-torque was applied to each bolt. The test duration lasted from the point when 100% of the desired initial torque was achieved until 12 hours after the final torque. These test durations were chosen based on the results of other studies in the field [11,12,13].

3.2 Outcomes of Ambient Temperature Experiments

The ambient temperature experiments measured the effects of gasket texture, filler material, gasket thickness, and dwell time on overall gasket performance. They provide a baseline of performance that can be used later. The analysis was split into three parts. The first part (Part 1) measured the impacts of filler material, dwell time, and gasket thickness on the performance of flat gaskets. The second part (Part 2) dealt with determining the impact of texture on gasket performance. Part 3 sought to determine whether or not a retorque was actually necessary. The test matrices and outcomes of each analysis are listed below.

Part 1:

As mentioned previously, this phase of experiments measured the impacts of filler material, dwell time, and gasket thickness on the performance of flat gaskets. There are two levels for each factor. The two filler materials are the blue and white materials, the two thicknesses are 1/8” and 1/16”, and the two dwell periods are 1 hour and 12 hours. As the different gaskets were discussed in Section 2.2, no description of these different gasket

materials will be provided here. However, a sketch of both dwell periods is shown in Fig. 12. In an industry setting, bolted joints often undergo a secondary torque which theoretically improves load retention. These two dwell periods will be compared to ascertain what impact the length of the dwell period has on the efficiency of the gasket. If it is fairly minor, the dwell period can be shortened, leading to reduced down times for pipelines.

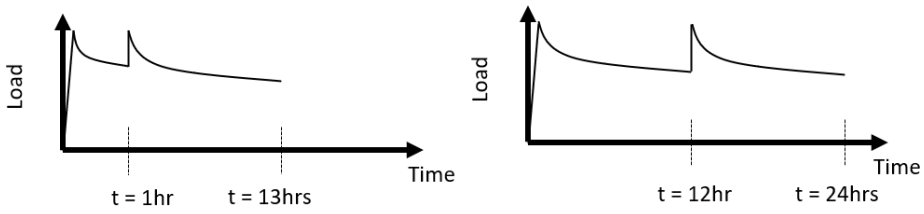

Figure 12: (Left) Sketch of a 1-hour dwell time test; (Right) Sketch of a 12-hour dwell time test

With all of these factors clearly defined, the test matrix for this phase of experiments can now be assembled. The test matrix is shown in Table 5. Three trials of each run listed in the table were conducted, for a total of 24 experiments. Using the data from these experiments, the importance of each of the factors can be determined.

Table 5: Test matrix for Part 1

Run	*Material*	*Dwell Time (hrs.)*	*Thickness (in)*
1	Blue	12	1/8”
2	White	12	1/8”
3	Blue	1	1/8”
4	White	1	1/8”
5	Blue	12	1/16”
6	White	12	1/16”
7	Blue	1	1/16”
8	White	1	1/16”

The efficiency results of these experiments were then collected. A summary of these results is found in Table 6. The efficiency value for each repeat is listed, along with the average efficiency for the overall run. These results could then be fed into the analysis to determine the relative importance of each factor.

Table 6: Part 1 efficiency data

Run	*Trial 1*	*Trial 2*	*Trial 3*	*Average*
1	88	87	83	85.60
2	81.9	82	82.6	84.35
3	81.2	84.4	79.6	79.62
4	84.6	85	86	85.82
5	88.65	87.39	91.1	91.41
6	99.6	98.1	98.1	98.18
7	88.66	91.1	93	92.87
8	98.3	97.6	99.2	98.36

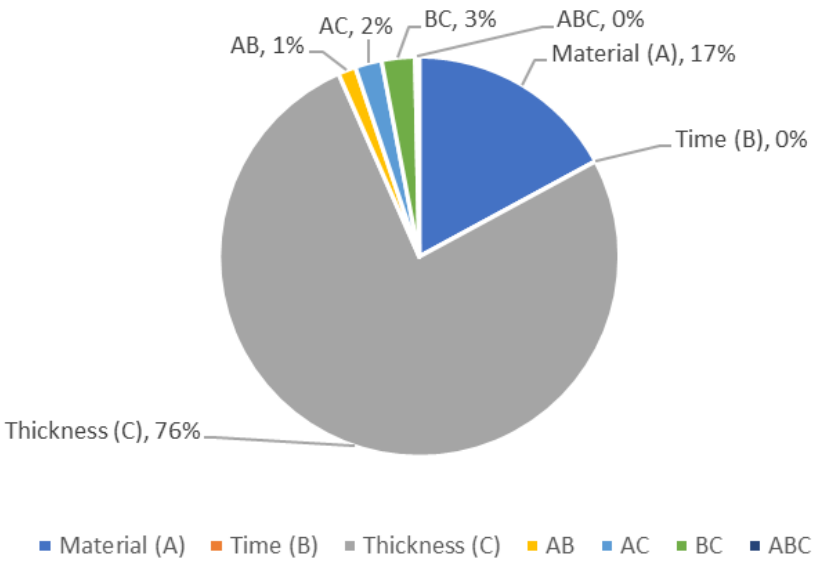

Figure 13: ANOVA results based on efficiency values for Part 1

The relative contributions of each factor on the efficiency were found using ANOVA (described in Section 2.6). The results of this analysis are shown in Fig. 13. The most

influential factor on the overall performance of the gasket was the thickness of the gasket, with a contribution of 76.28%, followed by the filler material at 17.1%, and the dwell time with a contribution of 0.8%. Of the interactions, the most important was the interaction between the thickness and the dwell time, having a contribution of 2.7%, followed by the interaction between thickness and filler material at 2.15%, and the interaction between the material and dwell time at 1.44%. The interaction between all three factors proved to be mostly irrelevant in this case as its contribution towards the efficiency parameter was only 0.33%.

These results align fairly well with current theories and observations about gasket performance. It has long been observed that thinner gaskets have better load retention capabilities than their thicker counterparts and those observations were repeated in this study. Case in point, the thicker gaskets had an average efficiency of 87.6%, whereas the thinner gaskets had an average efficiency of 94.3%; however, one unexpected finding was the relatively low impact of the dwell time on the overall efficiency. Standard retorquing procedures in an industry setting recommend torquing all of the bolts on the flange about twelve hours after the initial torque, but the results of this experiment show that the length of this dwell period between torques is unimportant. This implies that gaskets can achieve close to optimal efficiency with a retorque that is relatively soon after the initial torque, leading to less down time for important plant systems.

Part 2:

Part 2 sought to answer the question of whether or not a textured surface meant that a gasket was better at maintaining a seal over a long period of time. For this series of experiments, the textured 3/32” gasket was used in place of the flat 1/8” gasket. The same

analysis procedure applied earlier in Part 1 is used here. The only difference in this case is that the three variables in question are texture, filler material, and dwell time. The test matrix for this series of experiments is shown in Table 7. As before, three trials of each run listed in the table were conducted, for a total of 24 experiments.

Table 7: Test matrix for part 2

Run	*Material*	*Dwell Time (hrs.)*	*Texture*
1	Blue	12	Flat 1/8”
2	White	12	Flat 1/8”
3	Blue	1	Flat 1/8”
4	White	1	Flat 1/8”
5	Blue	12	Textured 3/32”
6	White	12	Textured 3/32”
7	Blue	1	Textured 3/32”
8	White	1	Textured 3/32”

From these experiments, the efficiency values for each trial were obtained. These results are shown in Table 8. As before, the efficiencies for each repeat are listed alongside the average run efficiency. The efficiency values were then analyzed to determine the contribution of each factor.

Table 8: Part 2 efficiency data

Run	*Trial 1*	*Trial 2*	*Trial 3*	*Average*
1	81.16	91.87	80.33	84.45
2	81.76	86.12	84.21	84.03
3	74.73	73.99	79.51	76.08
4	87	81.4	81.6	83.33
5	98.01	98.05	98.67	98.24
6	99.56	99.64	98.46	99.22
7	97.04	95.84	98.16	97.01
8	96.1	99.05	98.18	97.78

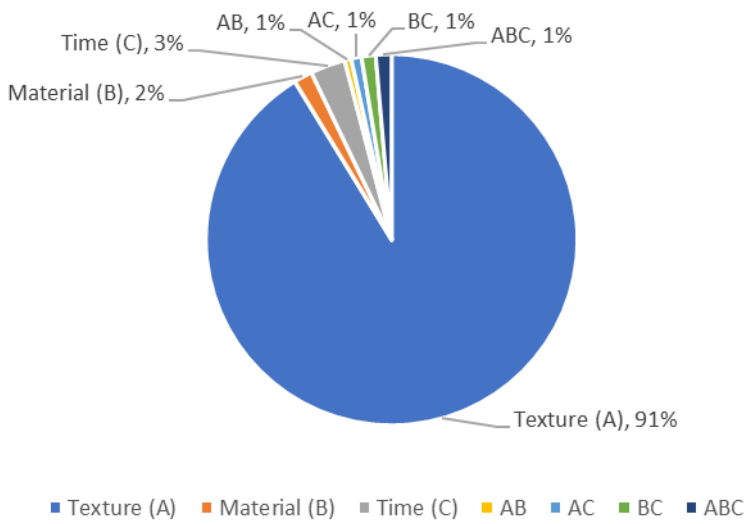

Figure 14: Analysis results for Part 2

As before, ANOVA was applied to determine the relative importance of each factor on the efficiency (η%). The results of this analysis are shown in Fig 14. The most important factor is shown to be the gasket texture, with a relative importance of 91.27%, followed by the dwell time with a contribution of about 3.04%, and finally the filler material at 1.62%. Again, the interactions between factors were relatively meaningless. The most important interaction was the interaction between all three factors with a relative importance of 1.374%, followed by the interaction between filler material and dwell time at 1.227% and the interaction between texture and dwell time with 0.9%

These results are fairly close to what was expected based on current theories about gasket performance. The textured gaskets performed far better than the flat ones, having an average efficiency of 92.6% to the average 87.6% of their flat counterparts. This was at least partially due to the fact that the textured surfaces increased compliance with the flange surface, allowing for a better seal to form. Another explanation could be that the hexagonal cells acted like suction cups, creating a vacuum between the gasket and the flange face,

which helped the flange retain load. This hypothesis would need to tested, most likely using CFD, to confirm whether or not any vacuum-like effect occurs. Also, as in Part 1, across all other conditions, the impact of the dwell time on the overall efficiency remained relatively low. This further supports the idea put forth in Part 1, that gaskets can achieve close to optimal efficiency with a retorque that is relatively soon after the initial torque. If this idea holds true, the installation and maintenance procedures for PTFE gaskets could be shortened significantly, leading to decreased down time.

Part 3:

As the previous two parts of the experiments found that the dwell time between torques was almost irrelevant, Part 3 sought to test whether or not a secondary torque was actually necessary to obtain maximum efficiency. To that end, the factors tested in this part were gasket texture, filler material and application of a re-torque. However, in this phase, the levels for the dwell factor were changed so that the higher level constituted a re-torque after 12 hours, while the lower level lacked any kind of re-torque. A sketch of both of these loading patterns is shown in Fig. 15. This difference will allow the difference in efficiency caused by the presence of a re-torque to be quantified.

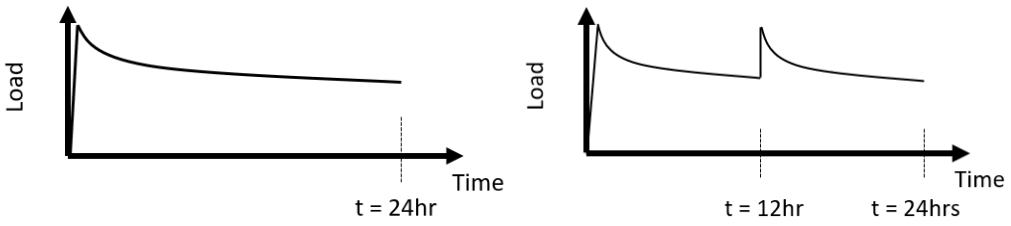

Figure 15: (Left) Sketch of no re-torque load curve, (Right) Sketch of 12-hour dwell load curve

With all of the conditions for this part of the study set, the test matrix for this part can now be assembled. The test matrix for this part of the study is given in Table 9. As before, each run has a total of three repeats, leading to a total of 24 experiments. These experiments will help determine whether the application of a re-torque is necessary for optimal performance.

Table 9: Test matrix for Part 3

Run	*Material*	*Dwell Time (hrs.)*	*Texture*
1	Blue	12	Flat 1/8”
2	White	12	Flat 1/8”
3	Blue	None	Flat 1/8”
4	White	None	Flat 1/8”
5	Blue	12	Textured 3/32”
6	White	12	Textured 3/32”
7	Blue	None	Textured 3/32”
8	White	None	Textured 3/32”

Similar to the previous parts of the study, efficiency values were collected for each repeat. These efficiency values are shown in Table 10. Again, the efficiency values for each test are listed, along with the run averages. These efficiency values were used in the final analysis for the ambient temperature experiments.

Table 10: Part 3 Efficiency data

Run	*Trial 1*	*Trial 2*	*Trial 3*	*Average*
1	93	98	93	94.67
2	94	95	94	94.33
3	93	80	84	85.67
4	93	98	93	94.67
5	98.01	98.05	98.86	98.31
6	99.6	99.6	98.5	99.23
7	89.96	90.33	92.52	90.94
8	95.7	94.46	91.7	93.95

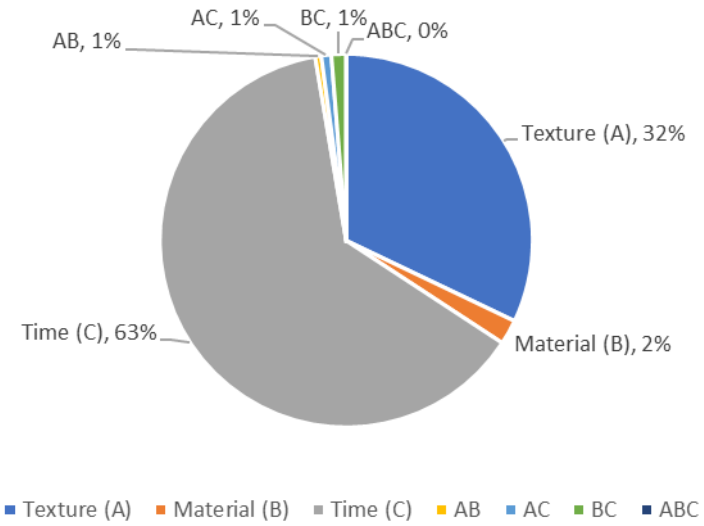

Figure 16: Analysis results for Part 3

ANOVA was again performed on the analysis values to evaluate the importance of each factor. The results of the analysis are shown in Fig. 16. In this part of the study, the presence of a re-torque was proven to be the most important factor, with a contribution of about 63.1% towards the total efficiency. This was followed by the texture of the gasket at 32.1% and the effect of the filler material at 2.14%. The effects of the interactions between factors were again proven to be mostly insignificant, with the most important interaction being that between the filler material and re-torque with a relative importance of 1.3%. This was followed by the interaction between the texture and the re-torque at 0.86% and the interaction between the filler material and the texture at 0.524%.

The presence of a re-torque did increase the efficiency of both types of gaskets by an average of about 7%, suggesting that a retorque is necessary to maximize the efficiency of the gasket seals. However, it is important to note that the effect of the re-torque is not equal over all surfaces but is relatively even across different filler materials. The data gathered in this phase shows that flat gaskets experienced an average efficiency increase of 9% when

given a re-torque after a dwell period, while the textured gaskets only had an average increase of about 6%. Meanwhile, for both filler materials, the average efficiency jumped by about 7%.

While this analysis provides a comprehensive view of how gasket materials respond to a re-torque, the influence of conditions such as the internal temperature and pressure is still not well known. Hence, a new series of experiments was developed and is discussed in Chapter 4.

CHAPTER 4 TEST PLAN

4.1 Motivation

While the previous set of experiments provided valuable insights into gasket mechanics, the testing equipment and procedure did not accurately simulate the conditions that the gaskets would be exposed to in an industry setting. In most industrial applications, gaskets have to endure elevated temperatures and high internal pressures, but these conditions were not present in the previous series of experiments. Hence, several questions such as “How do temperature and pressure interact with filler material to influence performance?” or “How do temperature and pressure interact with texture to influence performance?” were left unanswered. To answer those questions, new testing tools and procedures were developed that could more accurately simulate the conditions that gaskets face in an industry setting. Using the new apparatus, it was possible to characterize gasket mechanics at temperatures up to 500°F and at pressures up to 500 psi. The testing procedure for these experiments is described below in Section 4.2 and the test plans are explained in Section 4.3.

4.2 Experimental Setup

In order to subject gaskets to service like conditions, the test platform shown in Figure 11 was upgraded to be able to handle elevated temperatures and pressures. A 2-kW heating wire and K-type thermocouples were attached to the flange and connected to the data acquisition device in order to be able to increase the temperature of the flange up to a maximum of 500°F. Similarly, pressure sensors and a pump were attached to the flange to increase the internal pressure of the system to a maximum of 500 psi. As before, the load cells collected data at a rate of 1 sample per second, while the pressure sensors and the

thermocouples collected data at a rate of 4 samples per second. The upgraded test platform is shown in Fig. 17.

Figure 17: Upgraded Test Platform

The experimental procedure was similar to the one in the last series of experiments. To start a test, the flange is first disassembled, and the gasket is then placed inside the flange. The flange was then reassembled, and the bolts were then tightened to a final torque of 150 ft-lb (203.4 N-m) using a star pattern.

Once the gasket was fully torqued, the temperature and pressure were set to the desired values for the current test. The pressure was increased to the desired value over the course of about 10 minutes, while the temperature was slowly incremented over the course of

1 hour. The setup then ran independently for the duration of the 20-hour test. After the test is complete, the data was processed to turn the raw signal data into a load relaxation curve.

Unlike in the previous series of experiments however, the effects of the increased pressure and temperature on the load curves needed to be taken into account. For the increased temperature, it was determined that based on the coefficients of thermal expansion of the bolts and the flange pieces, the increase of length for each part should be an order of magnitude smaller than that of the deformation of the gasket (refer to appendix D for full calculations). Therefore, the thermal expansion of the bolts and flange pieces should have little to no effect on the load curve and thus can be ignored. However, the same cannot be said for the effects of internal pressure. Based on the maximum internal pressure applied and the diameter of the flange head, there would be a net decrease in load of up to 600 lbs. per bolt (full calculations shown in appendix D). However, as this offset was constant across all of the different types of gaskets, and due to the fact that the force lost was only 5% of the maximum load at the highest level, it was determined that the impact of this on the experimental results was minimal.

4.3 Test Plan

The testing and analysis for this series of experiments was again split into three phases. The first phase sought to answer the question of what impact the flange temperature and internal pressure had on the efficiency of gaskets made from different materials. Based on the results from Phase 1, the second phase sought to determine the extent to which the flange temperatures affected the efficiencies of flat gaskets with different filler materials and thicknesses. Meanwhile, the third phase was designed to answer the question of how the overall style of a gasket, the flange temperature, and the filler material influenced gasket

efficiency. A mixed level ANOVA design was used in all three phases to answer these questions.

Phase 1:

As mentioned previously, Phase 1 asked what impact the flange temperature and internal pressure had on the efficiency of gaskets made from different materials. To this end, the test matrix shown in Table 11 was constructed. The three variables tested in this phase were the filler material, flange temperature, and the internal pressure of the flange. All of the gaskets used in this phase were textured and had a thickness of 3/32". There were two filler materials (tan and blue), three different temperatures (100°F,300°F, and 500°F), and three different internal pressures (100 psi, 300 psi, and 500 psi) tested in this phase. The results from these experiments are shown in section 5.1.

Table 11: Test Matrix for Phase 1

Run	*Material (A)*	*Temperature (°F) (B)*	*Pressure (psi) (C)*
1	Tan	100	100
2	Tan	100	300
3	Tan	100	500
4	Tan	300	100
5	Tan	300	300
6	Tan	300	500
7	Tan	500	100
8	Tan	500	300
9	Tan	500	500
10	Blue	100	100
11	Blue	100	300
12	Blue	100	500
13	Blue	300	100
14	Blue	300	300
15	Blue	300	500
16	Blue	500	100
17	Blue	500	300
18	Blue	500	500

Phase 2:

The test matrix for Phase 2 was constructed based on the results of the Phase 1 experiments. It was discovered that the internal pressure of a flange had next to no impact on gasket efficiency, so that variable was removed from all subsequent analyses. However, the impact of the temperature was shown to be enormous, so the second phase sought to determine the extent to which the flange temperatures affected the efficiencies of flat gaskets with different filler materials and thicknesses. The test matrix for these experiments is shown in Table 12. This time, all three filler materials were tested (blue, tan, and white) along with both varieties of flat gasket (Flat 1/8" and Flat 1/16") at various different temperatures (100°F,300°F, and 500°F). The results of these experiments are discussed in Section 5.1.

Table 12: Phase 2 Test Matrix

Run	*Material (A)*	*Thickness (in) (B)*	*Temperature (°F) (C)*
1	Blue	Flat 1/8"	100
2	Blue	Flat 1/8"	300
3	Blue	Flat 1/8"	500
4	Blue	Flat 1/16"	100
5	Blue	Flat 1/16"	300
6	Blue	Flat 1/16"	500
7	Tan	Flat 1/8"	100
8	Tan	Flat 1/8"	300
9	Tan	Flat 1/8"	500
10	Tan	Flat 1/16"	100
11	Tan	Flat 1/16"	300
12	Tan	Flat 1/16"	500
13	White	Flat 1/8"	100
14	White	Flat 1/8"	300
15	White	Flat 1/8"	500
16	White	Flat 1/16"	100
17	White	Flat 1/16"	300
18	White	Flat 1/16"	500

Phase 3:

In Phase 3, some of the data from Phase 2 was analyzed alongside new data to create an overall picture of the factors that influence gasket efficiency. The three factors studied in this study were the overall style of a gasket (the combination of thickness and texture), the filler material, and the temperature. The test matrix is given in Table 13. There were three different styles (Textured 3/32", Flat 1/8" and Flat 1/16"), two different filler materials (white and blue), and three different temperatures (100°F,300°F, and 500°F). These results are also shown in Section 5.1.

Table 13: Test Matrix for Phase 3

Run	*Style (A)*	*Material (B)*	*Temperature (°F) (C)*
1	Textured 3/32"	Blue	100
2	Textured 3/32"	Blue	300
3	Textured 3/32"	Blue	500
4	Textured 3/32"	White	100
5	Textured 3/32"	White	300
6	Textured 3/32"	White	500
7	Flat 1/8"	Blue	100
8	Flat 1/8"	Blue	300
9	Flat 1/8"	Blue	500
10	Flat 1/8"	White	100
11	Flat 1/8"	White	300
12	Flat 1/8"	White	500
13	Flat 1/16"	Blue	100
14	Flat 1/16"	Blue	300
15	Flat 1/16"	Blue	500
16	Flat 1/16"	White	100
17	Flat 1/16"	White	300
18	Flat 1/16"	White	500

CHAPTER 5 EXPERIMENTAL RESULTS

5.1 Effect of Temperature

As mentioned in the introduction to this thesis, Chapter 5 will attempt to describe the effect of various factors, such as the temperature, pressure, and the interaction between those two factors on quantities relevant to understanding gasket performance such as the load loss and the force history. The effects of factors such as style, thickness and filler material will not be discussed here as their impact has already been discussed in earlier studies [14-18]. This section deals with the effects of temperature on the specified quantities.

Temperature had a pronounced effect on the force history of a gasket. An example of this can be seen in the load curves displayed in Fig. 18. The chart on the left shows the load decay history for a textured blue gasket being tested at 100°F and 500 psi, while the right graph displays the force history for a textured blue gasket at 300°F and 500 psi.

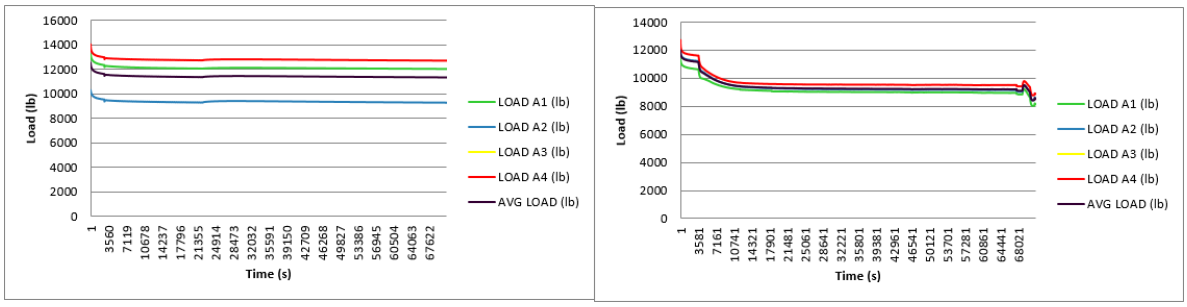

Figure 18: (left) load curve for a textured blue gasket tested at 100°F and 500 psi, (right) load curve for a textured blue gasket at 300°F and 500 psi

The most noticeable difference between the two charts is the precipitous drop in load observed in the gasket tested at 300°F. This drop occurred during the period of temperature increase and was even more pronounced at higher temperatures. As this pattern of load loss

during the temperature increase was prevalent throughout this series of experiments, albeit to varying degrees, it is possible to conclude that an increase in flange temperature while the gasket is in operation leads to a corresponding decline in the load. There are many reasons that this could be the case, but plausible explanations are conjectured in Chapter 6.

The pattern of load loss only became more pronounced as the temperature increased. A graph of the load loss at different temperatures for the textured blue gaskets is shown in Fig. 19. This graph helps clarify the relationship between temperature and load loss for gaskets tested at 100 psi. The regression equation shows on the chart shows the relationship between the temperature and the load lost. This equation has the form

$$F_L = m\left(\frac{T}{T_0} + C\right) \tag{8}$$

Here m is the slope of the line in lbs., T the flange temperature in °F, T_0 is the melting temperature of PTFE in °F, and C is a unitless constant.

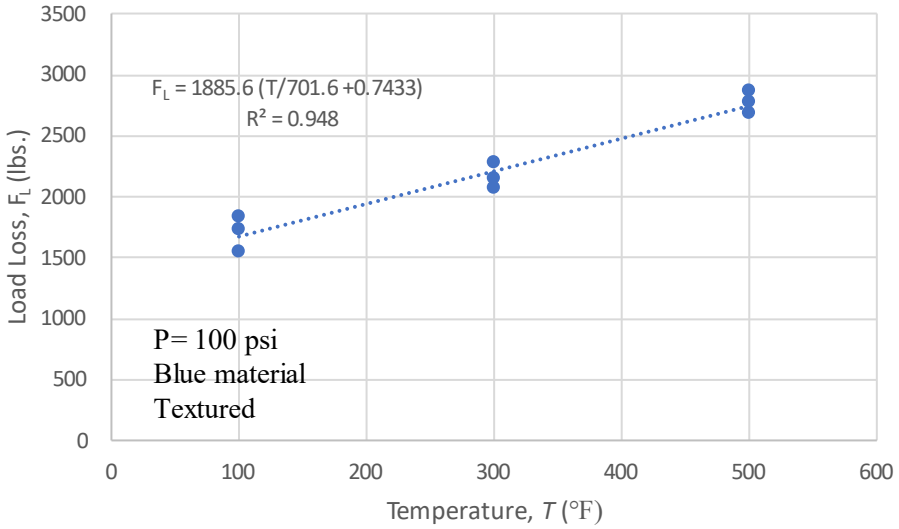

Figure 19: Load Loss at different temperatures for 100 psi tests

Based on this graph, it is clear that the amount of load loss increases linearly with the flange temperature. The load loss appears to be the same as room temperature for the tests performed at 100°F (based on the shape of the load curve) but climbs by about 600-800 lbs. for each 200°F increase. Similar patterns also hold for the other types of gaskets, albeit to varying degrees. For example, the flat 1/8" gaskets tested in Phases 2 and 3 experience slightly more load loss with each temperature increase, with an average of 900 lbs. between each temperature level. Meanwhile, the thinner 1/16" gaskets experienced slightly less load loss, with the load decreasing about 600 lbs. per temperature increment. Some load curves and load loss charts for these other types of gaskets are shown in the appendix.

5.2 Effect of Pressure

As bolted connections are often pressurized, it is important to understand what effects the internal pressure has on the performance of a gasket. The impact of the internal pressure on the force history of a gasket was relatively straightforward. The internal pressure of the flange served as more of an offset parameter for the force histories, rather than causing any dramatic changes in the load like the temperature. This can be seen in the graphs in Fig. 20. Figure 20 (left) shows a graph of the load decay curve of a textured gasket tested at 100°F and 100 psi, while on the right is a load curve for a gasket tested at 100°F and 300 psi.

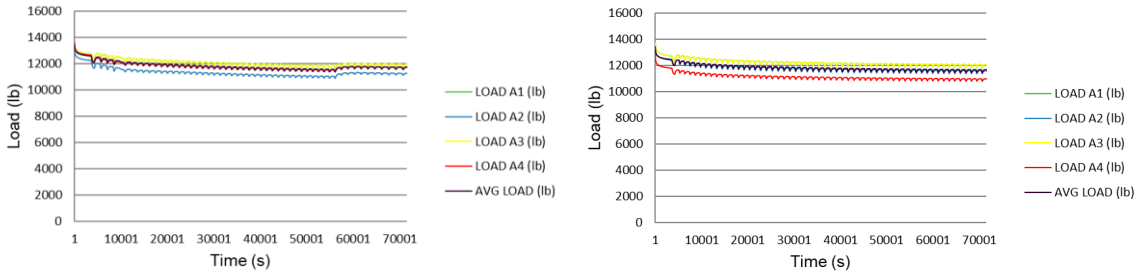

Figure 20: (left) load curve of a textured gasket tested at 100°F and 100 psi, (right) load curve for a gasket tested at 100°F and 300 psi

These graphs show that the average load curve for experiments done at a higher pressure are offset somewhat, being 100-200 lbs. lower than the load curves for the tests done at a lower internal pressure. Based on this, it is hypothesized that the pressure does not really have a significant impact on the shape of the load curve as the margin of difference is negligible in comparison to the loads applied that it may as well be negligible.

The internal pressure also had some impact on the load loss experienced by a gasket. A graph of the load loss measured at each pressure interval is shown in Fig. 21. This graph displays a regression analysis of how pressure affects the load loss across all three pressure levels for a blue textured gasket tested at 100°F. The regression equation shows on the chart shows the relationship between the internal pressure and the load lost. This equation has the form

$$F_L = m\left(\frac{P}{P_0} + C\right) \tag{9}$$

Here m is the slope of the line in lbs., P is the internal pressure in psi, P_0 is an extremely large internal pressure (psi), and C is a unitless constant.

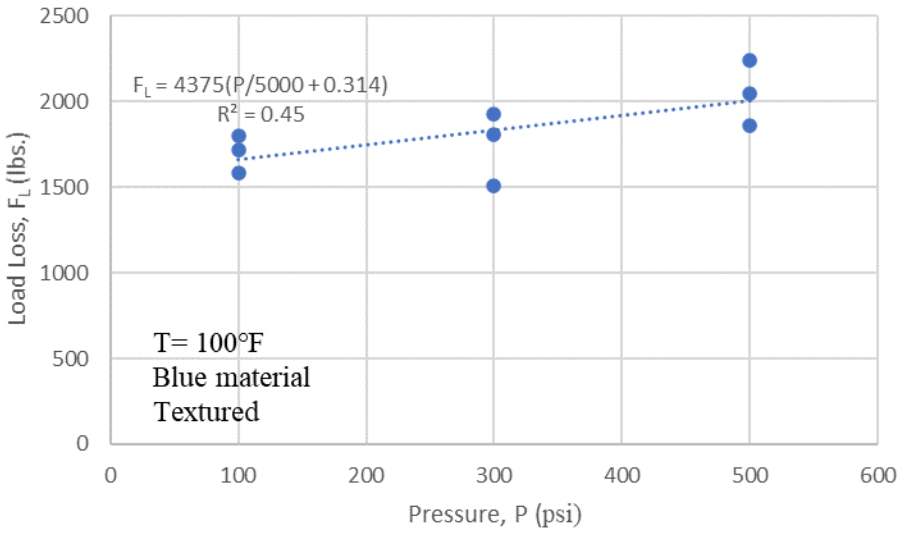

Figure 21: Load loss regression for a blue textured gasket tested at 100°F

The regression analysis shows that there is a gradual increase in load lost as the internal pressure increases. As shown in Figure 21, for each jump in pressure, load loss increases by about 120 lbs. This pattern also repeats with the tan gaskets tested in Phase 1, albeit with a slightly larger margin as the tan gaskets appear to suffer from load loss increases of 200-300 lbs. for each pressure increment. This suggests that for every 200-psi increase, there is a corresponding increase in the hydrostatic end force exerted on the bolts. It also suggests that the impact of pressure on the overall performance of a gasket is far smaller than that of temperature, as the increases in temperature caused the load lost to increase by around 800 lbs. while the increases in pressure caused the load to decrease by only an additional 150-200 lbs.

5.3 Interaction between Temperature and Pressure

As the interplay between pressure and temperature consists of the superposition of the influences of both of these factors on the load curves, any discussion of how this interplay

would affect the shape of the load curve is somewhat nebulous. There is no clear trend in the shape of the load curves that can be used to determine what attributes are caused by the interplay between the two factors. However, an examination of the load loss may yield some valuable information.

The results of the experiments suggest that there was some interaction between temperature and pressure. Figure 22 displays the load loss for various pressures at 300°F. By comparing the results in this graph to those in Fig. 21, it is possible to determine the effect of the temperature-pressure interplay on the load loss.

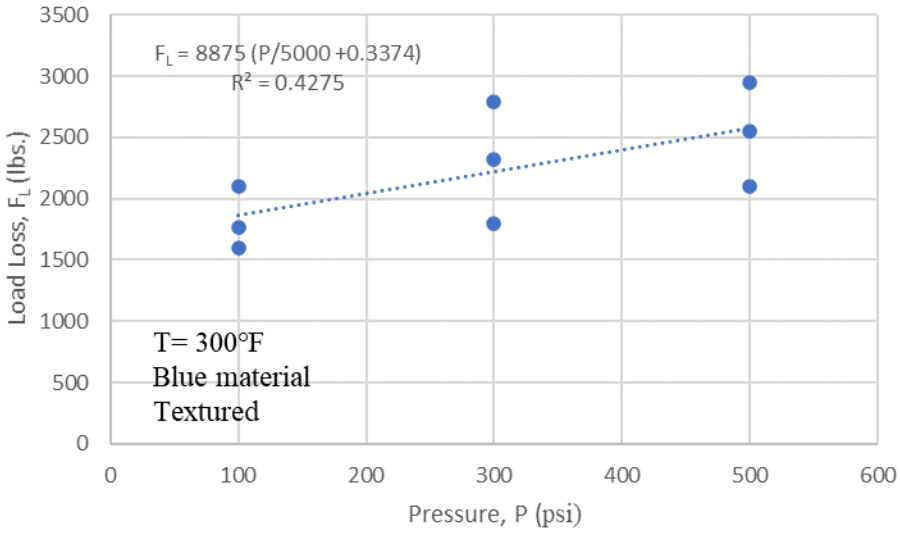

Figure 22: Load loss for a textured blue gasket at various pressures tested at 300°F

In this figure, the slope of the graph is about 8875. That means that for every 200-psi increase, the load loss increases by about 250 lbs. It also appears that the variance in the load loss is greater at 300°F as compared to the 100°F trials, hence the relatively low R^2. Additionally, when compared to the slope of the line in Figure 21, it is evident that the slope for the experiments performed at 300°F is somewhat steeper than the one at 100°F. This

makes it clear that the increase in temperature increases the effect of the pressure variation. A full breakdown between the effect of temperature and pressure on load loss can be seen in Fig. 23. This surface plot shows the spectrum of load loss for each level of temperature and pressure that was tested in this series of experiments. These results are for the blue textured gaskets.

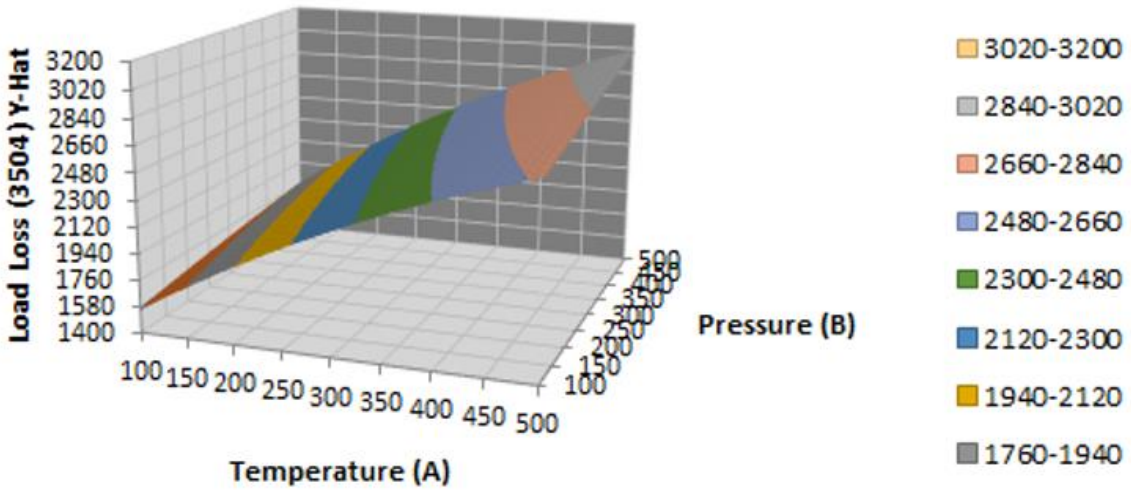

Figure 23: Load loss surface plot for a textured blue gasket

This surface plot shows that, as expected, the highest load loss occurred at 500°F and 500 psi. Furthermore, it shows that the influence of pressure (shown by the slope of the surface along the pressure axis) increases as the temperature increases, confirming the idea that there is some kind of interplay between the two factors that leads to greater load loss. This is likely because the change in the mechanical properties of the gasket exacerbates the effects of the hydrostatic end force on the bolts. However, it should be noted that the load losses portrayed in the graphs in this section are minimal when compared to the load applied. With a maximum load of approximately 96000 lbs. distributed across 8 bolts, load loss on

the scale seen in Figs. 19, 21, and 22 which hovers around 2000-3000 lbs., still implies that the gaskets are fairly efficient and capable of producing a proper seal.

In order to truly determine the impact of these factors on the overall performance of a gasket, a robust statistical analysis of the results is required; therefore, the results of these experiments are analyzed using Analysis of Variance (ANOVA) in Chapter 6.

CHAPTER 6 STATISTICAL ANALYSIS

With all the data having been collected, the same analysis procedure applied in Section 3.2 was used on the current set of data. The analyses for all three phases of the current experiment are provided. As mentioned in Chapter 4, Phase 1 asked what impact the flange temperature and internal pressure had on the efficiency of gaskets made from different materials, while Phase 2 sought to determine the extent to which the flange temperatures affected the different types of flat gaskets. Phase 3 analyzed data from Phase 2 alongside new data to create an overall picture of the factors that influence gasket efficiency.

6.1 Phase 1

The test matrix from Chapter 4 has been copied as Table 14. This table contains the conditions for each run. There were three repeats for each run, resulting in 54 total experiments.

Table 14: Phase 1 Test Matrix

Run	*Material (A)*	*Temperature (°F)* (B)	*Pressure (psi) (C)*
1	Tan	100	100
2	Tan	100	300
3	Tan	100	500
4	Tan	300	100
5	Tan	300	300
6	Tan	300	500
7	Tan	500	100
8	Tan	500	300
9	Tan	500	500
10	Blue	100	100
11	Blue	100	300
12	Blue	100	500
13	Blue	300	100
14	Blue	300	300
15	Blue	300	500
16	Blue	500	100
17	Blue	500	300
18	Blue	500	500

By processing the data from these experiments, the efficiency values could be derived from the experimental data. The efficiency values for each experiment are given in Table 15. These efficiency values, aside from being used in the ANOVA analysis, can provide some insight into the influence of certain factors. For one, the trends in this data align well with some of the trends discussed in Chapter 5. As a general rule, the gaskets become less efficient as the flange temperature increases, which mirrors the pattern of load loss discussed previously. For example, the blue gaskets experience an average drop in efficiency of about 5-6% per 200°F increment, which fits with the load loss pattern seen in Section 5.1. Furthermore, the internal pressure of the flange has a minimal impact on the efficiency values as the efficiencies only decrease by 1-2% for each increase in pressure.

Table 15: Phase 1 Efficiency Data

Run	*Trial 1 (η%)*	*Trial 2 (η%)*	*Trial 3 (η%)*	*Average*
1	92.2	94.1	90.2	92.2
2	91.0	89.9	87.4	89.4
3	94.6	88.1	87.2	89.9
4	70.0	81.5	86.0	79.2
5	83.6	91.8	80.0	85.1
6	92.3	80.3	80.3	84.3
7	78.4	76.4	69.2	74.6
8	75.3	72.4	78.6	75.4
9	75.1	73.2	70.5	72.9
10	91.8	96.6	97.5	95.3
11	85.1	87.6	85.0	85.9
12	84.3	85.3	85.1	84.9
13	89.0	82.0	81.0	84.0
14	80.0	79.0	82.0	80.3
15	88.6	80.7	77.3	82.2
16	93.6	76.2	77.1	82.3
17	72.4	73.1	71.6	72.3
18	71.6	69.2	70.4	70.4

By using the data from Table 15, the ANOVA analysis on the efficiency can now be performed. The results of the ANOVA analysis are shown in Table 16. The results of this analysis can be used to find the relative importance of each factor.

Table 16: Phase 1 ANOVA analysis

Source	*Sum of Squares, SS (%)*	*Degrees of Freedom, df*	*Mean of Squares, MS (%)*	*F-Ratio*	*P*
Material (A)	49.81	1	49.81	3.14	0.09
Temperature (B)	2248.49	2	1124.24	71.03	0.00
Pressure (C)	7.1459	2	3.57	0.226	0.80
AB	1.93	2	0.97	0.06	0.94
AC	26.27	2	13.14	0.83	0.44
BC	125.39	4	31.35	1.98	0.12
ABC	12.18	4	3.04	0.19	0.94
Error	569.79	36	15.82		
Total	3041.01	53			

As mentioned in Chapter 2, dividing the Sum of Squares (SS) value for a factor by the total Sum of Squares can be used to determine the relative importance of each factor. A graphical representation of that information is shown in Fig. 24. Based on the results in Table 16 and the representation in Figure 24, it is clear that the flange temperature was by far the most important factor in determining the overall efficiency of a gasket, with an overall contribution of 91%. Naturally, this means that the impacts of the other factors were fairly limited with the next most important factor, the filler material, having a contribution of about 2% and the internal pressure with a contribution of about 0.3%. The combinations of factors had relatively less impact, with the combination between material and temperature accounting for 0.08% while the combination of material and pressure accounted for 1%. The combination between internal temperature and pressure had a surprisingly large contribution at 5.07%, and the combination of all three factors fell just under 0.5%.

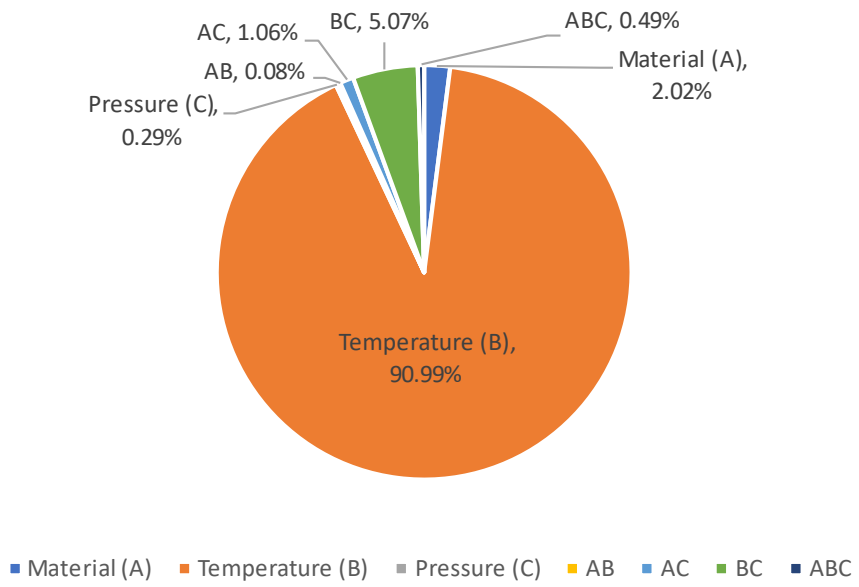

Figure 24: Phase 1 ANOVA contributions

These results correlate quite well with the trends seen in Chapter 5, as the gaskets tested experienced the greatest load loss at higher temperatures. Meanwhile, the pressure served mainly as a slight offset, with the load only dropping about 50 lbs. per 200 psi increase. Finally, the different filler materials did have a slight impact on the load, with the blue gaskets generally experiencing slightly less load loss than their white or tan counterparts at elevated temperatures.

6.2 Phase 2

As before, for the sake of readability, the test matrix for this phase is presented in Table 17. Here, the factors tested are the filler material, gasket thickness, and the flange temperature. As in the previous phase, there were three trials performed for each run, resulting in a total of 54 experiments.

Table 17: Phase 2 Test matrix

Run	*Material (A)*	*Thickness (in) (B)*	*Temperature (°F) (C)*
1	Blue	Flat 1/8”	100
2	Blue	Flat 1/8”	300
3	Blue	Flat 1/8”	500
4	Blue	Flat 1/16”	100
5	Blue	Flat 1/16”	300
6	Blue	Flat 1/16”	500
7	Tan	Flat 1/8”	100
8	Tan	Flat 1/8”	300
9	Tan	Flat 1/8”	500
10	Tan	Flat 1/16”	100
11	Tan	Flat 1/16”	300
12	Tan	Flat 1/16”	500
13	White	Flat 1/8”	100
14	White	Flat 1/8”	300
15	White	Flat 1/8”	500
16	White	Flat 1/16”	100
17	White	Flat 1/16”	300
18	White	Flat 1/16”	500

The data from these experiments can again be processed to yield the efficiency values for each test. These values are shown in Table 18 As before, the gaskets seem to become less efficient as the flange temperature increases. Here, the blue gaskets experience an average drop in efficiency of about 4-7% per 200°F increment, which again fits with the load loss pattern seen in Section 5.1. However, it should be noted that there was a difference in performance between the two different thicknesses. Generally, the thinner 1/16” gaskets experienced lower drops in efficiency with increases in temperature. This also fits with the information gleaned from analyzing the force histories as the load curves for the 1/16” gaskets are generally flatter than their thicker counterparts, so even with the loss in load, they would be less affected by the temperature increase.

Table 18: Phase 2 Efficiency data

Run	*Trial 1 (η)*	*Trial 2 (η)*	*Trial 3 (η)*	*Average*
1	0.970	0.870	0.920	0.920
2	0.860	0.850	0.900	0.870
3	0.800	0.760	0.770	0.777
4	0.910	0.990	0.930	0.943
5	0.870	0.890	0.870	0.877
6	0.760	0.820	0.800	0.793
7	0.750	0.860	0.810	0.807
8	0.800	0.780	0.780	0.787
9	0.760	0.790	0.720	0.757
10	0.960	0.990	0.920	0.957
11	0.880	0.820	0.840	0.847
12	0.810	0.740	0.770	0.773
13	0.850	0.920	0.820	0.863
14	0.800	0.870	0.780	0.817
15	0.760	0.850	0.810	0.807
16	0.920	0.950	0.900	0.923
17	0.880	0.860	0.880	0.873
18	0.800	0.780	0.840	0.807

Table 19:Phase 2 ANOVA analysis

Source	*Sum of Squares, SS*	*Degrees of Freedom, df*	*Mean of Squares, MS*	*F-Ratio*	*P*
Material (A)	0.0165	2	0.0082	6.501	0.004
Thickness (B)	0.0254	1	0.0254	19.984	0.000
Temperature (C)	0.1225	2	0.0613	48.291	0.000
AB	0.0082	2	0.0041	3.245	0.051
AC	0.0066	4	0.0016	1.293	0.291
BC	0.0100	2	0.0050	3.955	0.028
ABC	0.0075	4	0.0019	1.472	0.231
Error	0.0460	36	0.0010		
Total	0.2420	53			

Similar to the last phase of experiments, the values from Table 18 were used in ANOVA to produce the results shown in Table 19. By using the Sum of Squares values in Table 19, it is possible to conclude that the flange temperature was again the most important factor, with a

contribution of about 50.56% towards the efficiency values. By comparison, the impacts of the other factors were fairly minor. The second most important factor proved to be the gasket thickness with a relative importance of 29.3%, followed by the filler material with a contribution of about 6.81%. The combinations in particular had fairly negligible impacts, with the material and temperature combination accounting for 2.71%, the combination between material and thickness for 3.4%, the combination between internal temperature and thickness for 4.14%, and the three-factor combination for just over 3%. A graphical representation of this analysis is shown in Fig. 25.

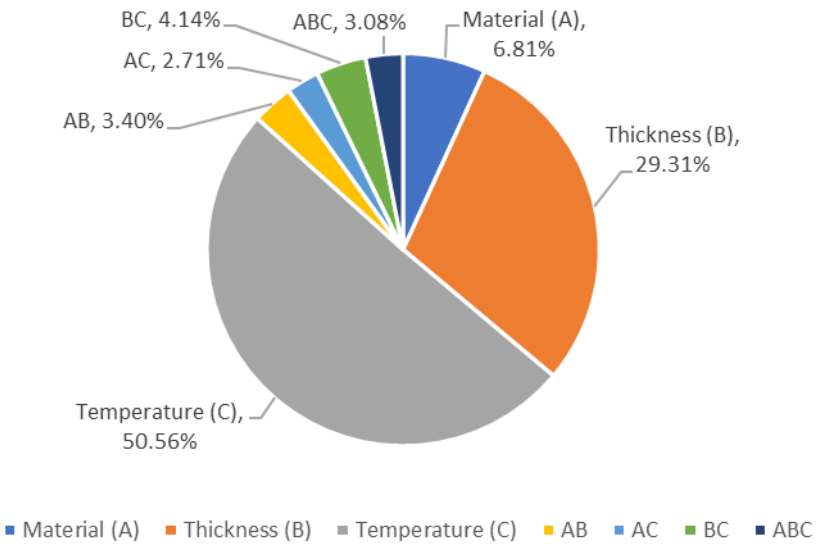

Figure 25: Phase 2 ANOVA contributions

These results support the findings in Phase 1 and correlate well with the trends seen in Chapter 5. As mentioned in the Phase 1 analysis, the gaskets experienced significant load loss at higher temperatures, which caused temperature to be the crucial factor in determining the overall efficiency. However, this time there was another factor that proved to be somewhat significant as well. The load curves for the thinner gaskets were flatter than those of their thicker counterparts, meaning that the gaskets were able to retain more of the load

applied to them over the test duration. This means that the thinner gaskets had far higher efficiency values than the thick ones, which explains the high relative importance of the thickness factor. Finally, the material variable followed the same trend as in Phase 1, with the blue material tolerating higher temperatures slightly better than the white or tan ones. This slight difference explains why the filler material held such a minor share of the contributions for efficiency.

6.3 Phase 3

The same format used for the Phase 1 and Phase 2 discussions is used here. For the sake of readability, the test matrix has been copied here as Table 20. As before, there were three repeats performed for each run, for a total of 54 experiments. This test plan will help clarify how all of the factors influence gasket efficiency.

Table 20: Phase 3 Test matrix

Run	*Style (A)*	*Material (B)*	*Temperature (°F) (C)*
1	Textured 3/32”	Blue	100
2	Textured 3/32”	Blue	300
3	Textured 3/32”	Blue	500
4	Textured 3/32”	White	100
5	Textured 3/32”	White	300
6	Textured 3/32”	White	500
7	Flat 1/8”	Blue	100
8	Flat 1/8”	Blue	300
9	Flat 1/8”	Blue	500
10	Flat 1/8”	White	100
11	Flat 1/8”	White	300
12	Flat 1/8”	White	500
13	Flat 1/16”	Blue	100
14	Flat 1/16”	Blue	300
15	Flat 1/16”	Blue	500
16	Flat 1/16”	White	100
17	Flat 1/16”	White	300
18	Flat 1/16”	White	500

Using the force histories from these experiments, the efficiency value for each run can be calculated. These efficiency values are tabulated in Table 21. The trends in this set of data essentially mirror those found in Phases 1 and 2. Increases in flange temperature again brought about the greatest decreases in gasket efficiency, while different types of gaskets exhibited different load decay patterns, leading to differing efficiency values. On average, the thick flat gaskets were the least efficient overall, while the thinner flat gaskets were often the most efficient. The textured gaskets served as a midpoint between the two.

Table 21: Phase 3 Efficiency data

Run	*Trial 1 (η)*	*Trial 2 (η)*	*Trial 3 (η)*	*Average*
1	0.950	0.880	0.870	0.900
2	0.920	0.800	0.800	0.840
3	0.750	0.730	0.700	0.727
4	0.843	0.850	0.850	0.848
5	0.890	0.810	0.770	0.823
6	0.716	0.692	0.700	0.703
7	0.970	0.870	0.920	0.920
8	0.860	0.850	0.900	0.870
9	0.800	0.760	0.770	0.777
10	0.850	0.920	0.820	0.863
11	0.800	0.870	0.780	0.817
12	0.760	0.850	0.810	0.807
13	0.910	0.990	0.930	0.943
14	0.870	0.890	0.870	0.877
15	0.760	0.820	0.800	0.793
16	0.920	0.950	0.900	0.923
17	0.880	0.860	0.880	0.873
18	0.800	0.780	0.840	0.807

The values in Table 21 were used in the final ANOVA analysis for this thesis, the results of which are shown in Table 22. The results of this analysis can be used to find the relative importance of each factor.

Table 22: Phase 3 ANOVA analysis

Source	*Sum of Squares, SS (%)*	*Degrees of Freedom, df*	*Mean of Squares, MS (%)*	*F-Ratio*	*P*
Style (A)	0.0356	2	0.017	12.203	0.000
Material (B)	0.0056	1	0.005	3.825	0.058
Temperature (C)	0.1571	2	0.078	53.815	0.000
AB	0.0020	2	0.001	0.683	0.512
AC	0.0082	4	0.002	1.400	0.254
BC	0.0056	2	0.003	1.924	0.161
ABC	0.0035	4	0.001	0.602	0.663
Error	0.053	36	0.001		
Total	0.270	53			

Using the same sum of squares analysis on the values in Table 22 essentially confirms the findings of Phase 1. This is shown in Fig. 26. The temperature of the flange was again the critical factor in determining gasket efficiency, with a contribution of about 58%. However, as was the case in Phase 2 there was another factor that was fairly important in determining the overall efficiency. This factor, the gasket style, had a contribution of about 32.6%. The material contribution was again somewhat minor, accounting for about 2% of the total results. The interactions between factors were again almost negligible with the largest one, the interaction between style and temperature contributing 3.03%, followed by the interaction between material and temperature with 2.08%, and the three-factor interaction at 1.3%. The least important interaction was between style and material with a contribution of about 0.74%

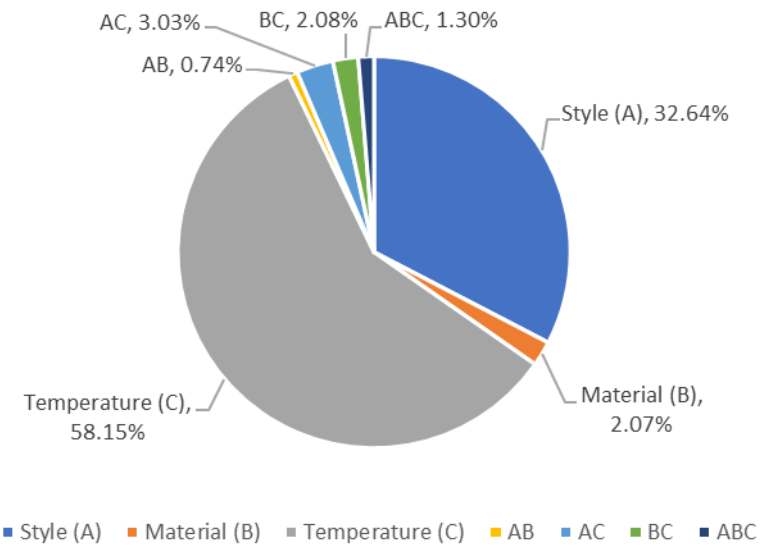

Figure 26: Phase 3 ANOVA Contributions

Again, as in the previous Phases, the temperature was the most important factor, which aligns with the findings from Chapter 5. The high load loss caused by the temperature increase led to the flange temperature being the most important factor contributing to the efficiency. Also, similar to the results of Phase 2, a secondary factor proved to be quite important as the varied conformability and sealability values of the different styles of gasket heavily impacted the shape of the load curve, leading to various differences in efficiency. As a general rule, the thinnest gasket outperformed the other two styles, with the textured gasket being something of a midpoint between the 1/16” gasket and the 1/8” gasket.

Discussion:

There seem to be a few noticeable trends that are seen throughout all 3 phases of testing. The first is that the most important factor in every situation is the temperature of the flange. Every increase in temperature across all three phases caused the average efficiency to drop by 5-6%. This correlates with what was noted in Chapter 5, that the gaskets experience

severe load loss as the temperature increases. An explanation for this behavior could be that the increase in temperature causes the material stiffness to decrease, thereby resulting in load loss. According to the current understanding of polymers, a decrease in stiffness for these materials is generally due to the polymer fibers crosslinking [19]. This crosslinking can sometimes be caused by an increase in temperature, with the point at which PTFE fibers start to crosslink being 285°F [20]. Therefore, it is not unreasonable to consider that the increases in temperature during the test cause the polymer fibers in the PTFE gasket to crosslink, thereby reducing material stiffness. It is most likely this decrease in stiffness that results in the high load loss and drops in efficiency at higher temperatures. In order to confirm this, further research needs to be done by using scanning electron microscopy (SEM) in conjunction with normal material stiffness testing to determine the extent to which PTFE experiences crosslinking at higher temperatures and how much this impacts material stiffness.

Another major trend among all 3 phases is that the style of the gasket was often the second most important factor. This also correlates well with the results presented in Chapter 5. The different gasket geometries often produced different types of load curves, with the thinner gaskets generally producing flatter load curves than their thicker counterparts. Additionally, the textured 3/32” and flat 1/16” gaskets showed much better load retention overall than their thicker counterpart. This, in turn, led to higher efficiency values, which is why ANOVA flagged it as an influential factor.

The analysis presented in this chapter aligns very well with the data presented in Chapter 5. There was an exceptionally strong negative correlation between the load loss experienced by a gasket and its efficiency. Increases in temperature correlated with increases

in load lost, which led to lower efficiency values. Also, different types of gaskets experienced different amounts of load loss during the experiments, which was mirrored by the differing efficiency values in this analysis. For example, flat 1/8” gaskets experienced the greatest load loss leading to the lowest efficiency values, whereas the textured and thinner gaskets experienced far lower load loss, leading to higher efficiency values. However, it still remains to be seen what impact these factors will have on quantities like leak rate or blow out resilience. It is entirely possible that a higher flange temperature could increase leak resistance while an increase in internal pressure could lower it. It is also possible that a combination of higher temperatures and pressures could make blow out failures more common. More experiments will need to be done to determine if this is the case.

It is possible to use the information gained in this series of experiments to design better gaskets. However, in order to do this efficiently, a robust material model will be needed. The development of such a model is discussed in Chapter 7.

CHAPTER 7 NUMERICAL MODELING

7.1 Elastic Modeling

The numerical simulation efforts presented in this thesis seek to put forward a method that can both simulate gasket loading and relaxation behavior, as well as be used for design optimization efforts in the future. The first phase of these numerical simulations consisted of a series of elastic simulations that could help determine the stress state inside a gasket. These simulations would help validate the accuracy of the simulation software and provide a base for the viscoelastic simulations. The elastic simulations were split up into two parts. One part simulated a hypothetical flange that had no friction between the plates and the gasket, while the other simulated a more realistic flange where the faces of the gasket were bonded to the interior plate surfaces. Both cases used the same model shown in Fig. 27. Here, the model consists of three parts, two circular plates and a gasket. A cross sectional view of the model in the YZ plane is shown.

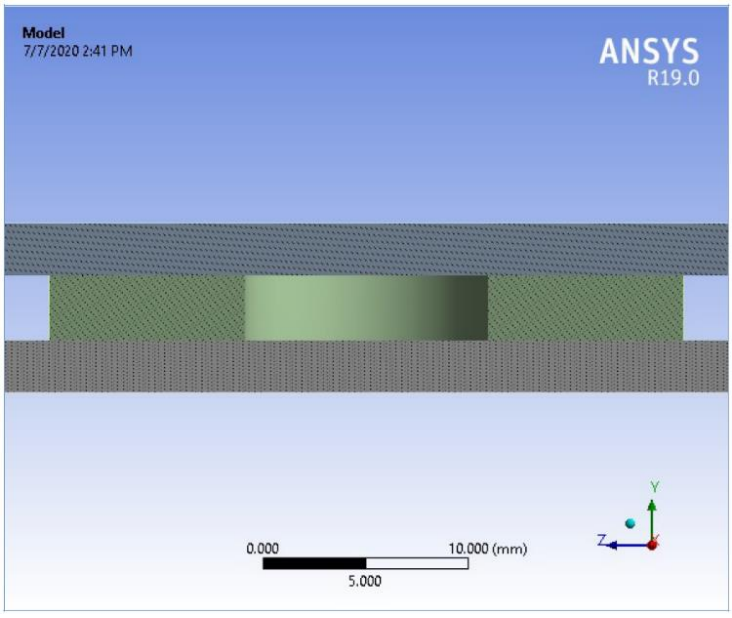

Figure 27: Elastic Model

Four paths were drawn on the cross section of the gasket in order to determine the internal stresses at different points inside the gasket. A representation of this is shown in Fig. 28. The vertical lines represent the paths along the inner and outer diameter of the gasket. These paths start at the point where the gasket meets the bottom plate and proceed upward until they meet the top plate. The horizontal lines represent the paths along the top and center of the gasket. These two paths travel from the outer diameter to the inner diameter.

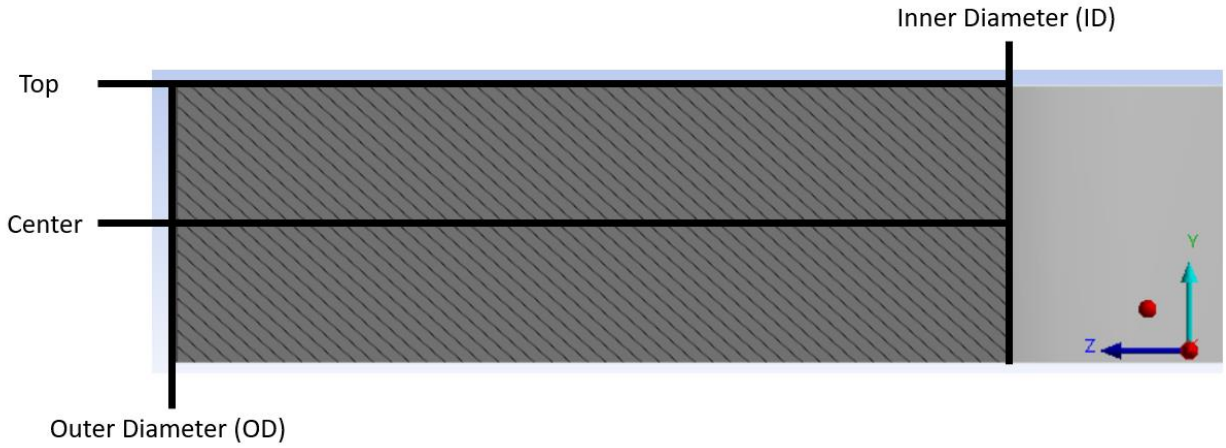

Figure 28: Paths along gasket cross section

Each of the four paths had 100 points where measurements were taken for the desired quantities. Using these paths, the Von Mises stress, the maximum principal stress, the normal stresses in all three cardinal directions, and the shear stresses in the XY and YZ planes could be found.

As the results of a simulation can vary wildly depending on the simulation parameters and material constants used, it was imperative that all of these factors be kept constant. The general model and material properties used in these simulations are given in Table 23. This table defines both the material parameters used, such as the Young's modulus and Poisson's

ratio for all the parts, and certain simulation parameters such as the number of nodes and elements. Using these parameters, the desired stress values could be found along the path for a number of different gasket types.

Table 23: Material and Simulation properties

Property	*Value*
Nodes	4124
Elements	576
Gasket Outer Diameter (OD)	1.22”
Gasket Inner Diameter (ID)	0.47”
Plate Diameter	1.5”
PTFE Density [21]	2200 kg/m^3
PTFE Young’s Modulus	80000 psi
PTFE Poisson’s Ratio	0.42
Steel Density	7750 kg/m^3
Steel Young’s Modulus	2E11 Pa
Steel Poisson’s Ratio	0.3

The boundary conditions for these simulations were as follows. A fixed support condition was applied to the bottom face of the bottom plate and a force of 5000 lbs. was applied to the top face of the top plate in the -Y direction for a duration of 1s. In the frictional case, the gasket was then connected to both plates using a frictional contact condition with a friction coefficient of 1. However, in the frictionless case, the value of the friction coefficient was changed to 0. Using this method, the results below were obtained. As the results for all four types of gasket are virtually identical for this series of simulations, only the results for the 1/8” thick glass microsphere gasket are shown.

Frictionless case:

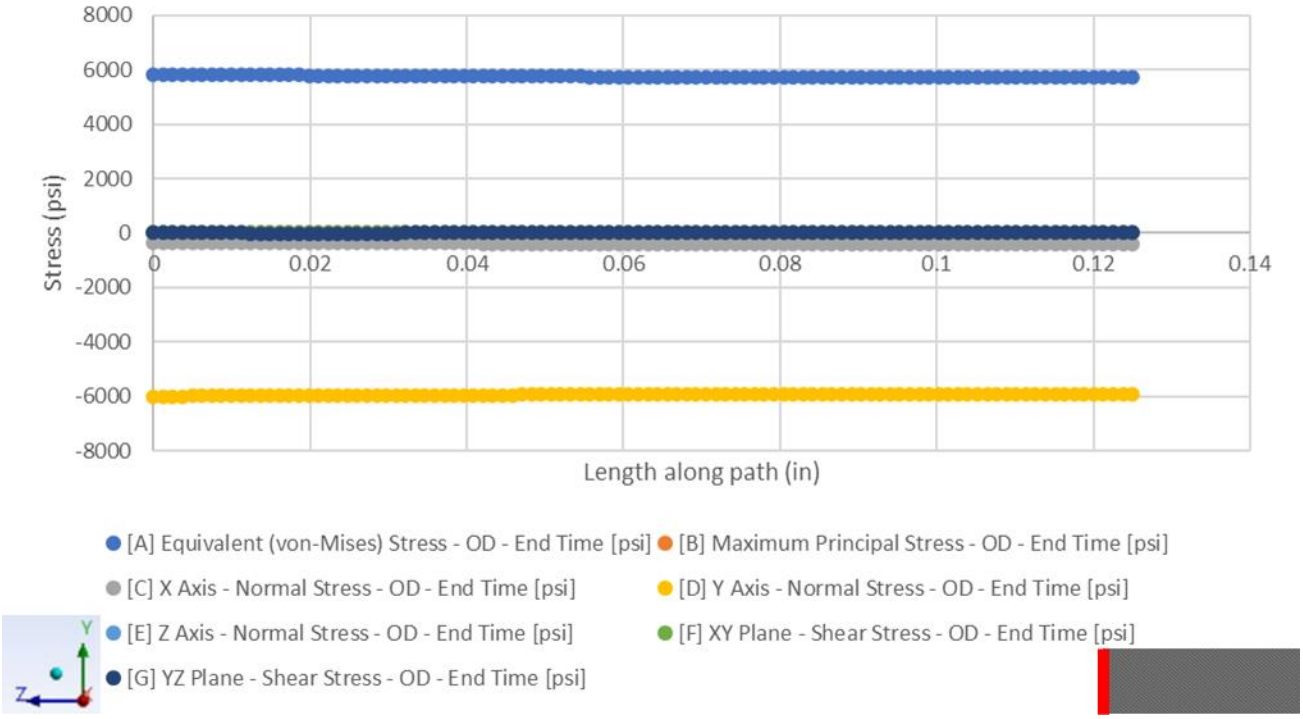

Figure 29: Frictionless case outer diameter stresses

The stress values from the simulations are similar to those that were predicted by the general elasticity equation. As seen in Figure 29, the normal stresses in the X and Z directions are both 0 along the path, as are all of the shear stresses. This outcome is to be expected, as without friction between the plates and the gasket, the gasket is free to slide in the X and Z directions, and thus experiences no resistive internal stresses along those planes or any of the shear planes. That leaves the stress in the Y direction as the only major stress, with a value of -5800 psi. The value of the Von Mises stress essentially mirrors the value of the normal stress in the Y direction, reaching a maximum value of 5800 psi.

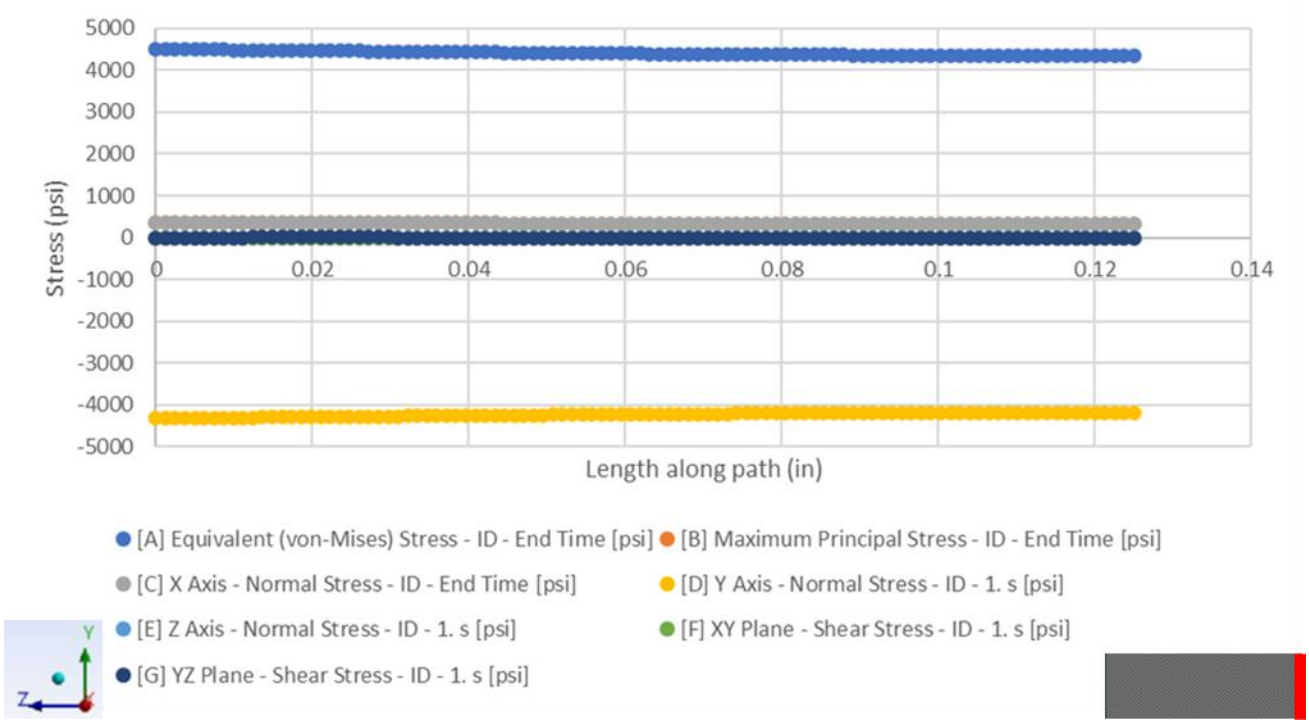

Figure 30: Stresses along the inner diameter for the frictionless case

As predicted by the constitutive equations, the stresses are fairly similar along the inner and outer diameter. Figure 30 shows that the stresses along the inner diameter mostly follow the same patterns as the stresses along the outer diameter, with the only major difference being that the stresses are somewhat lower in magnitude. For example, while the value of the normal stress in the Y direction at the outer diameter was -5800 psi, the value at the inner diameter is -4200 psi.

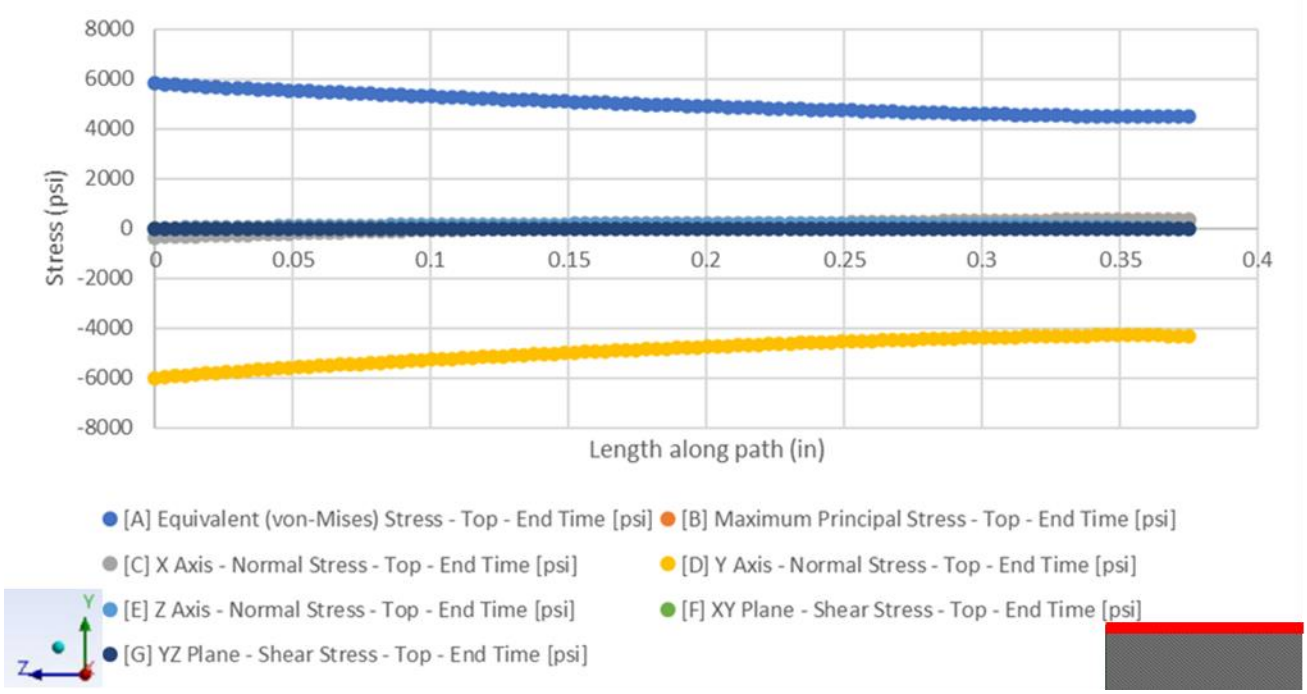

Figure 31: Stresses along the top for the frictionless case

As mentioned previously, the stresses along the top of the gasket were also calculated. The stresses along this path are given the graph shown in Figure 31. As before, since the gasket is free to move in the X and Z directions, the normal stresses in the X and Z directions are 0. The same is again true for the shear stresses in all three shear planes. This means that the maximum principal stress along this path is 0 as well. Again, the stress in the Y direction is the only major stress, starting at a value of -6000 psi and converging to -4000 psi. The value of the Von Mises stress essentially mirrors the value of the normal stress in the Y direction, starting at a maximum value of 6000 psi before converging to 4000 psi.

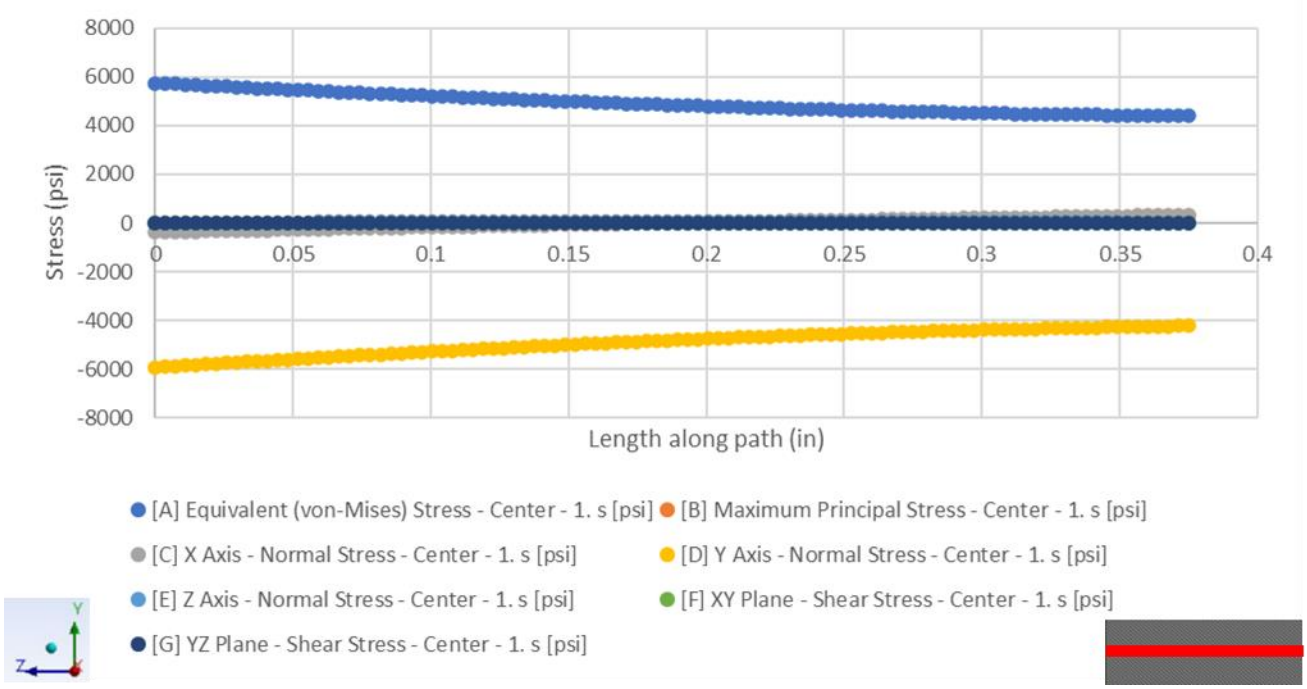

Figure 32: Stresses in the center for the frictionless case

The stresses along the center of the gasket are almost identical to those along the top of the gasket. This can be seen based on the graph shown in Fig. 32. The normal stresses in the X and Z directions, as well as the shear stresses are again 0, while the normal stress in the Y direction is the only major stress. Again, the value of the Von Mises stress mirrors the value of the normal stress in the Y direction, starting at a value of 6000 psi and converging to 4000 psi.

Frictional case:

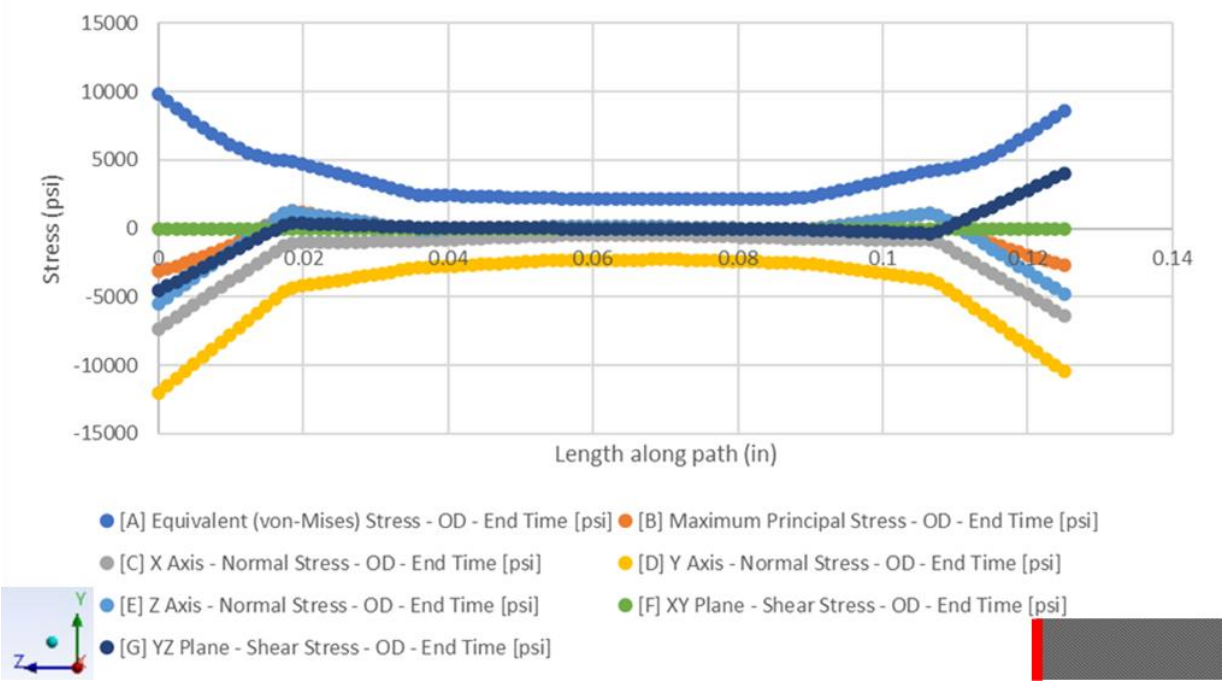

Figure 33: Stresses along the outer diameter for the frictional case

As predicted by the theoretical model, the stresses at the outer diameter seem to be mostly symmetric about the center. Figure 33 shows that the normal stresses in the X and Z directions start out at high negative values near the edges of the gasket and converge to zero near the center. This pattern is also seen with the maximum principal stress. Meanwhile, the normal stress in the Y direction starts out at an extremely high negative value (likely due to increased stress concentration at the plate/gasket boundary) and converges to a value of about -2300 psi near the center. This pattern is also seen in the values for the Von-Mises stress, with the only difference being that the values are positive. The shear stress in the YZ plane appears to follow a tilted Z shaped pattern, again having higher values near the edges, while converging to 0 about the center. Finally, the shear stress in the XY plane remains close to 0 along the length of the path.

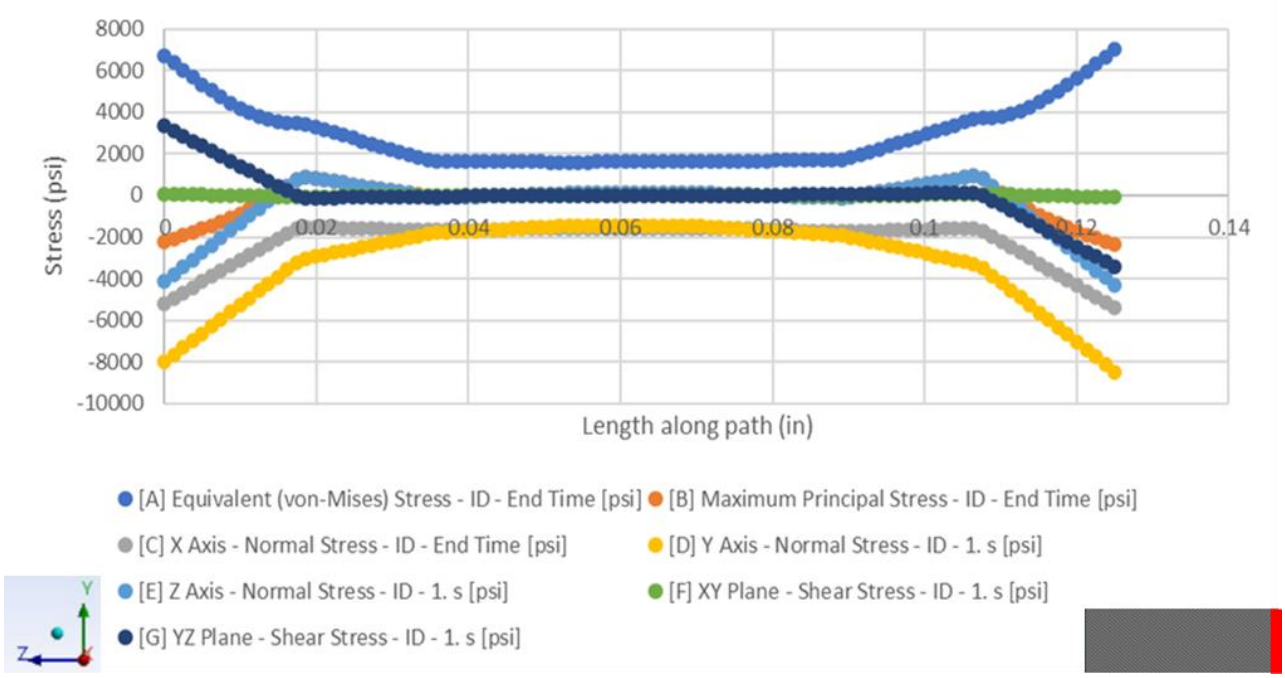

Figure 34: Stresses along the inner diameter for the frictional case

The pattern seen in the frictionless case repeated itself here, where the stresses along the inner diameter mostly follow the same patterns as the stresses along the outer diameter. This can be seen in Fig. 34. Comparing this graph with the one seen in Figure 33, it can be seen that the only major difference is that the stresses are somewhat lower in magnitude. This fits with the results predicted by the general elasticity equation as the gasket deformed less at the inner diameter than at the outer diameter, leading to comparatively lower stresses in this area.

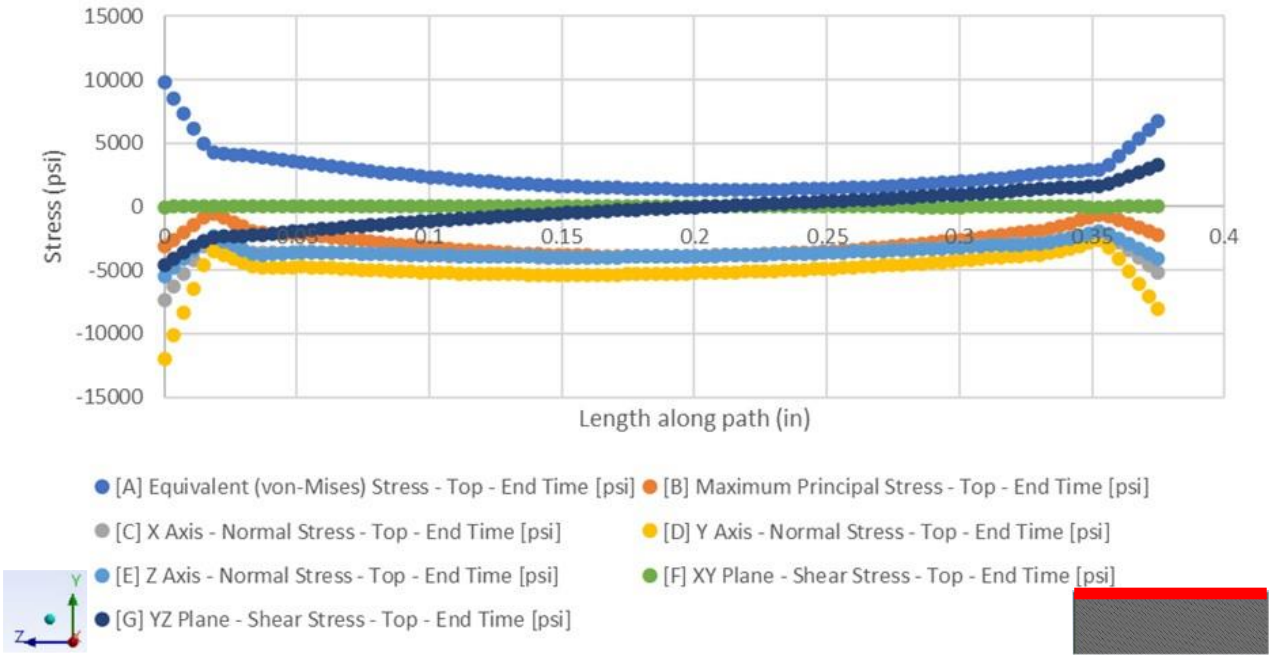

Figure 35: Stresses along the top for the frictional case

Some of the patterns in the stresses seen at the inner and outer diameters are repeated here as well. Figure 35 shows that the Von-Mises Stress along the top appears to follow the same trend as the stresses along the inner and outer diameters. It has a high value along the edges but converges to a lower value at the center. Also, the shear stress in the XY plane is zero along the entire path in this case as well. However, from there, the patterns start to diverge. Discounting the stresses at the very edge of the gasket, the normal stresses in all 3 directions as well as the maximum principal stress follow the same pattern. All 4 values start off near zero, before reaching a peak near the center. Meanwhile, the shear stress in the YZ plane follows a similar curve to the one shown before, with the stress reaching equal and opposite values near the edges and converging to zero near the center of the path.

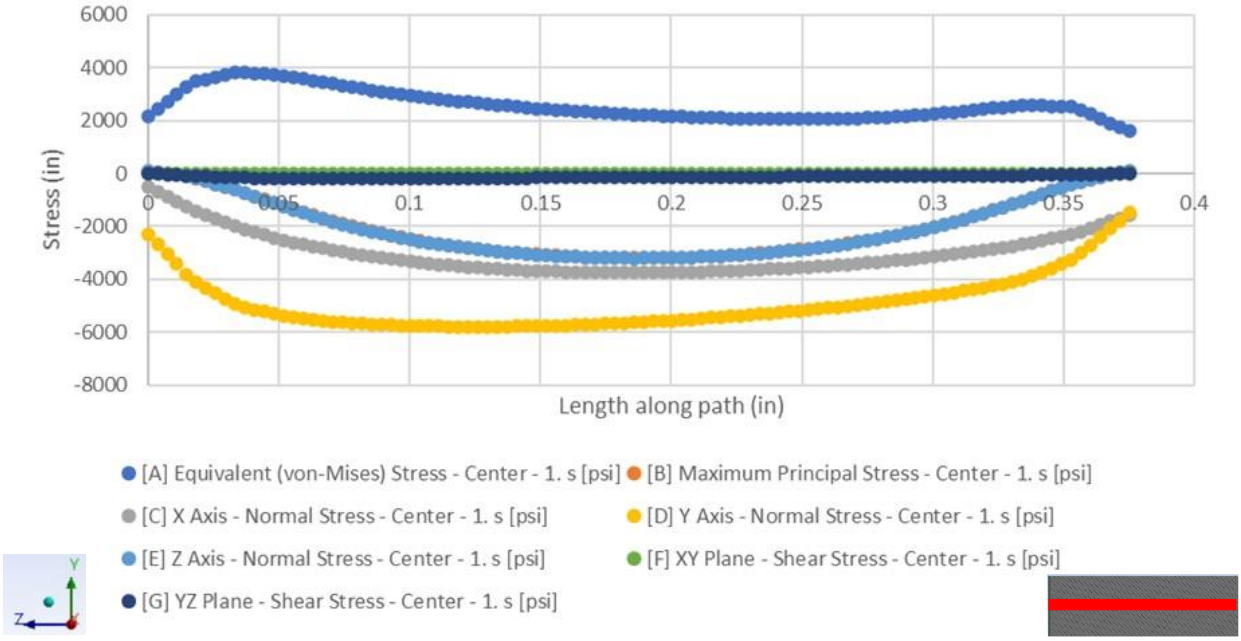

Figure 36: Stresses in the center for the frictional case

As with the frictionless case, a lot of the stress patterns seen in the top path can be seen in the center path as well. As seen in Fig. 36, the normal stress in the X, Y and Z directions along the central path follow roughly the same patterns as along the top path, starting out at zero and reaching their peaks near the middle of the path. However, these stresses are far more spread out than those of the top path, with the normal stress in the Y direction having a far larger magnitude than either of the other stresses. The pattern of the Von Mises stress also appears to be the opposite of what was previously observed. The peaks in the Von mises stress are closer to the center, and the values converge to zero at either edge. Finally, the values for the shear stress in the YZ plane, the maximum principal stress, and the shear stress in the XY plane are all zero along the entirety of the path.

Summary:

The results for both the frictional and frictionless cases closely match the theoretical shapes of the stress curves. For the frictionless case, the normal stresses in the X and Z directions, as well as the shear stresses should be 0 along all of the paths, and that matches what was seen in the simulations. This happens because without friction between the plates and the gasket, the gasket is free to slide in the X and Z directions, and thus experiences no resistive internal stresses along those planes or any of the shear planes. Therefore, as seen in the graphs for that section, the only major stresses on the gasket should be the normal stress in the Y direction and the Von Mises stress. The magnitude of these stresses on the top and center paths starts near 6000 psi (1.5X the applied stress) before decreasing to around 4200 psi. For the paths along the inner and outer diameter, these stresses remain at 6000 psi along the path.

The results for the frictional cases also follow the expected patterns. The values for almost every stress along the top, inner diameter, and outer diameter paths peak at either end of the path, where the gasket meets the plate. As the friction between the gasket and the plate causes the gasket to deform and bend in on itself, the stress is concentrated in those locations. These stress concentration zones cause the stress to be multiplied by a factor of 2-3 at the very edges, before decreasing to normal levels at a set distance along the path. For the paths along the inner and outer diameter, the elevated stresses fade away at about 0.019” along the path, or at about 15% of the path length. For the path along the top, the increased stresses disappeared at around 0.025” along the path, which was about 8% of the path length. This can be seen in the sketch displayed in Fig. 37. Here, the areas highlighted in red show the zones of increased stress concentration in the gasket.

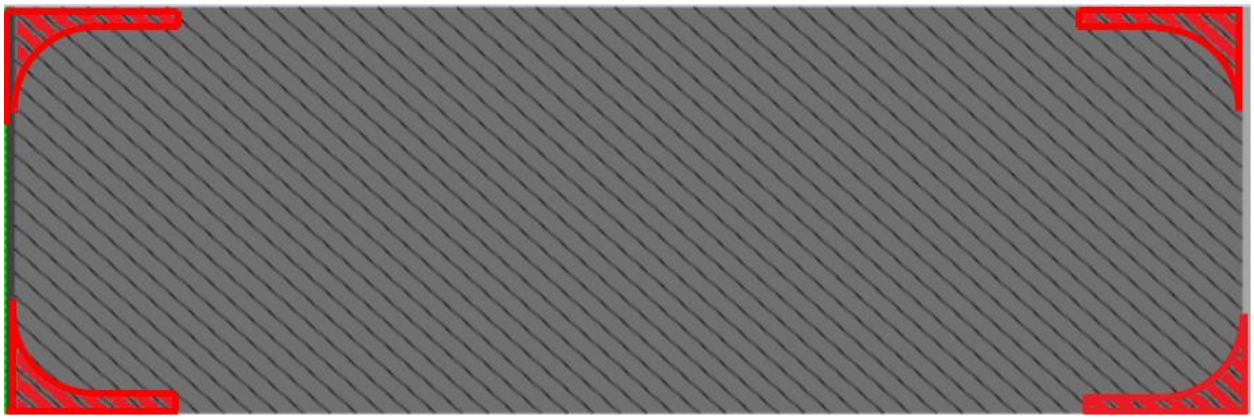

Figure 37: Regions of high stress concentration

In these regions, the stress reached a maximum of 15000 psi, or 3x the applied force. However, closer to the middle of these three paths, all of the stresses dropped below the applied stress of 4651 psi.

Along the center path, which has no contact with the plates, the stresses are 0 at either end and peak around the middle. The largest of these stresses is the normal stress in the Y direction, which peaks at about -5800 psi, or 1.5X the applied stress. The shear stress in the XZ plane being 0 along all of the paths is due to the fact that the cross section being examined is in the YZ plane, so in that location there is no shear along the XZ plane. If the cross-section were in the XY plane, then the shear stress in the YZ plane would be 0 instead. It also makes sense that the stresses at the inner diameter have similar shapes but lower values than the stresses at the outer diameter. Both paths have the same boundary conditions at both ends and are exposed to the same load so the load curves should be similar. However, the inner diameter deforms less than the outer diameter, so the stresses at the inner diameter are lower as a result.

Among the other differences between the frictionless and frictional cases was that the gasket deformation pattern between the two was quite different as well. A sketch of both patterns is shown in Fig. 38. Here, the light-yellow silhouettes represent an undeformed gasket, while the darker shapes represent the deformed gaskets. In both cases, the gaskets have the same final thickness, but have different deformation profiles.

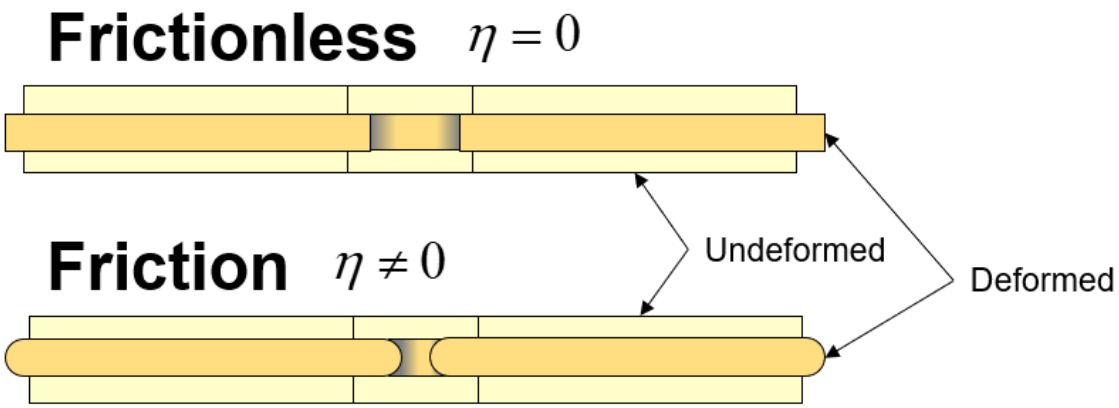

Figure 38: Deformation profiles for the frictional and frictionless case

As mentioned previously, the friction between the gasket and the plate causes the gasket to deform inwards on itself. This creates a bulge at the inner and outer diameters of the gasket where none exists in the frictionless case. This deformation pattern is likely responsible for the high stress concentrations in these areas. The results and patterns seen in this set of elastic simulations can be used to verify the results of the viscoelastic model discussed in Section 7.3.

7.2 Deformation Testing

To support the viscoelastic modeling efforts on this project, a series of stress-deformation experiments were also performed. These experiments used the setup shown in Figure 39 to collect both stress and deformation data. It consisted of a miniature gasket,

having an inner diameter of 0.44” and an outer diameter of 1.25”, clamped between two square platens using a single nut and bolt assembly. As before, the clamp load was measured using a Futek load cell that recorded data at 1 hz, and the deformation of the gasket was measured using an MTS extensometer. Analog signals from both the load cells and the extensometer were transmitted to a National Instruments data acquisition device via a USB cable. This data could then be read and processed using another custom-built Graphical User Interface (GUI).

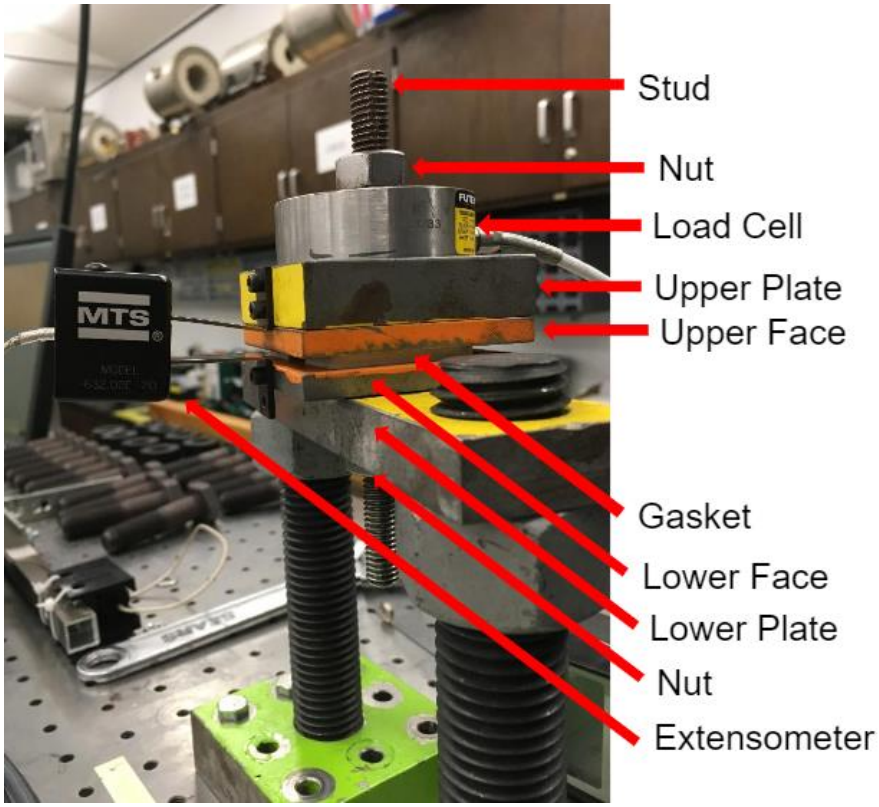

Figure 39: Extensometer test setup

Despite the test device being so different from the mock flange, the testing procedure was fairly similar. To start a test, the setup is first disassembled, and the gasket is placed on

the bottom plate. The apparatus was then reassembled, and the bolt was then tightened to a final torque of 33 in-lb. The test then continued until the limit of 1 hour.

These tests allowed for the collection of load and deformation data that was in turn used to calculate the elastic and bulk moduli for different types of gaskets. The exact procedure for these calculations is discussed in more detail in Section 7.3, where the steps to derive the material model are explained. A sample load curve for this data is shown in Fig. 40.

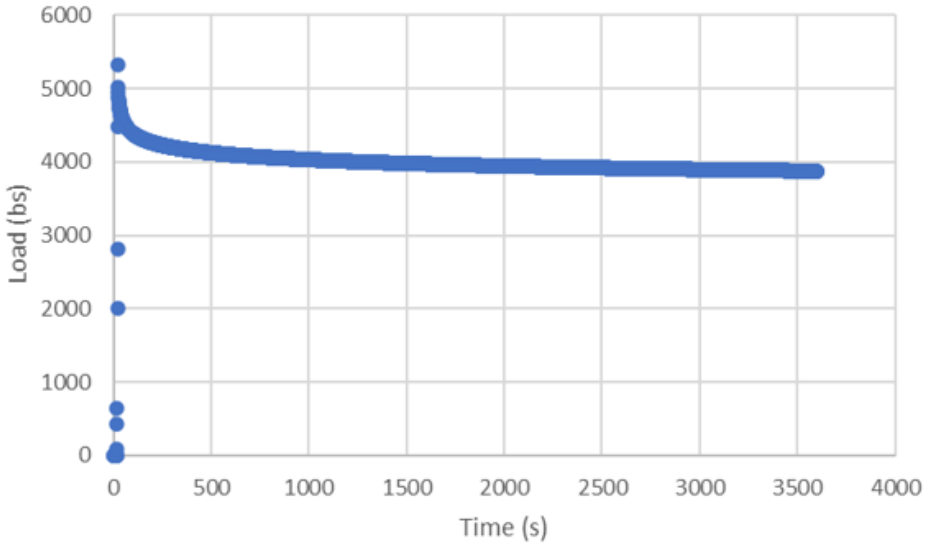

Figure 40: Sample load relaxation curve for deformation experiments

As shown in this load curve, the data collected from this series of experiments is extremely similar to that collected in the high temperature and pressure experiments. The force spikes as the initial load is applied, the decays to the eventual relaxed load. However, there is one key difference, the initial loads applied to the gasket are much lower in these experiments as the setup was only torqued to 33 in-lb. However, this was still enough to create significant strains in the gasket and create a proper seal, as shown in the deformation curve in Fig. 41.

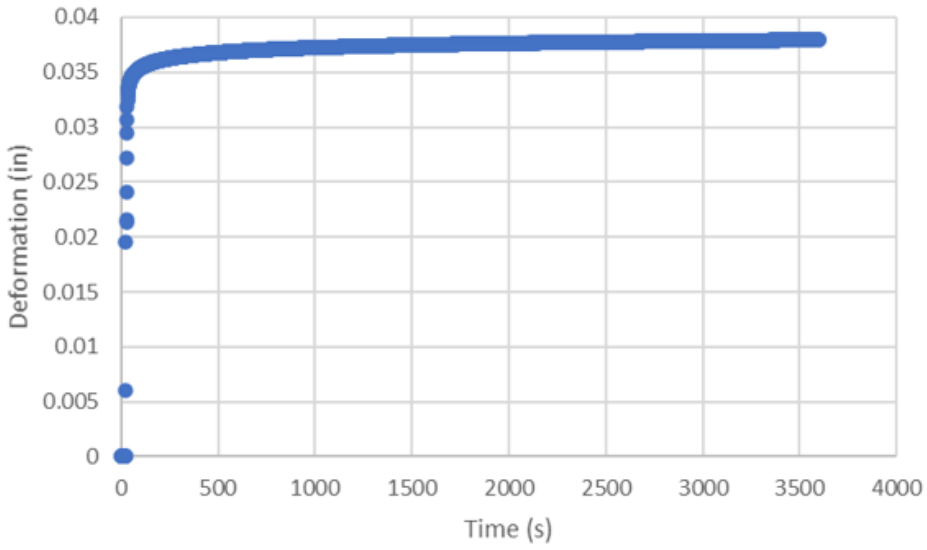

Figure 41: Sample Deformation Curve

This deformation curve shows the typical deformation behavior for a gasket under this set of loading conditions. As expected, there is a sharp increase in deformation as the initial load is applied, and the deformation gradually reaches an asymptote as the gasket relaxes. Using these two types of data, stress-strain curves for the different types of gaskets could be produced, which allowed the Young's modulus for the different gasket materials to be derived. These experiments provided the foundation for the modeling efforts discussed in Sections 7.3 and 7.4.

7.3 Viscoelastic modeling

As the main aim of this simulation effort is to create a framework for the analysis of advanced gaskets, a 6-step process was developed to be able to model different types of gaskets. A simplified diagram of this process is shown in Fig. 42. Using this process, it is possible to take the data collected in the experiments described in Section 7.2 and use it to create a viscoelastic material model. The latter half of this process will also allow the model

to be applied to gaskets that have different textures or any other unique design characteristics.

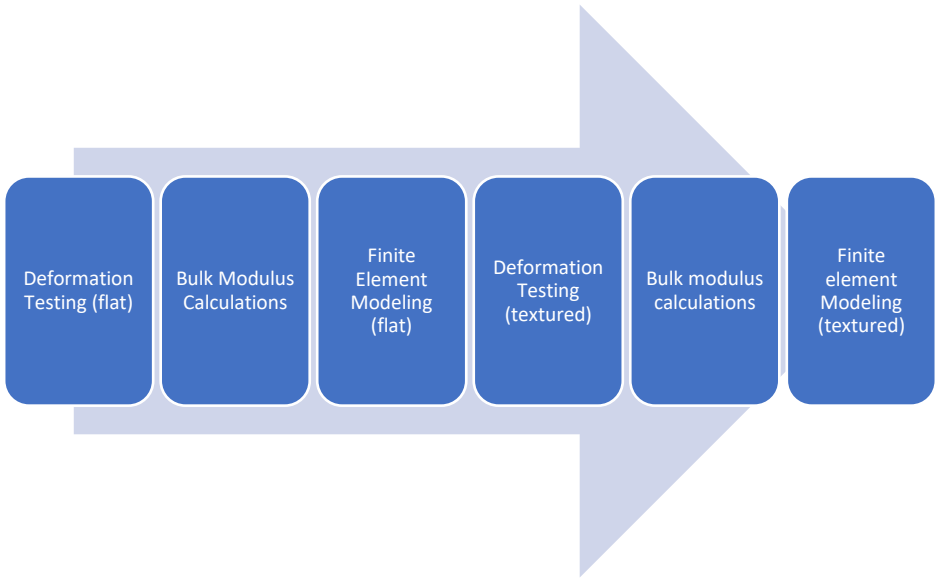

Figure 42: Diagram of information flow in the modeling process

The first step in this process was to conduct the types of deformation experiments described in Section 7.2 on flat gaskets in order to obtain both the load and deformation data. Next, the data was processed using the methods provided in this section to provide a base for the material model. A series of time-dependent simulations, also discussed in this section, were then performed using a flat gasket model to see if the material model was accurate. With the model developed and tested on the flat gaskets, its accuracy with respect to the textured gaskets needed to be validated. As before, load-deformation experiments were performed to gather data, which was then processed to create the material model. Finally, the accuracy of the model was tested on the textured gaskets, as described in Section 7.4.

Using this process, the time-dependent viscoelastic simulations could now be completed. The model used in these simulations was the same as the model used in the elastic simulations. A cross sectional view of the gasket model is shown in Figure 43.

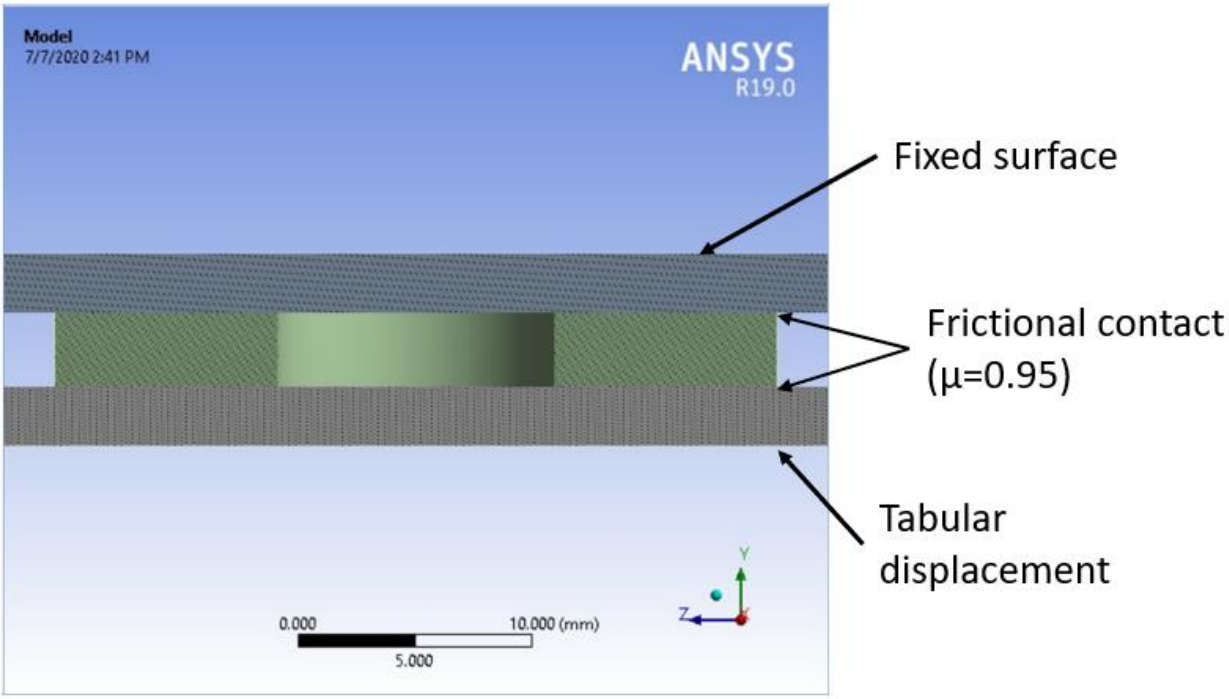

Figure 43: Gasket model used in the viscoelastic simulations

Even though the same STEP file was used to model the flange, the contact and boundary conditions were obviously quite different. The top face of the top plate was fixed, while the bottom face of the bottom plate had a displacement boundary condition applied that mimicked the deformation curve from one of the experimental tests. Furthermore, instead of having the simulation only last one second, these simulations sought to simulate gasket behavior over an entire hour. Finally, the contact between the gasket and the plates was changed from a bonded condition to a frictional contact with a friction coefficient of 0.95. Using this combination of geometry and boundary conditions, the stresses could be found throughout the flange along with the force reaction at the fixed face of the plate.

Aside from the model and the boundary conditions, the other key factor in these simulations was the viscoelastic material model. Using the force and deformation results from Section 7.2, it is possible to construct a viscoelastic material model that accurately the load relaxation behavior of certain types of gaskets. As mentioned in the introduction of this thesis, this method is a combination of the methods used by Williams (2017) and Bharadwaj (2019). It relies on the use of Burger's model in ANSYS to capture both the loading and unloading behavior of certain types of gaskets. However, ANSYS cannot use Burger's model directly, so a Prony series approximation based on the bulk modulus is required. The general equation for the Prony series that uses the bulk modulus is

$$\mathrm{K(t)} = K_0 \left[a_m^K + \sum_{i=1}^{n} a_1^k e^{\frac{t}{\tau^n}} \right] \tag{10}$$

where K_0 is the initial bulk modulus (in psi), t is the time, τ is the time constant, n is the maximum index, and a^k is the Prony series constant [22].To get the bulk modulus data required for this Prony series curve fit, the data files for a particular test had to be referenced. By using the force and deformation data from the deformation experiments, the stress and strain at each time can be calculated via

$$\sigma = F/A \tag{11}$$

$$\varepsilon = \Delta L/L_0 \tag{12}$$

where F is the measured load in lbs., A is the cross-sectional area of the gasket as viewed from the top, ΔL is the change in gasket thickness, and L is the initial gasket thickness. These stress and strain values can in turn be used to calculate $E(t)$, the elastic modulus at each point in time, using the linear elasticity equation

$$E = \sigma/\varepsilon \tag{13}$$

The Young's modulus values are then used to calculate the bulk modulus '*K*' via Eqn. 14. Here, *v* stands for the Poisson's ratio of the material.

$$\mathrm{K} = \frac{E}{3*(1-2v)} \tag{14}$$

Now, these bulk modulus values are used to calculate the Prony series relaxation constants using the built-in curve fit feature in ANSYS. The average Prony coefficients from several tests for each material are shown below in Table 24. The Prony series approximations were carried out to three terms in order to fully capture the behavior of the graph during its unloading step.

Table 24: Material and Prony series constants

		Index					
		1		2		3	
Material	E(0) (psi)	a	t (s)	a	t (s)	a	t (s)
1/8" Blue	6500	0.166	0.78	0.168	2.23	0.188	200.21
1/8" White	9300	0.172	0.77	0.168	2.28	0.212	223.26
1/16" Blue	10720	0.166	0.78	0.193	1.23	0.271	186
1/16" White	14500	0.084	978.46	0.079	72.29	0.075	5.89

There are a few general trends that can be seen in the values of the constants. For one, all of the materials have Prony constants spread out across the duration of the test to capture the different behaviors at each time. The constants obtained near the 1 second mark control the shape of the curve during the initial dip, while the constants near the 2 second mark fix the shape of the curve near the beginning of the change in slope. Finally, the constants past the 100 second mark fix the shape of the curve at longer time intervals. It also appears that

the white materials are stiffer than their blue counterparts as they have a higher initial young's modulus.

By using these constants to define the material and the displacement values from the experimental data for the displacement boundary condition, the accuracy of the material model can now be verified. The results for the viscoelastic modeling simulations are shown below. Figure 44 displays the real and simulated load curves for a 1/8" thick gasket filled with glass microspheres. The hollow red circles represent the experimental data points, while the black line represents the results of the simulation. This figure should help convey the performance of the model.

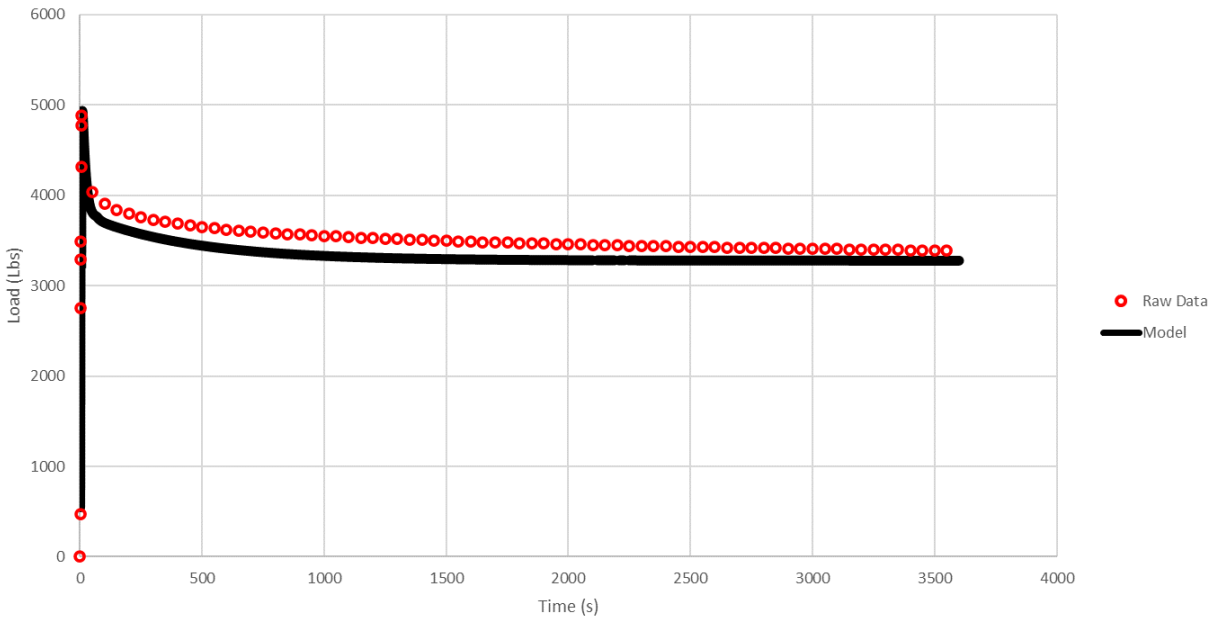

Figure 44: Load Curves for a 1/8" thick glass microsphere gasket

From Figure 44, it is clear that the model is fairly effective at modeling the material behavior during both loading and unloading. For the case shown above the model managed to replicate the data with an R^2 value of 0.84. This is a fairly strong correlation, but there are still areas

where the model can be improved. For one thing, the force values in the simulated curve appear the drop far more quickly than those from the experimental data. To fix this problem, a higher order Prony series approximation could be used as it would better approximate the shape of the curve in those locations. However, despite this shortcoming, the fact that the R^2 value is relatively high means that this model is sufficient for use in further applications.

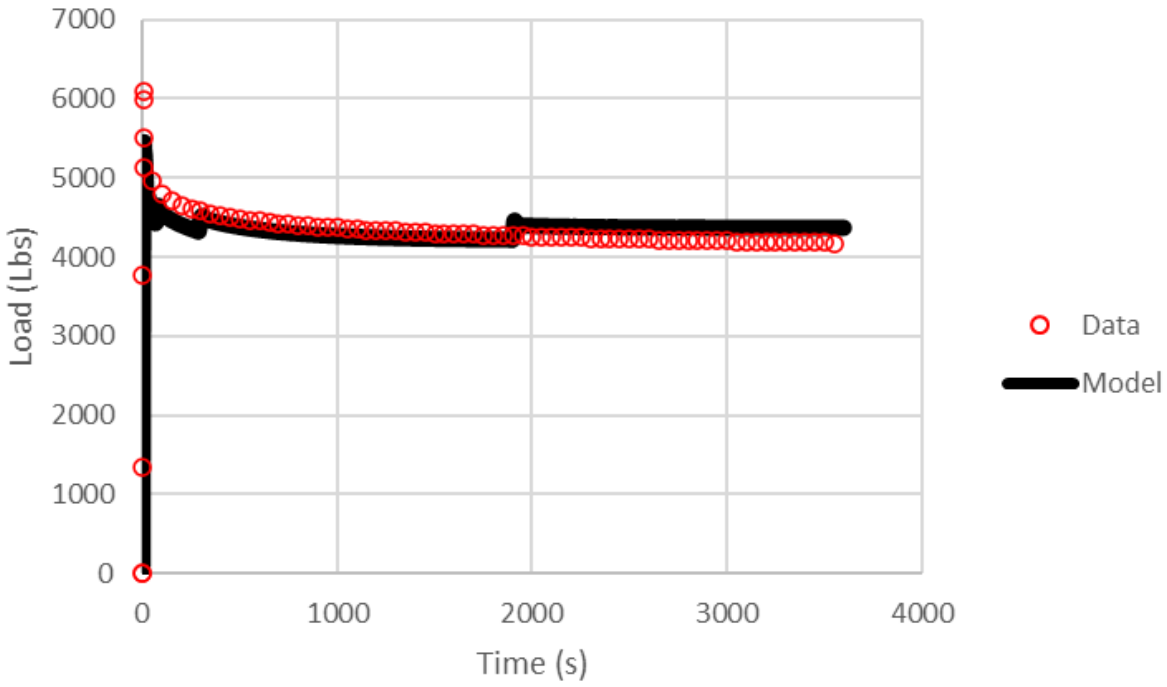

Figure 45: Load curve for a 1/8" thick gasket filled with barium sulfate

As mentioned previously, the modeling approach was used to model the performance of several different types of gaskets. Figure 45 shows the simulation results for a 1/8" thick gasket filled with barium sulfate. For the case shown above the model managed to replicate the data with an R^2 value of 0.926. This is an extremely strong correlation, but even so there are still areas where the model can be improved. The force values in the simulated curve have significant jumps at 250s and 1900s. This is likely because the deformation curve used

to describe the displacement boundary condition had sharp jumps in the deformation data, which was erroneously translated to mean that the gasket was being subjected to another load. This issue will likely be fixed if another deformation curve is used. However, the relatively high accuracy means that this model can be used for further applications.

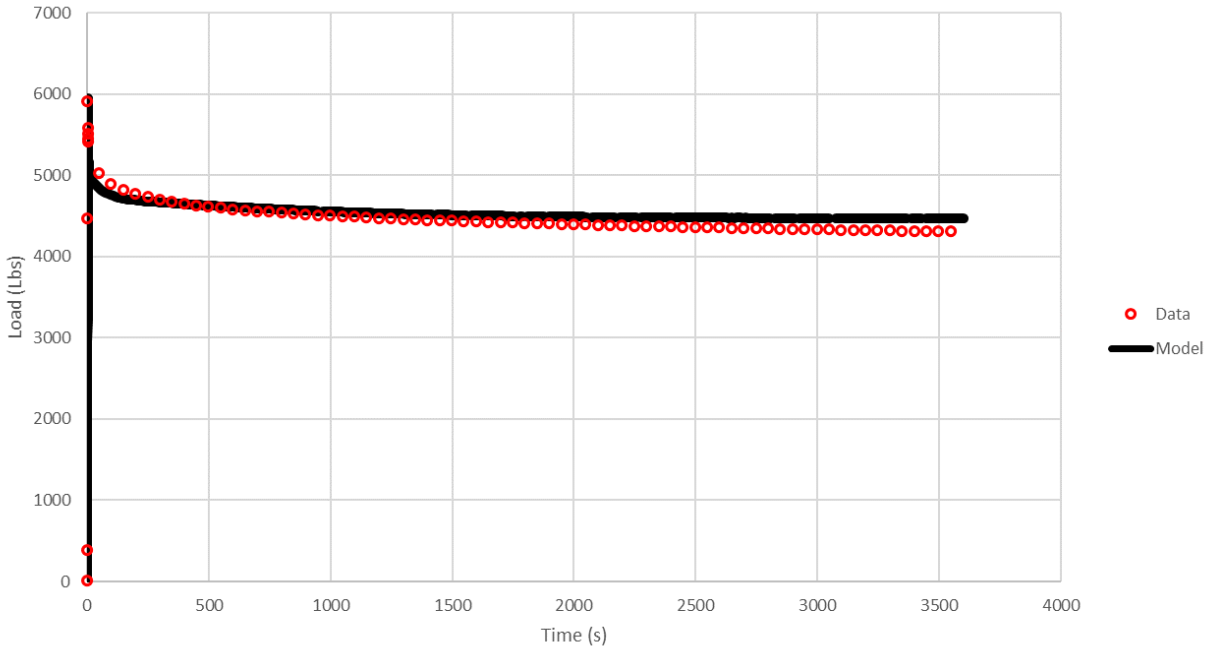

Figure 46: Load Curve for 1/16" thick gasket filled with Glass Microspheres

The performance of the modeling approach improved somewhat when applied to the 1/16” gaskets. Figure 46 shows the results for a 1/16” thick gasket filled with glass microspheres. For the case shown above the model managed to replicate the data with an R^2 value of 0.961. This is the strongest correlation that has been observed in this series of experiments meaning that the constants for this material can be used in other applications. However, some of the same shortcomings seen in earlier simulations can be seen here as well. For one thing, the load drops somewhat sharply at the beginning, and flattens towards the end. These two issues could be solved by increasing the order of the Prony series

approximation to account for the behavior at the start and deriving those coefficients from data taken from longer term experiments to account for the behavior at the end.

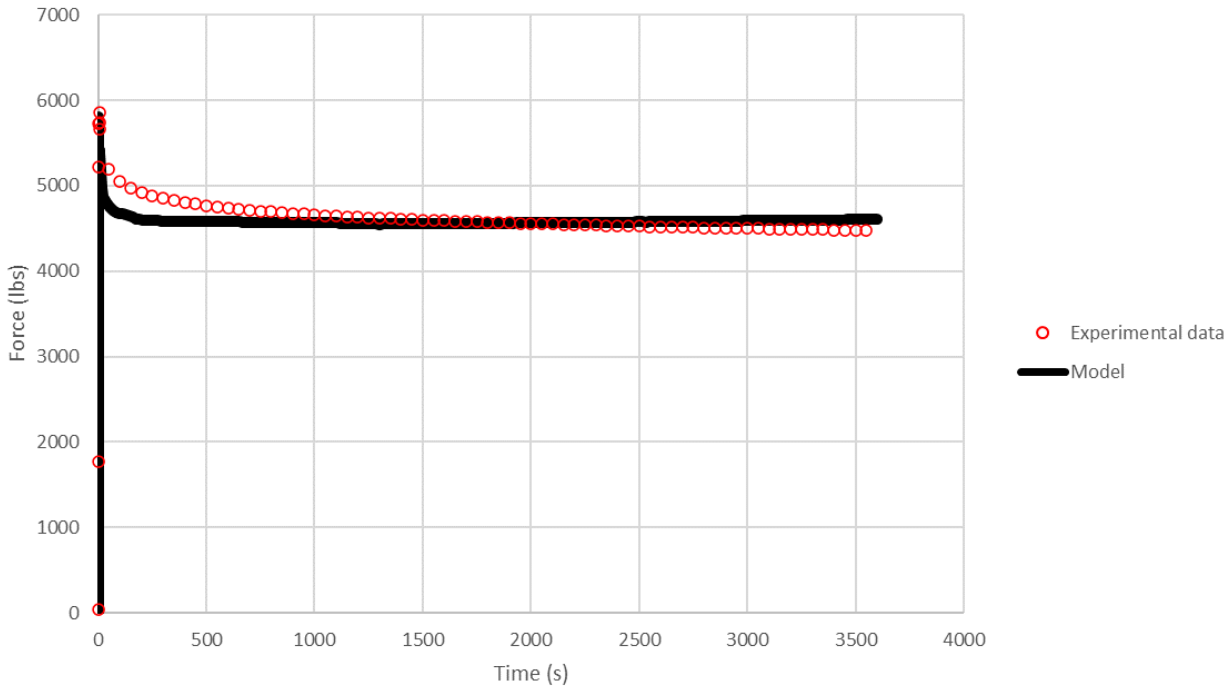

Figure 47: Load curve for 1/16" thick gasket filled with barium sulfate

The final series of simulations in this section was for a 1/16" thick gasket filled with barium sulfate. The load curve for these simulations is given in Fig. 47. As with the previous case 1/16" gasket, the load curve in the simulated data dropped more sharply than the experimental data before smoothing out. In this case, the model managed to replicate the data with an R^2 value of 0.89. However, it seems that the performance of this particular model will become more inaccurate as the time increases. As with the previous curve these issues could be fixed by increasing the order of the Prony series and deriving those coefficients from data taken from longer term experiments.

With all of these simulations complete, it can be said that the material model presented in this thesis is fairly accurate at modeling the behavior of these gaskets under the specified loading conditions. A summary of the overall simulation results is given in Table 25. This table lists all of the relevant characteristics of the simulated load curves, such as the R^2 value, the maximum load, and the load at the end of the simulation.

Table 25: Simulation results

Material	R^2	F_{max} *(lbs.)*	*F (1hr) (lbs.)*
1/8" Blue	0.847	4971	3381
1/8" White	0.926	5712	4780
1/16" Blue	0.961	5980	4730
1/16" White	0.891	5886	4854

The trends shown in this table closely mimic those seen in the experimental results discussed in Chapter 5. The load loss between the maximum and final loads is higher in the thinner gaskets than the thicker ones. However, one thing to note is that in these simulations, the load loss between the white and blue materials is almost identical, while in the experimental tests the blue material experienced slightly less load loss. This discrepancy may be because the material model was slightly more accurate when modeling the white material. Finally, the R^2 values listed in the table show that in almost all cases, the model surpassed the 0.85 threshold that denotes a strong correlation between the model and the experimental data. This confirms that the material model defined in this section is viable for use in modeling traditional gaskets. However, the applicability of the model to textured gaskets still needs to be verified. This will be done in Section 7.4.

7.4 Textured Gasket Modeling

After having verified the accuracy of the viscoelastic material model on flat gaskets, it was then necessary to test whether the model could be applied to gaskets with unusual geometries. However, this task presented a new set of challenges. For one, the small, raised surfaces of the gasket required a much finer mesh in order to avoid the elements becoming heavily deformed. Therefore, an extremely fine mesh was applied to the peaks of the gasket by using a named selection to specify the boundaries and size of the mesh. This also required the model to be revised as shown in Fig. 48. The model was cut into a quarter of the model used for the simulations of the flat gaskets to reduce the computational cost required to run the simulations.

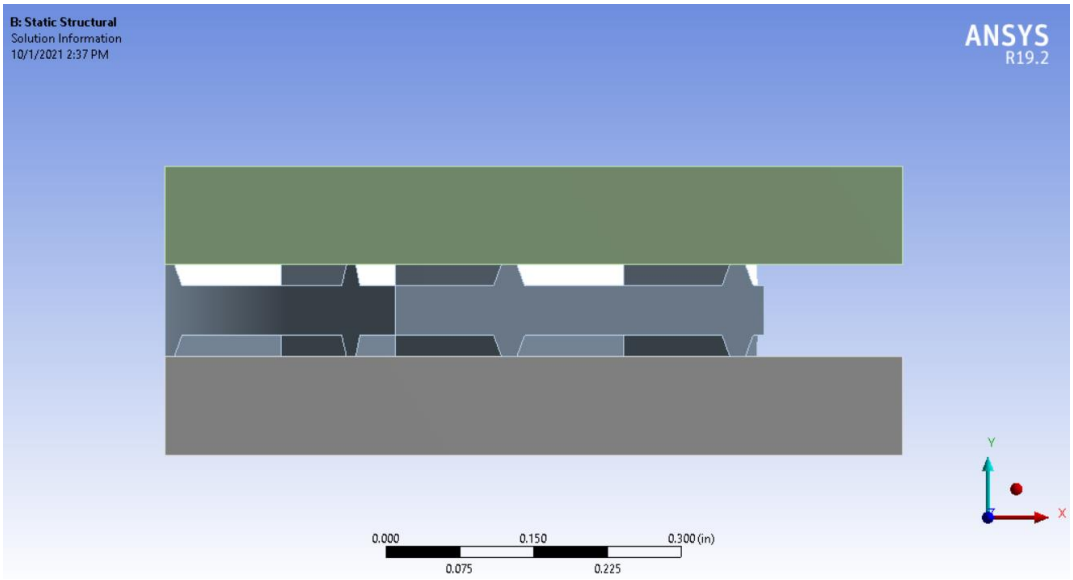

Figure 48: Textured gasket model

By using this model with two symmetry regions in the X and Z directions it was possible to simulate the behavior of the gasket properly. However, it should be noted that the force reaction results yielded by this model will be a quarter of what they should be, given that the

gasket only has a quarter of the usual surface area. For this reason, the load curves from the model presented later in this section will be multiplied by 4 in order to reflect the true value.

Another problem that surfaced was the fact that the initial contact stiffness specified by ANSYS caused the simulations to fail as the program could not keep up with the relatively large degree of deformation. Therefore, the contact stiffness was reduced from a factor of 1 to a factor of 0.04. Using this method did allow for somewhat increased penetration between the contact regions, but so long as the penetration does not exceed 1% of the applied displacement, the effect of the increased penetration on the accuracy of the simulation is negligible [23].

The last issue that arose when trying to perform the simulations was that the default number of iterations used by the ANSYS APDL solver was insufficient. This often caused convergence failures as the program could not find an acceptable solution within the specified number of iterations. To remedy this, an ANSYS APDL command was inserted that changed the maximum number of iterations allowed to 100. With all of these problems rectified, the performance of the model on the textured gaskets could finally be verified.

Despite the problems listed above, the application of the viscoelastic material model essentially followed the same process listed in Section 7.3. Based on the force and deformation curves from the tests discussed in Section 7.2, the average Prony series and material constants were found for each type of gasket. A list of all of these material constants is given in Table 26.

Table 26: Material and Prony series constants for textured gaskets

		Index					
		1		2		3	
Material	E(0) (psi)	a	t	a	t	a	t
3/32" Blue	6500	0.123	2.20	0.088	48.9	0.091	836.77
3/32" White	7800	0.172	0.77	0.168	2.28	0.212	223.26

Using these average constants, the viscoelastic properties could be applied to the gasket model. The results of the simulations for different types of gaskets are shown below, starting with the results for the blue material in Figure 49. Here, the experimental results are shown by the red circles, while the results of the model are shown by the black line.

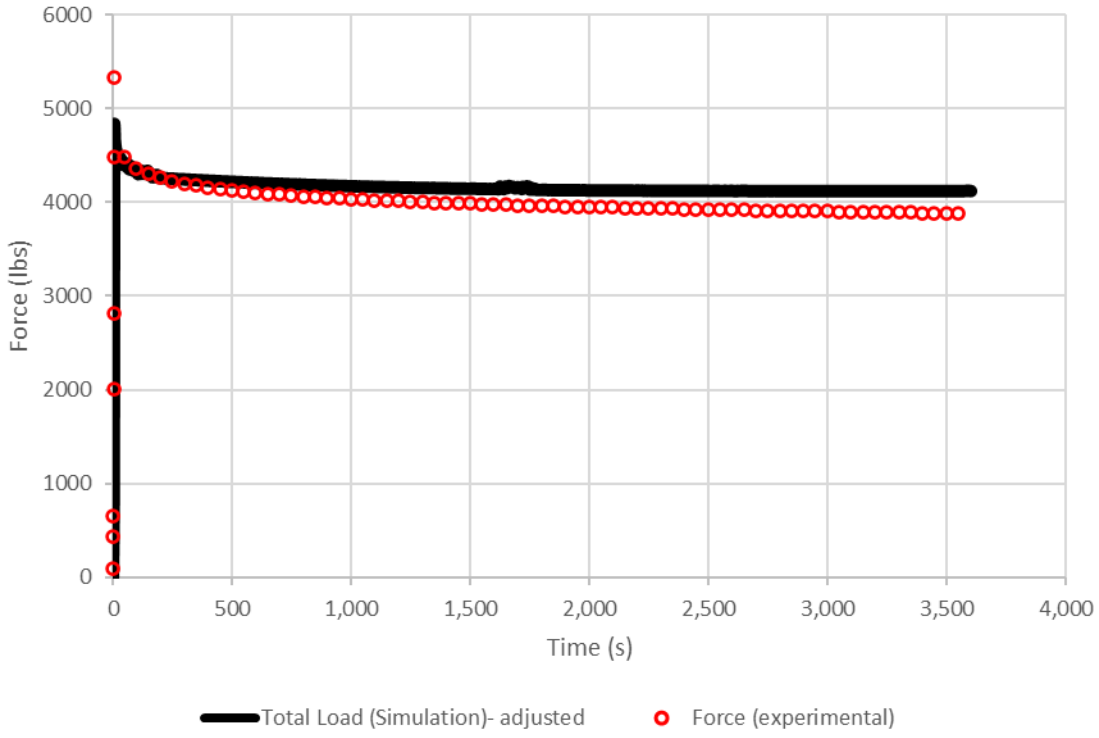

Figure 49: Simulation results for a textured gasket filled with glass microspheres

As seen in Figure 49, the material model seems to be quite accurate, reaching an R^2 value of 0.82 even when applied to the textured gaskets. For this particular load curve, the

accuracy of the curve seems to be almost perfect near the beginning, but it does deteriorate somewhat towards the end. As with the load curves for the flat gaskets, the simulated load curve appears to flatten somewhat faster than the experimental data. Again, this could be fixed by using longer duration tests to determine the Prony series constants.

The final series of simulations in this thesis is for the textured gaskets filled with barium sulfate. The results of this simulation are shown in Fig. 50. Again, the experimental results are displayed as red circles and the simulation results are shown by the black line. This figure helps illustrate the accuracy of the model.

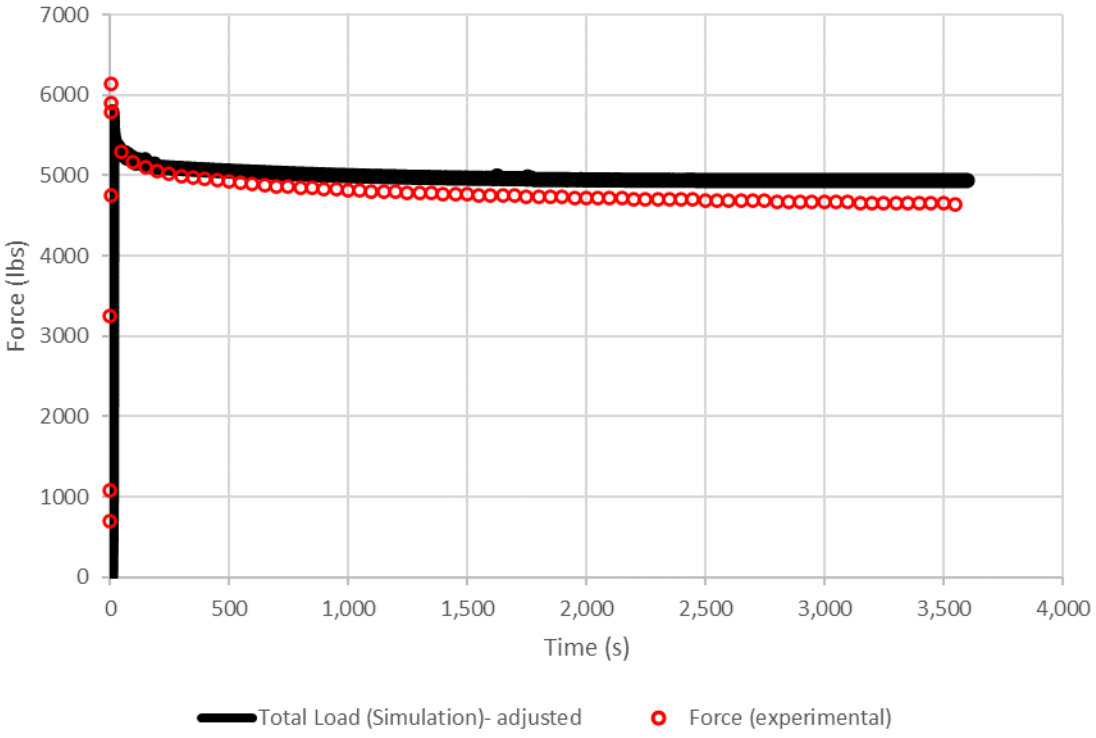

Figure 50: Simulation results for a textured gasket filled with barium sulfate

The results of the simulation indicate that the model is also accurate for the textured white gaskets, having an R^2 value of 0.87 with respect to the experimental data. In this case, the

model appears to flatten out a bit earlier than in Fig. 49, leading to increased error near the end of the test. However, as this error is only on the scale of 300-400 lbs., it can still be said that this model is fairly effective in predicting gasket behavior. The recommendations made earlier in Section 7.3 will most likely help alleviate the issues with this model as well.

There are a few general trends that can be seen from examining the simulated load curves and the material coefficients. First, the elastic modulus values for the textured gaskets are somewhat lower than those of the flat gaskets made from the same material. This is somewhat surprising albeit not impossible as the Young's modulus for PTFE can vary wildly depending on whether the material is being subjected to tension or compression, as well as varying due to the shape of the sample [24,25]. These values also correlate very well with the sealability table from Chapter 2, as the lower stiffness indicates that the material should require far less force to seal when compared to their flat counterparts, which is exactly the trend seen in the sealability values. Furthermore, it seems that the various sources of inaccuracy that were present in the viscoelastic simulations of the flat gaskets were again present in these simulations as well. For example, in Figure 50, the load curve dropped more sharply in the beginning than the experimental force curve. Again, this can likely be fixed by increasing the number of coefficients, although this will come with increase computational cost as well. However, despite this relatively minor flaw, the model still had an accuracy of 0.845, which means it can be used to reliably model the behavior of these textured gaskets.

7.5 Comparisons and Possible Improvements

The modeling approaches were fairly different between the flat and textured gaskets. As expected, modeling the flat gaskets was rather more straightforward, requiring only a material definition and a rather fine mesh applied to the entire gasket body. In contrast,

modeling the textured gaskets proved to be challenging but possible. One of the main differences between the two types of simulations was the properties of the mesh in either case. As mentioned previously, the simulation of the flat gasket required a mesh with an average element volume of 0.01 in^3 to be applied to the entire gasket to get an accurate result. However, for the textured gaskets, the mesh elements had to have a max volume of 0.005 in^3 at the ridges and peaks, while the elements in the main body of the gasket could be slightly larger at 0.0075 in^3. The textured gaskets also required three mesh refinement loops that optimized the mesh throughout the simulation and deleted certain elements when they became unnecessary. These features of the mesh also allowed for the simulations to more easily and accurately cope with changes in contact status between the gaskets and the flange faces, as well as self-contact between different faces on the gasket. Ultimately, these changes helped avoid the mesh from becoming too distorted, thus allowing ANSYS to converge on a solution more easily.

Various other factors differed between the simulations for the two types of gaskets, especially with regards to the contact settings. For one thing, the contact type for the textured gaskets had to be changed from the nodal normal type to the nodal normal to target variety in order to better model changes in contact status. Also, in order to cope with the relatively higher levels of deformation seen in the peaks of the textured gasket, the contact stiffness had to be lowered from a factor of 1, as in the flat gasket simulations, to a factor of 0.04. This change allowed ANSYS to cope with the high levels of bending and deformation, thus resulting in an accurate solution. However, it should be noted that lowering the contact stiffness did result in increased levels of nodal-element penetration, which can often be a source of inaccuracy. Despite this, as the penetration between the gasket and the flange faces

had an average value of less than 1% of the displacement applied to the gasket, it is fair to say that the impacts of penetration on the model's accuracy are fairly limited. The differences listed here are by no means an exhaustive list, but serve as an overview of some of the most important factors that had to be changed between the treatment of the flat and textured gaskets.

Even though the modeling approaches differed quite a bit, there were several similarities between the results of the simulations for the flat gaskets and those for the textured gaskets. For one thing, the R^2 values for both types of gaskets seem to drift somewhere around 0.87. The sources for error seem to be the same as well. Both sets of simulations displayed load curves that dropped far more sharply than their experimental counterparts at the beginning while staying flatter towards the end. It should also be noted that in both types of simulations, the gaskets filled with barium sulfate were often easier for the model to simulate, leading to higher R^2 values for those types of gaskets.

There are several ways to improve this simulation approach and create a more robust and accurate model. One approach would be using more experimental data to create higher confidence averages for the Prony series and E(0) coefficients. This would improve the statistical robustness of the model, as by using a higher number of data curves to form the coefficients, the standard deviation in all sets of coefficients would be far lower, thus ensuring that the behavior seen in the simulations was not based on a series of outliers. Another method to improve the accuracy of the simulations would be to use more Prony series coefficients. This would help mitigate one of the sources of error seen in the simulated loads. Using more coefficients would likely help better capture the shape of the initial drop in load, as well as help reduce the flattening problem at higher times.

One of the simpler, but more time intensive methods that could be used to improve the model is to use longer duration tests to develop the Prony series constants. This would drastically improve the accuracy of the simulation over long intervals, as by having some of the Prony constants fix the shape of the curve at higher time intervals, the model could better account for how the load curves act at those times. Finally, one last improvement would be to use an anisotropic or orthotropic elasticity assumption, as the material behavior may be different depending on the direction of the material fibers. Until now, the model has been relying on an isotropic elasticity assumption but switching over to an anisotropic assumption would help the model be more realistic, and may help the model in future applications, as an anisotropic or orthotropic model would better capture the changes in material behavior due to temperature [26, 27]. Using any or all of these methods would likely improve the accuracy of the simulations, as well as the applicability of the model to CAE applications.

The ideal next step would be to progress the development of this framework so that it could be capable of the following. First, the material parameter definition would need to be done in such a way that by performing a deformation test on any flat gasket, material parameters could be extracted that are independent of thickness. Next, it would need to be verified that the constants derived from these tests can accurately model the force relaxation and deformation behavior of textured gaskets within a similar thickness range. Finally, the material model would need to be usable in various design optimization processes (e.g., Monte Carlo methods) to identify the optimal dimensions and shapes of a textured gasket that yield optimal sealability and conformability. This series of improvements would both improve the model's applicability to other types of gaskets as well as allow engineers to design better gaskets using advanced engineering tools.

CHAPTER 8 CONCLUSIONS

In this thesis, a framework was proposed to greatly improve the methods of designing and characterizing the properties of advanced gaskets. This method combined statistical and mechanical approaches and is able to characterize the behavior of various different types of PTFE gaskets under several different loading conditions. Despite the near universal usage of these gaskets in a variety of different conditions, the behavior of these gaskets on the meso-scale is still not very well understood. In this work, PTFE gaskets with various different characteristics and filler materials were used as a basis to create the model. A material database was established to collect and analyze the experimental data. Statistical methods were then used to determine the relevance of different factors on the efficiency of a gasket. It was found that the temperature of the flange is the most important factor affecting gasket efficiency, followed by the style. It was also found that the filler material had next to no impact on the performance of a gasket.

A Finite Element approach was also used to characterize gasket behavior. A series of load-deformation experiments were performed to get the required quantities for the model. A second database was established to analyze the stress-strain behavior of the materials for use in the model. Based on information gleaned from this series of experiments, a material model was created that relied on a Prony series approximation of Burger's model in ANSYS to simulate gasket loading and unloading behavior. The validity of this model was measured by comparing the simulated load data to the experimental load data. This model was found to be fairly accurate, with an average R2 value of 0.87 across all flat gaskets. The efficacy of the material model was also tested with regards to textured gaskets, where it produced similar

results. A combination of these approaches should help future engineers characterize and design better gaskets through the use of experiments and tools such as design optimization.

APPENDIX A DATA

Table 27: Summary of results for ambient temperature experiments

Test Variables					Output					
					Initial Torque			Retorque		
Specimen ID	Material	Style	Thickness, tg (in)	Dwell Times, t1-t2 (hr)	Peak Load (lb)	Relaxed Load (lb)	Area Under Curve (lb*s)	Peak Load (lb)	Relaxed Load (lb)	Area Under Curve (lb*s)
TB-01	3504	HX	-	1	14967.21	13649.95	42896594.43	14879.03	13744.26	594628590.45
TB-02	3504	HX	-	12	15091.26	13532.48	586989463.27	13532.53	13502.17	589071414.53
TB-03	3504	Legacy	1/8	1	14323.05	11752.18	37507917.58	13896.50	11856.04	520329180.62
TB-04	3504	Legacy	1/8	12	15861.82	13014.57	565797533.67	14045.47	12802.67	560012306.29
TB-05	3504	Legacy	1/16	1	17314.68	15404.60	52816259.96	15406.80	14757.44	642464986.70
TB-06	3504	Legacy	1/16	12	15910.13	15034.49	49971753.15	14984.33	14563.80	632251440.77
TB-07	3510	HX	-	1	16243.61	15041.63	48776654.53	15770.86	14819.00	646833471.20
TB-08	3510	HX	-	12	14878.76	13698.22	589927135.19	13695.48	13707.60	595887917.21
TB-09	3510	Legacy	1/8	1	15516.27	14034.17	44797541.32	15214.77	13758.44	603547985.20
TB-10	3510	Legacy	1/8	12	15256.52	13231.81	577265940.93	13976.61	13111.51	573475772.02
TB-11	3510	Legacy	1/16	1	16792.13	16509.28	53484412.82	16687.12	16474.14	712118097.92
TB-12	3510	Legacy	1/16	12	15790.49	15337.83	658768522.14	15473.67	15366.67	663780608.27
TB-01a	3504	HX	-	1	16663.98	15013.36	48227799.40	15422.94	14591.44	636935020.50
TB-02a	3504	HX	-	12	15163.10	13451.43	583141495.77	14083.95	13591.28	590544464.38
TB-03a	3504	Legacy	1/8	1	14156.36	12062.20	39316634.98	13536.30	11758.52	515599915.22
TB-04a	3504	Legacy	1/8	12	15910.94	14650.97	636212760.71	14775.33	14451.80	626705976.52
TB-05a	3504	Legacy	1/16	1	16269.50	15245.85	50517483.38	15489.94	14923.14	649099603.44
TB-06a	3504	Legacy	1/16	12	16189.80	15081.50	649851121.92	15366.70	15074.88	653378354.54
TB-07a	3510	HX	-	1	15105.60	13642.99	43188170.00	13849.28	13293.56	578367141.65
TB-08a	3510	HX	-	12	16868.08	14974.10	649801143.68	15073.34	14699.27	637545295.17

TB-09a	3510	Legacy	1/8	1	14790.56	13453.47	40212263.69	14396.23	13045.81	571857149.47
TB-10a	3510	Legacy	1/8	12	15366.56	13060.70	565774093.90	14721.58	13687.09	597895418.80
TB-11a	3510	Legacy	1/16	1	16272.52	16010.74	52920665.52	16179.06	16012.14	691651542.00
TB-12a	3510	Legacy	1/16	12	15764.80	15375.09	658988395.50	15434.42	15398.38	664266245.63
TB-01b	3504	HX	-	1	16005.07	14605.20	46594176.29	14958.04	14317.92	623355534.81
TB-02b	3504	HX	-	12	15282.15	13662.20	590769854.68	13916.11	13603.88	589919383.98
TB-03b	3504	Legacy	1/8	1	15415.85	13400.94	43613566.09	14185.74	12528.15	549163070.98
TB-04b	3504	Legacy	1/8	12	15548.80	12168.62	528411492.20	13996.17	12663.43	554975116.27
TB-05b	3504	Legacy	1/16	1	15135.07	14066.20	46541351.47	14315.07	13819.21	600631944.67
TB-06b	3504	Legacy	1/16	12	14860.65	13782.04	596260544.02	14181.00	13837.52	600390635.23
TB-07b	3510	HX	-	1	15880.35	14477.71	48217962.51	14602.31	13938.06	606557965.98
TB-08b	3510	HX	-	12	15717.86	13699.62	593861907.88	13897.31	13476.72	585474987.78
TB-09b	3510	Legacy	1/8	1	15416.38	13792.41	45390400.91	14412.92	13076.90	572887314.27
TB-10b	3510	Legacy	1/8	12	16162.14	13947.34	607077761.67	14396.80	13423.21	587833720.84
TB-11b	3510	Legacy	1/16	1	16061.98	15524.54	53168330.73	15550.43	15421.33	666067578.41
TB-12b	3510	Legacy	1/16	12	16003.66	15626.31	671396336.58	15704.13	15644.76	674625161.88
TB-01c	3504	HX	-	1	17024.15	15194.45	49217371.88	15281.17	14722.70	640505437.23
TB-02c	3504	HX	-	12	15923.89	13987.26	606479801.40	14270.00	13917.42	604381510.97
TB-03c	3504	Legacy	1/8	1	15175.02	12736.43	38661327.52	14893.93	13043.95	571037768.58
TB-04c	3504	Legacy	1/8	12	15880.81	13151.57	570534889.31	13936.18	12713.87	555811382.06
TB-05c	3504	Legacy	1/16	1	15819.51	14550.75	48633765.83	14708.24	14180.85	617119093.12
TB-06c	3504	Legacy	1/16	12	15018.96	13723.32	594172093.96	13976.08	13647.64	591807318.97
TB-07c	3510	HX	-	1	15804.84	14575.32	46848862.83	14977.98	14199.03	619027979.49
TB-08c	3510	HX	-	12	15910.49	13670.72	591109805.57	13821.12	13453.62	583907698.96
TB-09c	3510	Legacy	1/8	1	16137.82	14102.66	47025497.49	14532.44	13132.34	575542609.53
TB-10c	3510	Legacy	1/8	12	16111.76	13535.05	588701888.23	13858.84	12821.11	561579499.19
TB-11c	3510	Legacy	1/16	1	16170.47	15908.50	52132266.73	16038.26	15862.50	686209144.28

TB-12c	3510	Legacy	1/16	12	15839.46	15425.88	664289679.45	15462.70	15407.50	664507181.64
TB-01d	3504	HX	-	1	16244.76	14738.12	49857717.75	14989.36	14297.86	622049069.53
TB-02d	3504	HX	-	12	16549.34	14553.79	629461843.94	14693.36	14256.51	619560579.56
TB-03d	3504	Legacy	1/8	1	16814.79	14553.92	49090798.18	15053.58	13722.27	600251341.13
TB-04d	3504	Legacy	1/8	12	16246.45	13477.17	584868268.70	13944.85	12798.26	559113188.82
TB-05d	3504	Legacy	1/16	1	16140.70	14811.04	49814958.91	15127.33	14480.09	630115728.88
TB-06d	3504	Legacy	1/16	12	16184.23	14527.72	629393182.20	14672.16	14192.39	617311324.88
TB-07d	3510	HX	-	1	15804.91	14512.76	48183531.21	14631.36	14042.51	610838233.48
TB-08d	3510	HX	-	12	17593.97	15094.13	654624000.64	15487.17	14882.13	648616873.64
TB-09d	3510	Legacy	1/8	1	17035.12	14843.28	49566894.33	16270.39	14620.50	640293612.73
TB-10d	3510	Legacy	1/8	12	17153.83	14576.86	634319652.27	15168.05	14260.51	623440301.33
TB-11d	3510	Legacy	1/16	1	17330.12	16749.12	56068023.09	16825.57	16600.05	718419366.25
TB-12d	3510	Legacy	1/16	12	17295.53	16711.51	720482325.01	16804.52	16720.31	722288702.19
TB-01e	3504	HX	-	1	16858.56	14980.44	50128945.32	15661.41	14846.08	646271340.98
TB-02e	3504	HX	-	12	16908.65	14854.56	640958361.44	15011.64	14662.25	636127400.17
TB-03e	3504	Legacy	1/8	1	17130.16	14292.75	48496085.48	15499.81	14006.70	612409357.44
TB-04e	3504	Legacy	1/8	12	16073.76	13264.49	576478956.86	14653.99	13182.88	577678447.67
TB-05e	3504	Legacy	1/16	1	17088.30	15514.67	51591275.44	15639.93	14962.13	651518083.72
TB-06e	3504	Legacy	1/16	12	17102.30	15112.63	655227822.33	15785.85	15213.40	660870846.46
TB-07e	3510	HX	-	1	16936.37	15428.74	49790260.54	15499.47	14850.94	646261229.29
TB-08e	3510	HX	-	12	16937.31	14664.42	635069341.52	14926.96	14478.48	629101858.44
TB-09e	3510	Legacy	1/8	1	16727.31	14455.84	46642930.50	15809.46	14362.96	627410708.35
TB-10e	3510	Legacy	1/8	12	16571.26	14269.86	621044873.15	15106.33	13886.97	608299773.19
TB-11e	3510	Legacy	1/16	1	16967.73	16355.00	54142499.91	16403.63	16128.10	700193804.50
TB-12e	3510	Legacy	1/16	12	17162.59	16503.66	712309823.23	16646.94	16545.76	714137751.04

Table 28: Summary of results for elevated conditions experiments

Material	Style	Temperature (°F)	Pressure (psi)	Initial Max Average Load (lbs.)	Average Relaxed Load (lbs.)	Area under Curve (lbs.*s)
3504	3/32"	100	100	10034.2268	8755.515666	759456675.5
3504	3/32"	100	300	10023.79837	8665.32109	757605399.6
3504	3/32"	100	300	10134.57462	9065.110807	794440201
3504	3/32"	100	300	9864.823094	8451.994028	739041116.4
3504	3/32"	100	500	9807.503483	8349.753904	732064888.3
3504	3/32"	100	500	9475.525671	8117.080245	722233589.7
3504	3/32"	100	500	9413.396331	8518.769308	740491577.9
3504	3/32"	300	100	9107.966258	6577.131755	619291777.2
3504	3/32"	300	100	9101.183237	8351.824264	725751058.2
3504	3/32"	100	100	9163.139479	6442.456391	599958805.1
3504	3/32"	300	100	9288.369211	6894.716121	660534958
3504	3/32"	300	300	11174.94567	9469.288905	827263899.8
3504	3/32"	300	300	9541.959045	7673.17319	752570201
3504	3/32"	300	300	9295.59742	6687.114684	642218374
3504	3/32"	300	500	10390.5427	9514.753642	825709643.2
3504	3/32"	300	500	9973.704065	9126.942891	794198411.1
3504	3/32"	300	500	9574.501332	7435.086974	662073546.1
3504	3/32"	300	500	9013.929152	6414.965646	607259348.5
3504	3/32"	300	300	9286.737296	7656.558522	674314251.1
3504	3/32"	300	300	8764.804726	7021.645143	631338908
3504	3/32"	100	100	9456.335104	8267.479465	724531569.2
3504	3/32"	500	100	6064.331559	4564.302512	414212127.9
3504	3/32"	500	100	8391.045105	7791.988303	674856222.2
3504	3/32"	500	100	7622.647083	7122.234765	619492427.2
3504	3/32"	500	100	8006.867349	5844.035164	521991352.5
3504	3/32"	500	100	8546.756112	5622.775923	506632001.4
3504	3/32"	500	300	8243.533883	5927.550789	523706802.6
3510	3/32"	500	500	8818.315889	4619.631188	423093784.5
3510	3/32"	500	500	7033.867831	5853.831719	514228505.1
3510	3/32"	500	500	4731.317064	4427.716936	383122200
3510	3/32"	500	500	4671.206431	4137.111395	360470847.6
3510	3/32"	500	500	4720.907534	4593.090246	398182629.9
3510	3/32"	500	500	4784.202187	4200.249579	363669458.1
3510	3/32"	500	500	5895.023626	5026.153447	441274210.7
3510	3/32"	100	100	4241.500462	3442.175032	302473112.5
3510	3/32"	100	100	10491.52236	9023.035151	792275618
3510	3/32"	100	100	91830.60993	4577.187283	-4.14653E+11
3510	3/32"	100	100	7257.384111	4169.120636	671976508.9
3510	3/32"	100	100	92927.36634	92192.94179	7977173524

3510	3/32"	100	100	179383.722	90331.98749	7003438541
3510	3/32"	300	300	176648.9655	176648.5209	15262398718
3500	1/8"	100	500	4120.261274	3000.452443	263390414.1
3500	1/8"	100	500	3882.570307	3642.386501	315418848.8
3500	1/8"	100	500	3613.282608	3239.553905	287776125.2
3510	1/8"	100	500	4386.595092	4100.55847	356099464.5
3504	1/8"	100	500	6794.656221	6434.873175	564175265.7
3504	1/8"	100	500	2818.229582	2304.603691	205240978.1
3504	1/8"	100	500	4136.222247	3169.352783	283445513.6
3500	1/8"	300	500	5843.601283	4451.7855	424238214.2
3500	1/8"	300	500	3770.284901	3599.282113	313281552.2
3500	1/8"	300	500	2752.952714	2647.403813	229043819.1
3504	1/8"	300	500	5981.533952	4228.936654	381858327.8
3504	1/8"	300	500	2858.811581	2309.881978	204665378.7
3504	1/8"	300	500	3326.919836	2787.401707	247197365.7
3500	1/8"	300	500	4200.042634	4023.835407	348528119.8
3500	1/8"	500	500	3397.932142	3236.172489	280460690.9
3500	1/8"	500	500	3620.494995	3457.947774	299955768.5
3510	1/8"	500	500	4552.129248	3895.571348	339893653.4
3504	1/8"	500	500	2306.132813	1957.618421	173855045.8
3504	1/8"	500	500	3057.792998	2438.594646	217608311.5
3504	1/8"	500	500	3642.312544	3056.420485	270383095.8
3500	1/16"	100	500	4018.82893	3731.22343	325300732.3
3500	1/16"	100	500	2485.011868	2290.795025	200277251.6
3500	1/16"	100	500	2412.196286	2194.345596	192200862.3
3504	1/16"	100	500	3472.551912	3223.532848	281156139
3504	1/16"	100	500	2443.849248	2069.181066	183084623.1
3504	1/16"	100	500	2480.439078	2119.020669	187193668
3500	1/16"	300	500	3930.134118	3703.973597	323471729.7
3500	1/16"	300	500	2463.360602	2686.631448	226493073.2
3500	1/16"	300	500	2400.938973	2550.530668	216480663.8
3504	1/16"	300	500	3947.835673	3450.696268	303201011.5
3504	1/16"	300	500	3023.042071	2722.893753	237392078.7
3504	1/16"	300	500	2281.571432	2223.122684	191207582.7
3500	1/16"	500	500	3131.944628	3027.829151	262690267.8
3500	1/16"	500	500	2252.684719	2437.270106	207866441.8
3500	1/16"	500	500	2581.387532	2744.643248	232699069.7
3504	1/16"	500	500	4128.879237	3772.332539	329993830.2
3504	1/16"	500	500	2768.615122	2512.611189	218823025.2

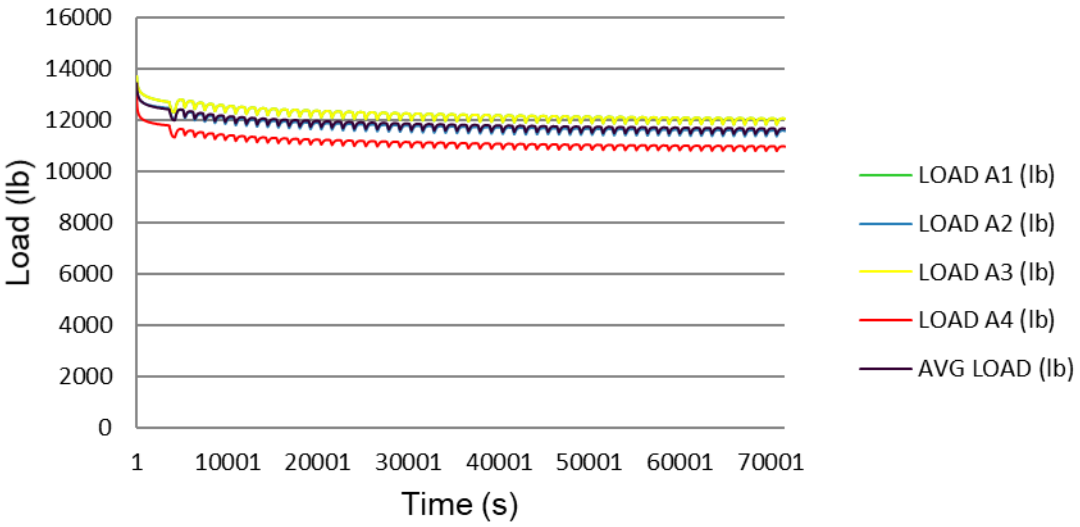

Figure 51: Load history for a textured blue gasket at 100F and 300 psi

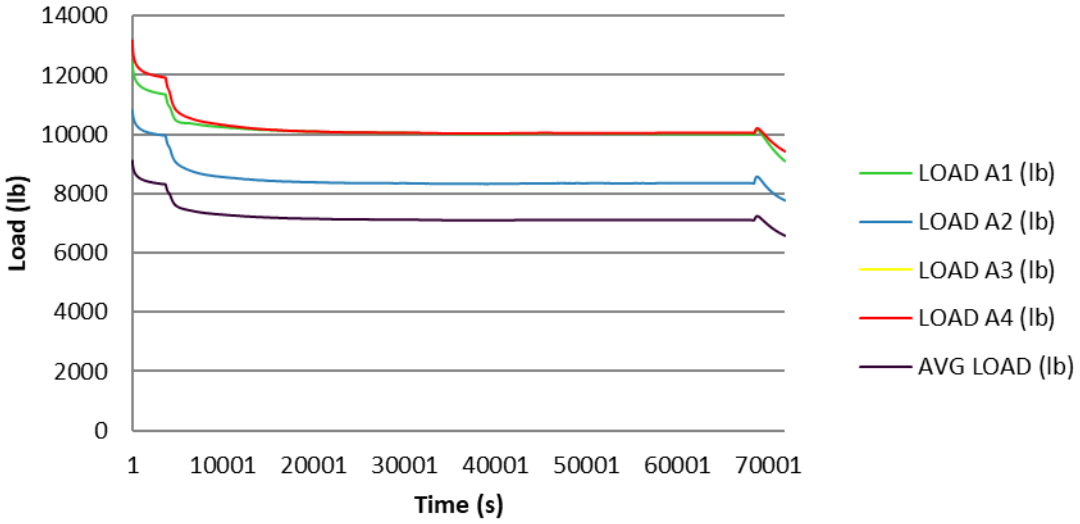

Figure 52:Load history for a textured blue gasket tested at 300F and 100 PSI

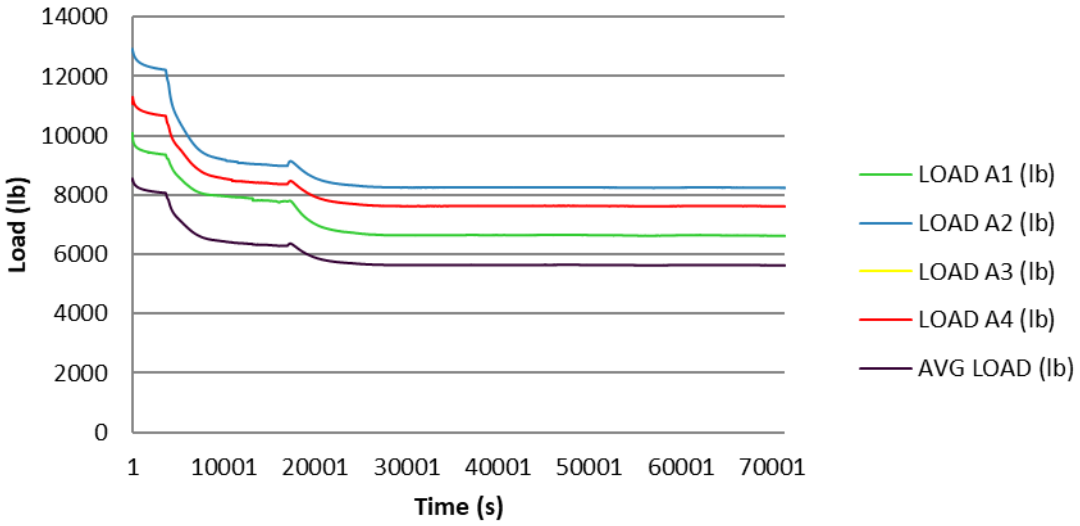

Figure 53: Load history for a textured blue gasket at 500F and 100 psi

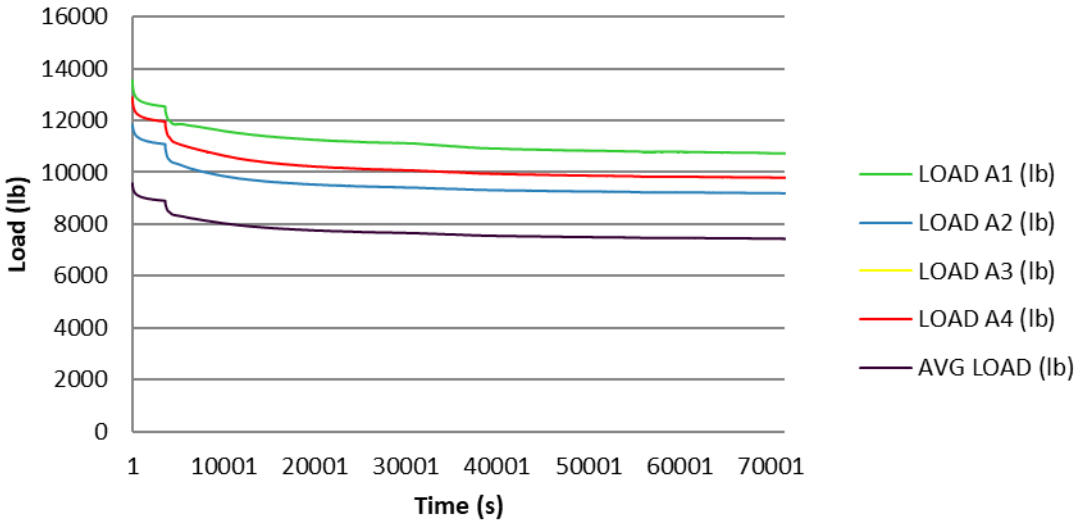

Figure 54:Load history for a textured white gasket at 300F and 500 psi

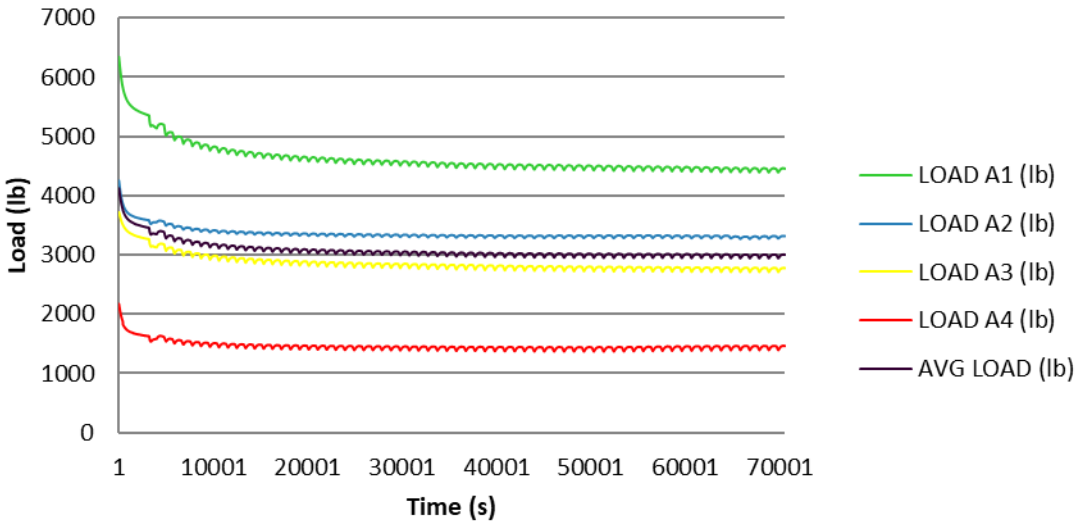

Figure 55: Load curve for a flat, 1/8" thick white gasket at 100F and 500 psi

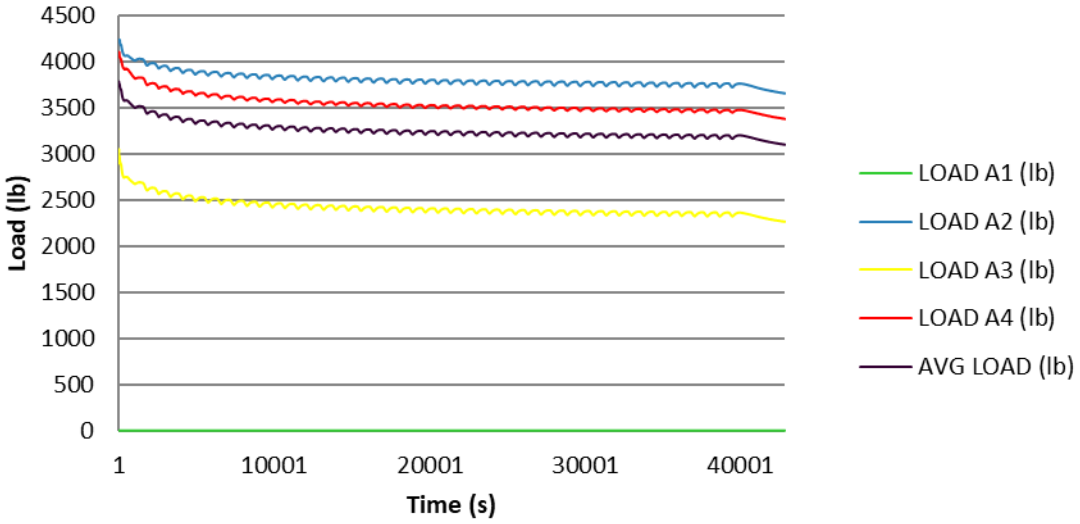

Figure 56: Load curve for a flat, 1/8" thick blue gasket at 100F and 500 psi

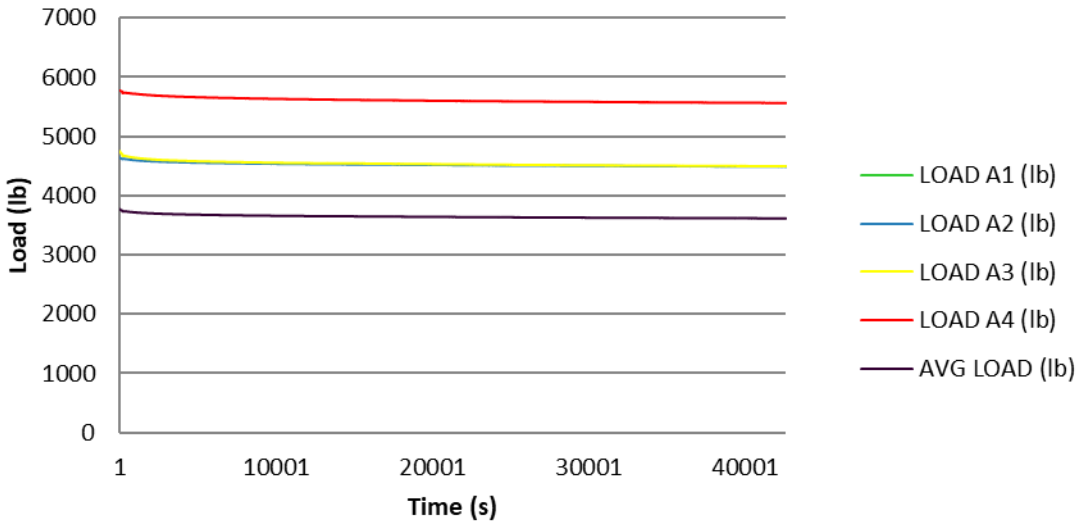

Figure 57: Load curve for a flat, 1/8" thick tan gasket at 100F and 500 psi

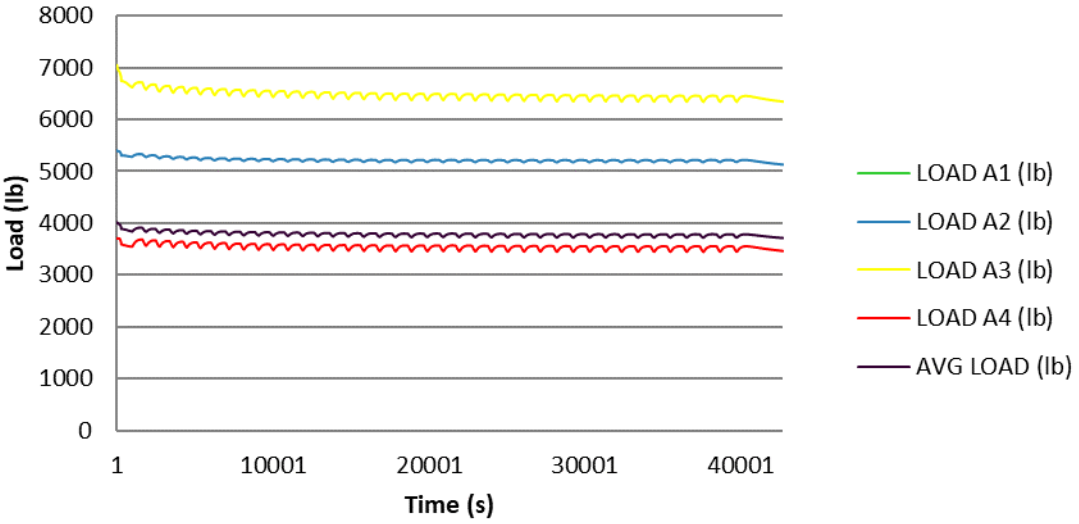

Figure 58: Load curve for a flat, 1/16" thick tan gasket at 100F and 500 psi

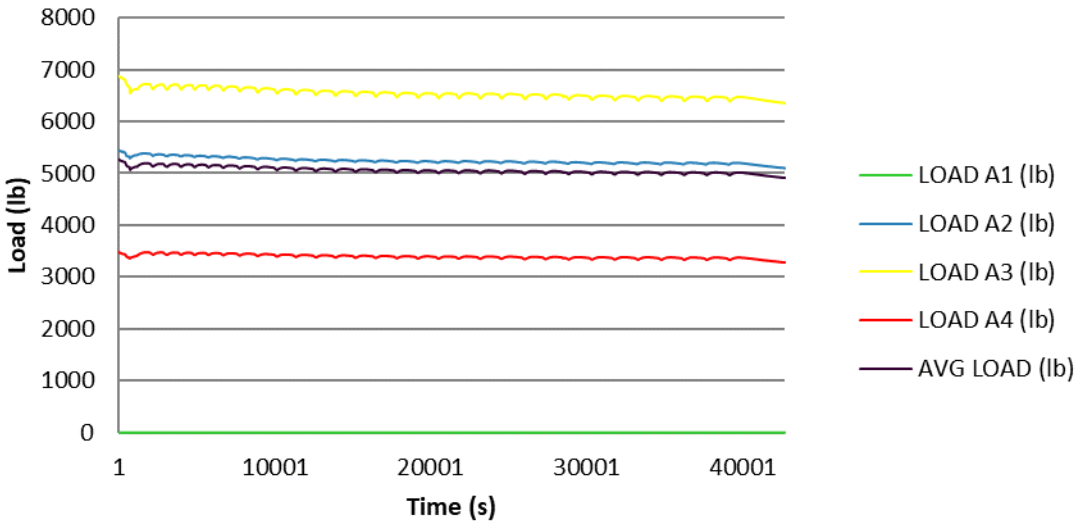

Figure 59: Load curve for a flat, 1/16" thick tan gasket at 300F and 500 psi

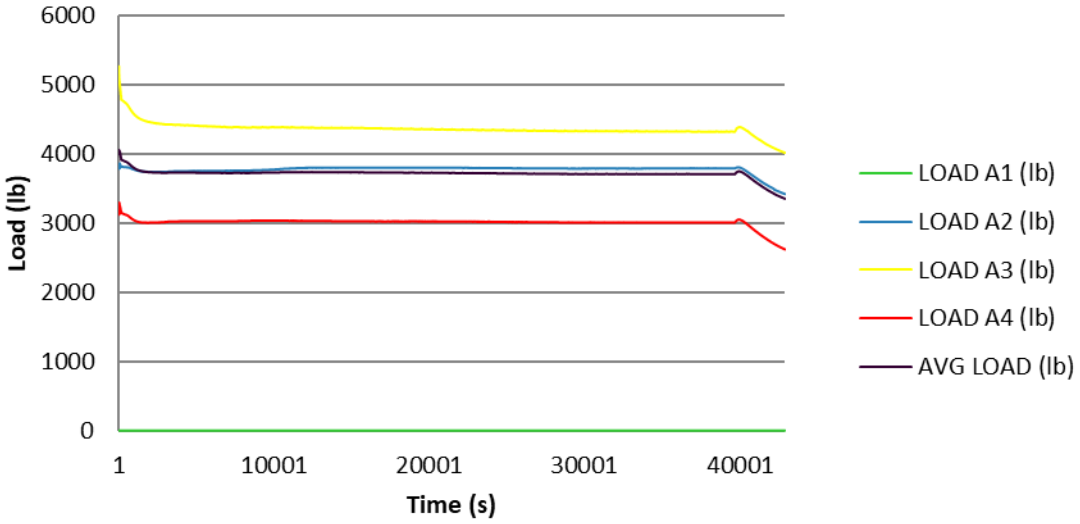

Figure 60: Load curve for a flat, 1/16" thick blue gasket at 300F and 500 psi

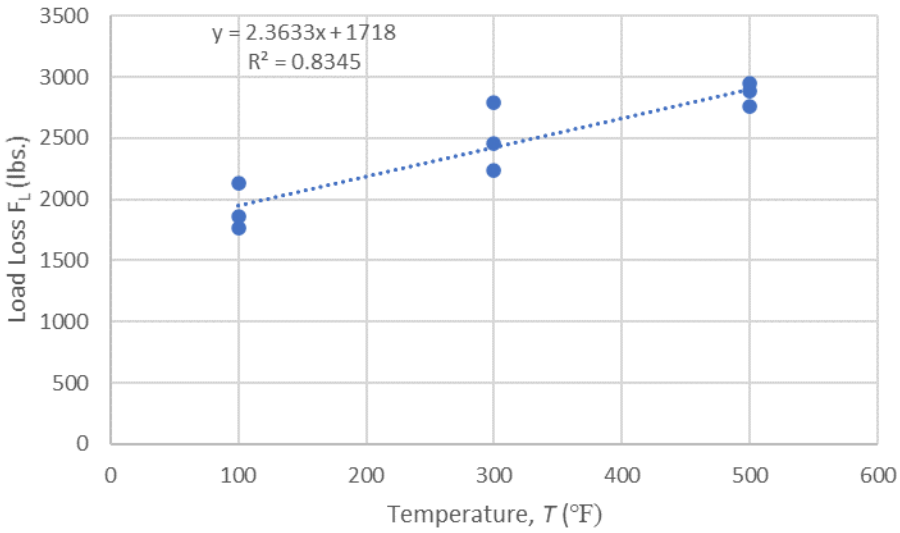

Figure 61: Load loss graph for white textured gasket at 100 psi

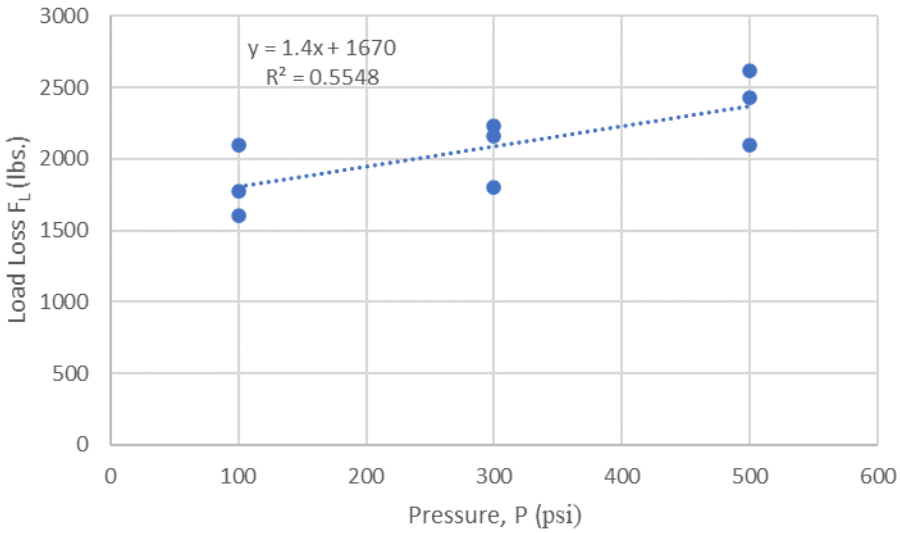

Figure 62: Load loss graph for white gasket at 100 F

APPENDIX B CODE

```
# -*- coding: utf-8 -*-

"""

Created on Wed Jan 13 16:18:15 2021



@author: sannm

"""

# Working ANOVA code(?)- needs more than one trial to be used, otherwise returns error.

#Can be used for any # of factor levels/ # of combinations

import pandas as pd

import researchpy as rp

import statsmodels.api as sm

from statsmodels.formula.api import ols



data1 = pd.read_csv("Data3.csv")

data1.info()

rp.summary_cat(data1[["Material", "Thickness", "Temperature"]])

rp.summary_cont(data1["E"])
```

```
model = ols("E ~ C(Material, Sum) + C(Thickness, Sum) + C(Temperature, Sum) + C(Material, Sum)*C(Thickness, Sum)*C(Temperature, Sum)", data=data1).fit()


aov_table = sm.stats.anova_lm(model, typ=2)

aov_table
```

APPENDIX C TECHNICAL DRAWINGS

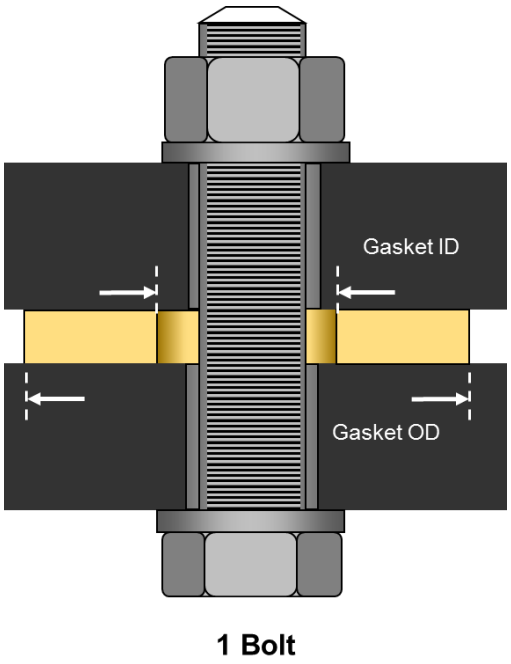

Figure 63: Sketch of relaxometer gasket creep test setup

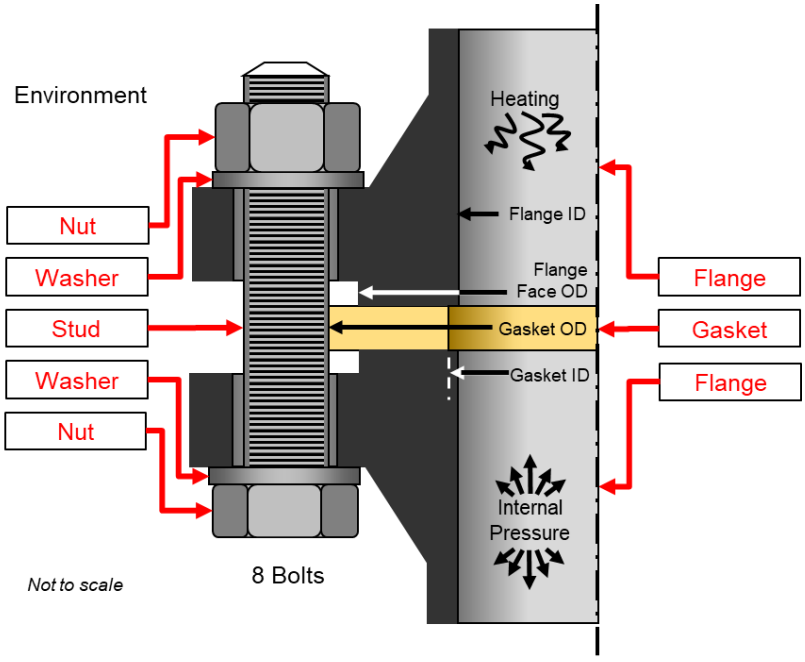

Figure 64: Sketch of enhanced test bed setup

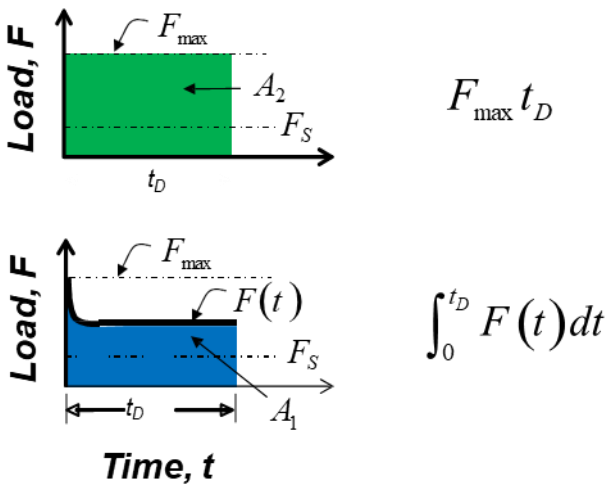

Figure 65: Efficiency diagram

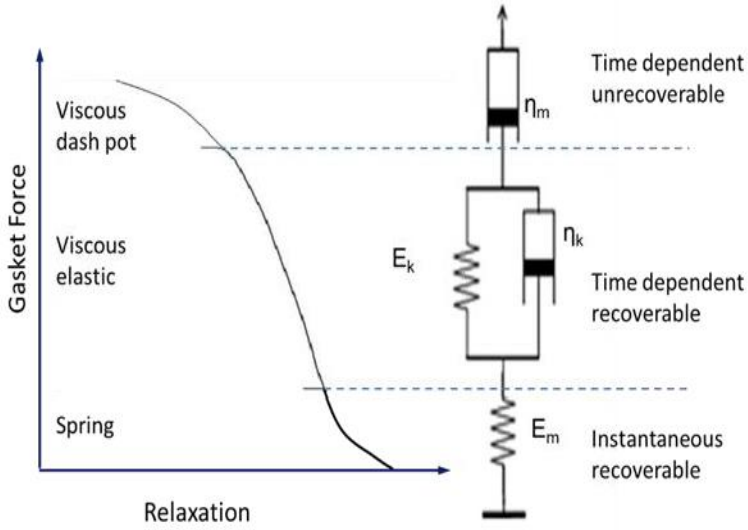

Figure 66: Viscoelasticity diagram

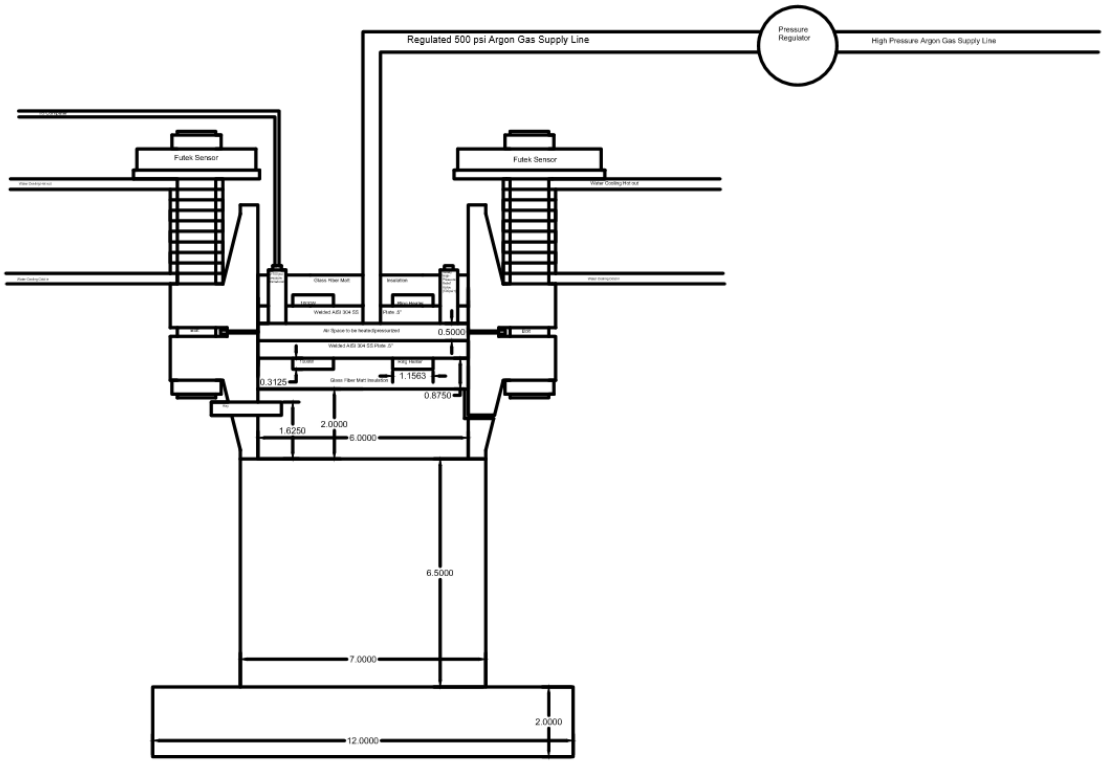

Figure 67: Schematic of upgraded test setup

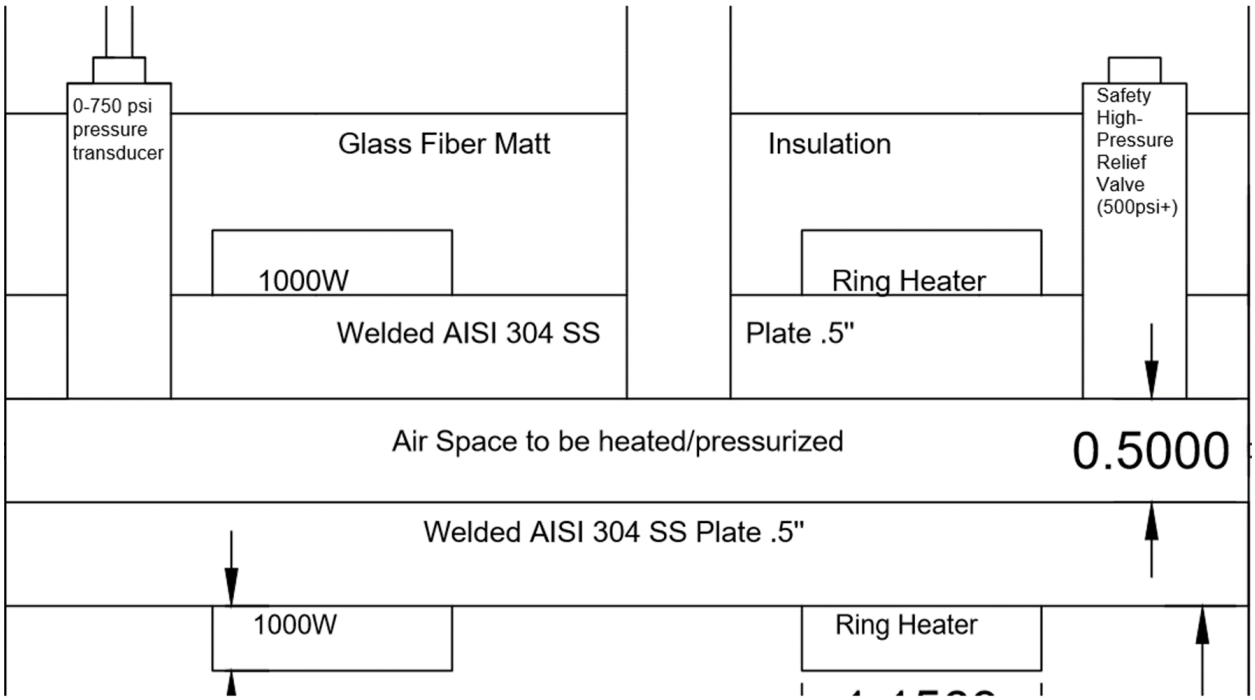

Figure 68: Schematic of heating and pressure elements of upgraded test setup

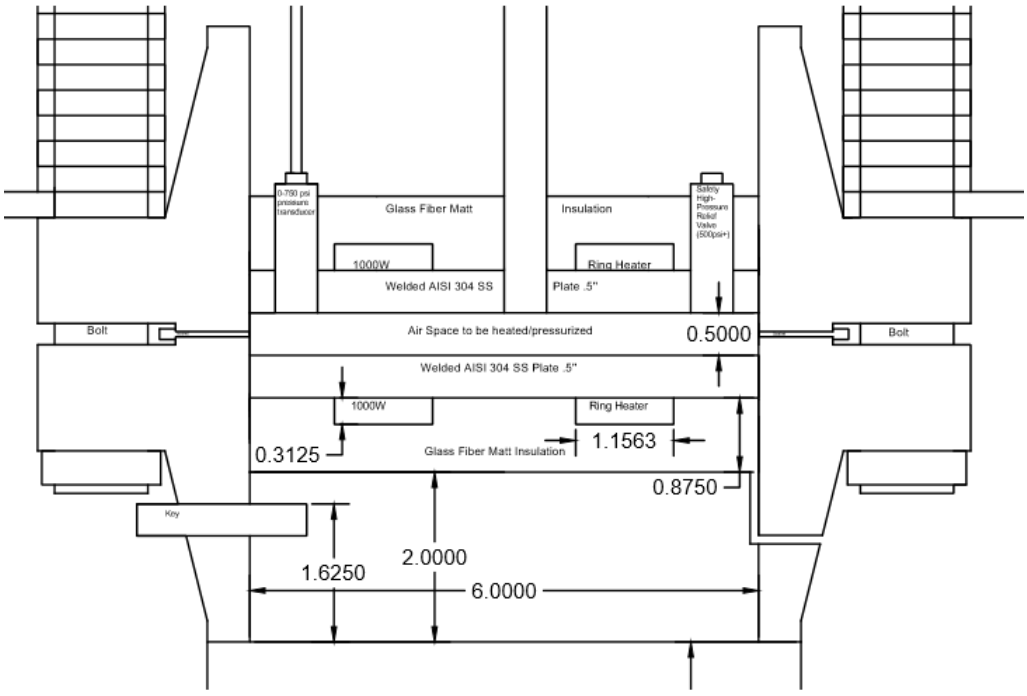

Figure 69: Schematic of bolted connection art of upgraded test setup

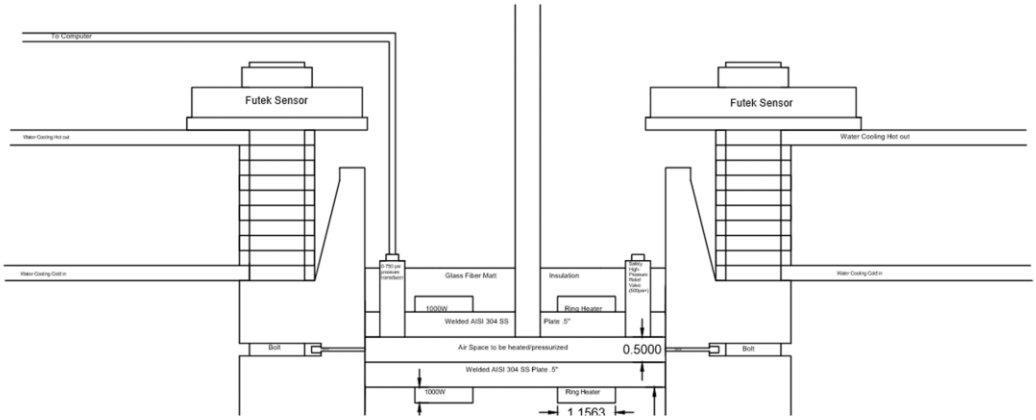

Figure 70: Schematic of load measuring instruments in upgraded test setup

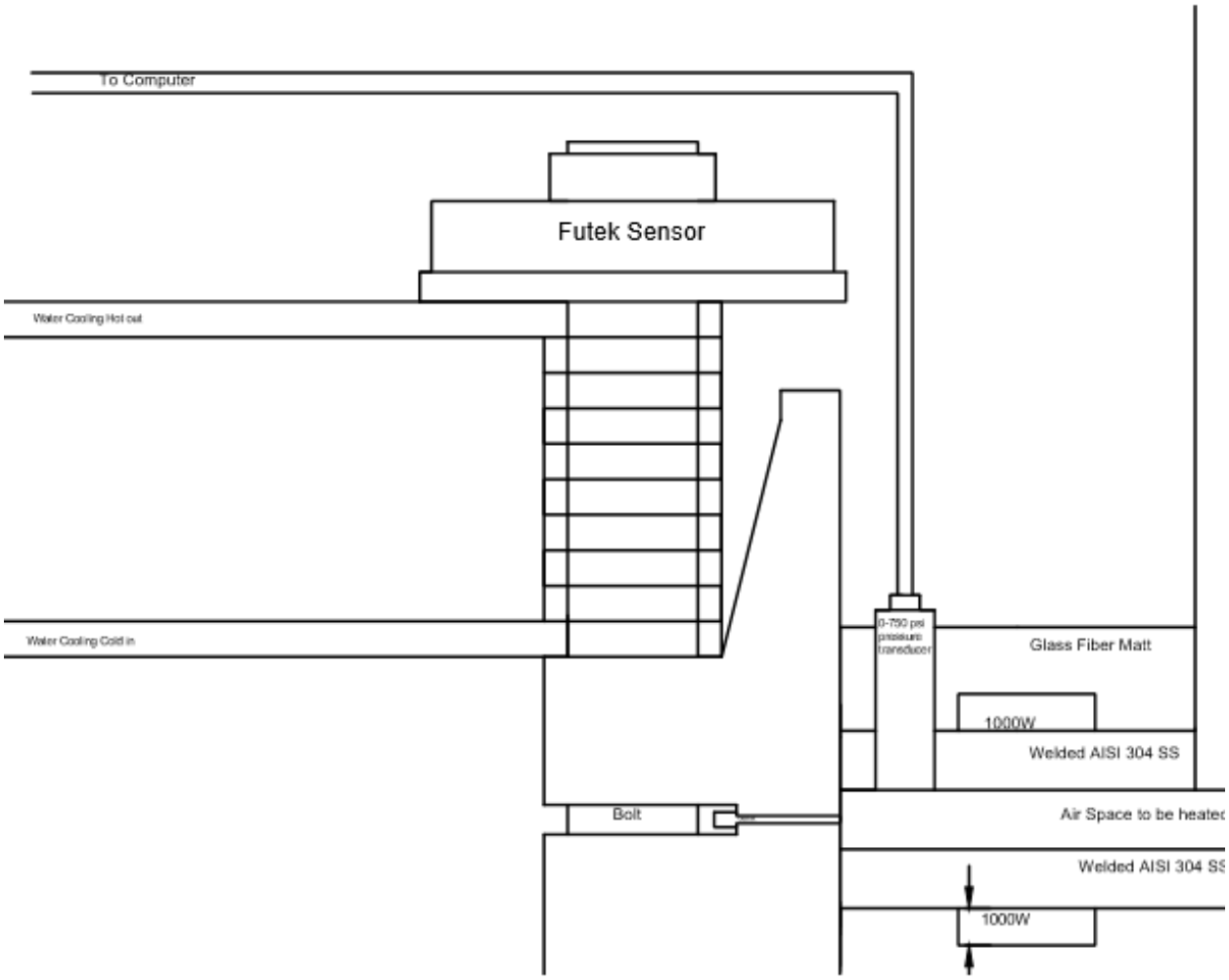

Figure 71: Close up view of test bolt load measurement setup

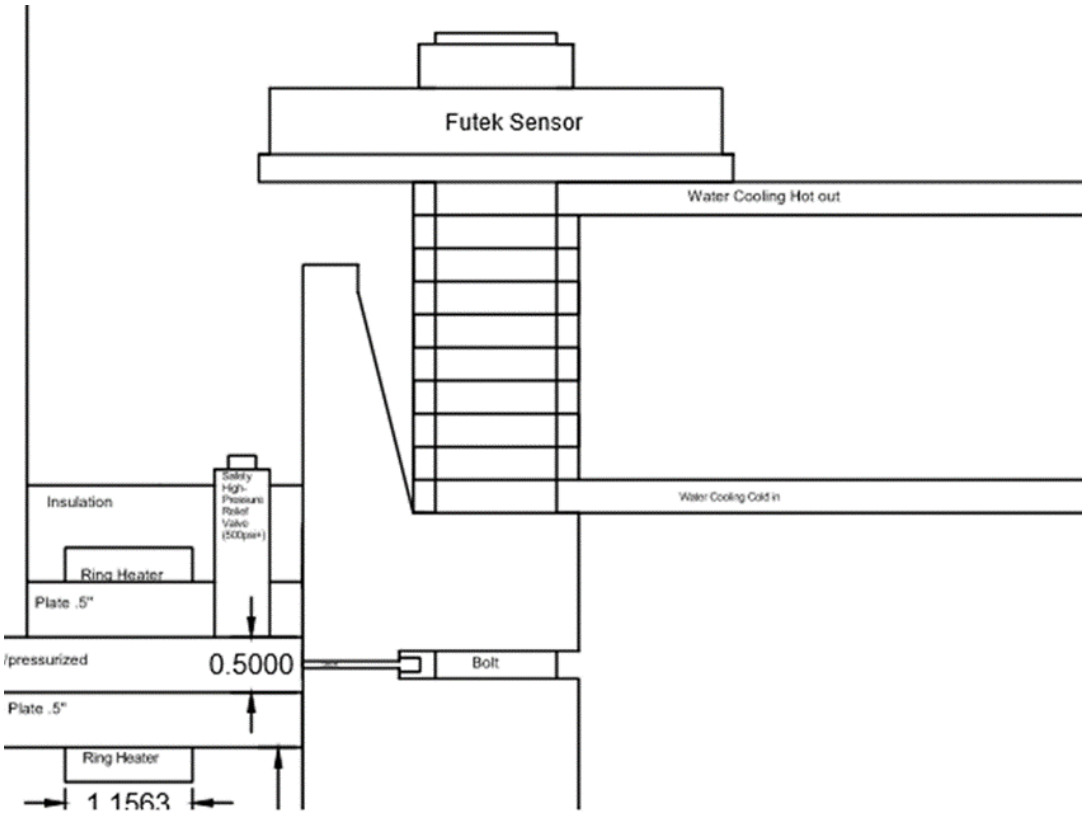

Figure 72: Closeup view of water cooling system

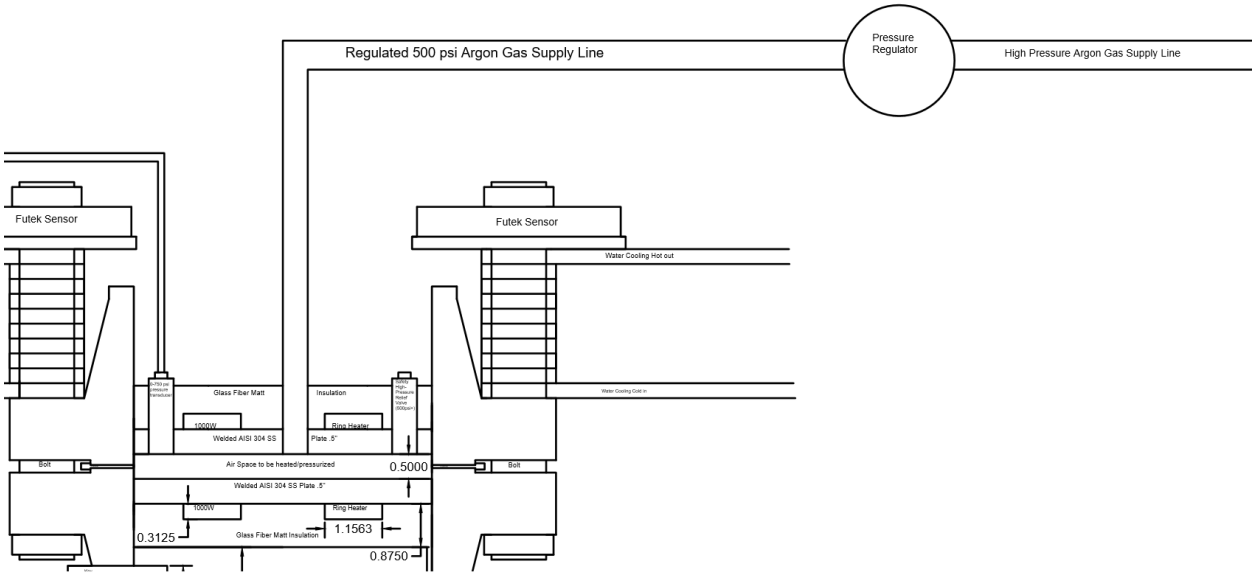

Figure 73: Schematic of pressure control system

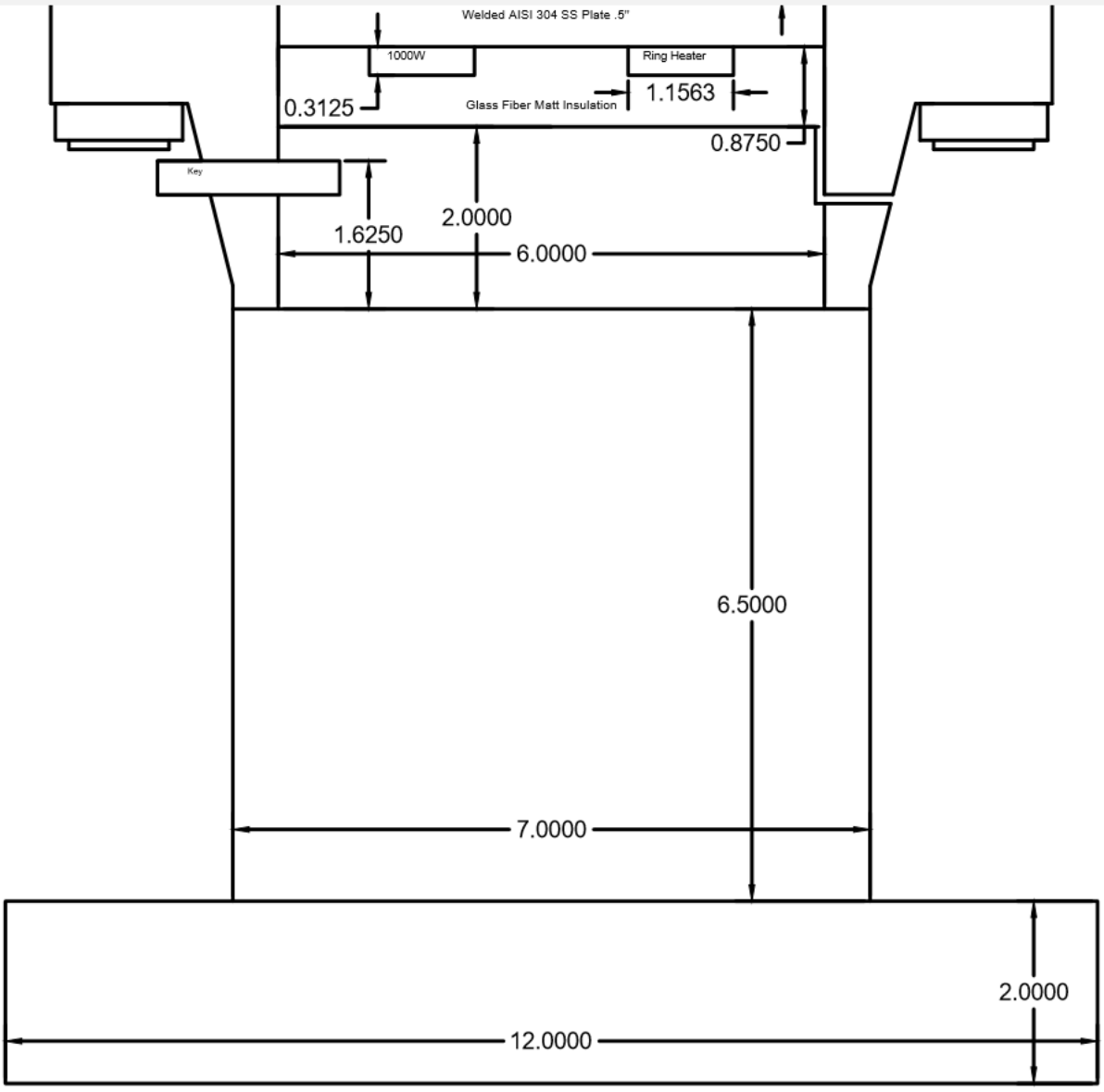

Figure 74: Schematic of flange base

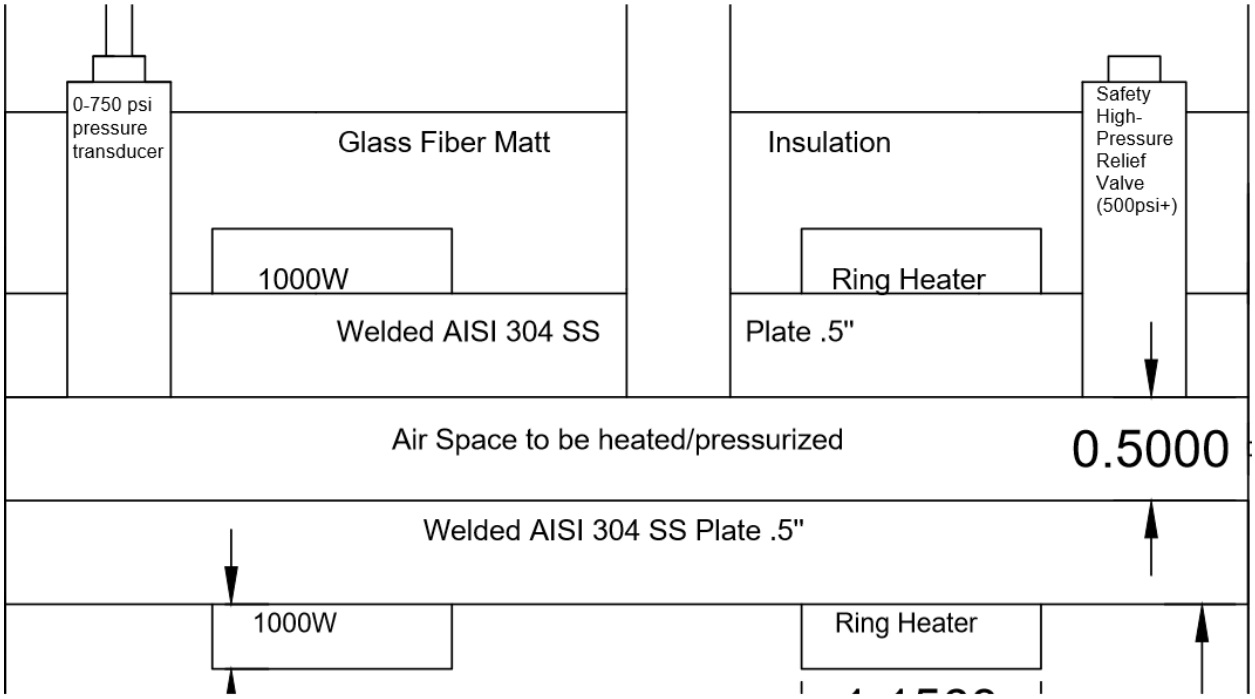

Figure 75: Close up view of top of flange

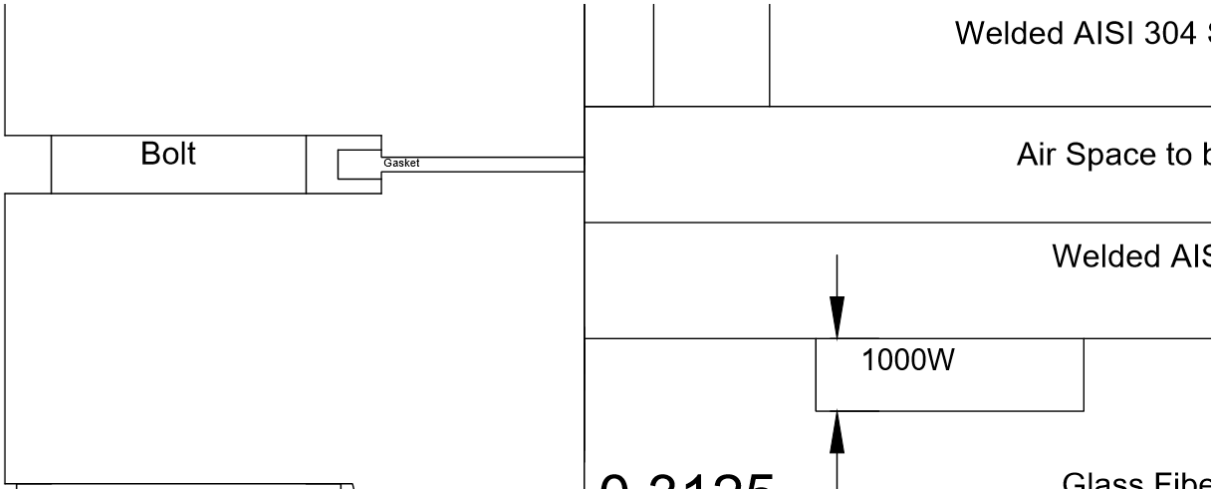

Figure 76: Close up view of gasket area

APPENDIX D SAMPLE CALCULATIONS

Efficiency:

This section will cover how to calculate the gasket efficiency. Calculating the efficiency relies on the load curves for the test and the efficiency equation.

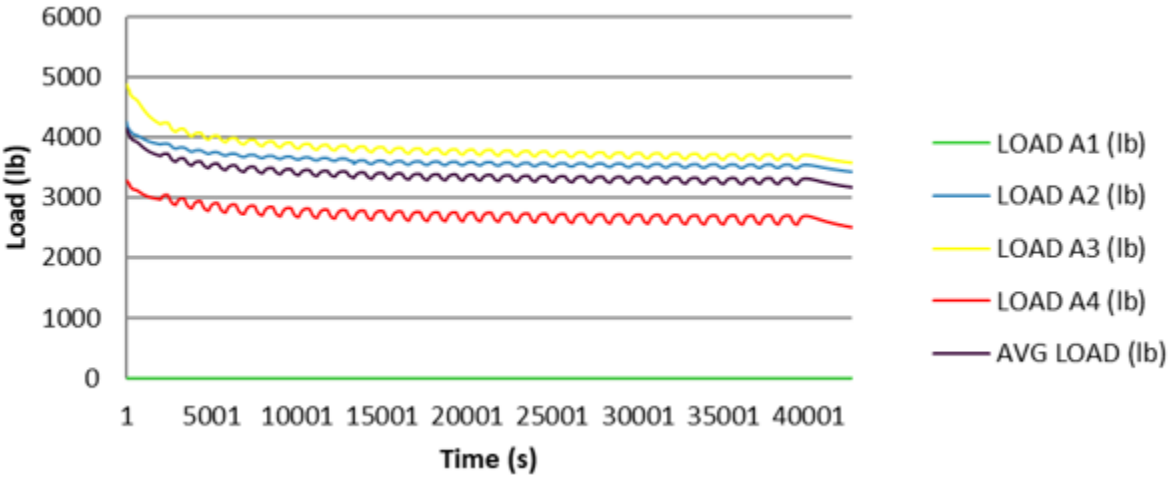

Figure 77: Sample load curve for efficiency calculations

$$\eta\% = \left(1 - \frac{F_{max} * t_d - \int_0^{t_d} F(t)dt}{t_d * (F_{max})}\right) * 100\%$$

The efficiency equation contains three separate variables that can be calculated from the load curve. The first is the average max load across all four load cells, F_{max}. The second is the dwell time t_D. The last term represents the area under the average load curve and is denoted by the integral term $\int_0^{t_d} F(t)dt$. Using these variables, the efficiency can be calculated.

F_{max} = 4300 lbs. (From the average load curve)

t_D = 42000 s (Constant)

$\int_0^{t_D} F(t)$ = 174150000 lbs.*s (Calculated from the average load curve)

$$\eta\% = \left(1 - \frac{(4300 * 42000) - 174500000}{(4300 * 42000)}\right) * 100\%$$

$$\eta\% = 87\%$$

Stress:

Calculating the stress on the gasket was necessary for creating the stress strain curves. The general normal stress equation was used. *F* is the applied force in lbs. and *A* is the cross sectional area (as seen from the top). For the following calculations, the force is set to an arbitrary value of 5000 lbs.

$$\sigma = \frac{F}{A}$$

F= 5000 lbs.

A = 1.075 in^2

$$\sigma = \frac{5000}{1.075}$$

$$\sigma = 4615.5\ psi$$

Strain:

Calculating the strain was also necessary for creating the stress strain curves. The general strain equation was used. Here, *L* is the initial gasket thickness in inches and *ΔL* is the deformation of the gasket. For the following calculations, *ΔL* is set to an arbitrary value of 0.032".

$$\varepsilon = \frac{\Delta L}{L}$$

L = 0.125 in

ΔL = 0.032 in

$$\varepsilon = \frac{0.032}{0.125}$$

$$\varepsilon = 0.256$$

Young's Modulus:

The stress and strain values calculated in the previous sections are plugged into the general elasticity equation to find the elastic modulus.

$$E = \frac{\sigma}{\varepsilon}$$

$$E = \frac{4615.5}{0.256}$$

$$E = 18462\ psi$$

Bulk Modulus:

The Young's modulus value is then plugged into the bulk modulus equation. Here, v is Poisson's ratio. The value used here is the average Poisson's ration for PTFE, 0.46.

$$K = \frac{E}{3 * (1 - 2v)}$$

v = 0.46

$$K = \frac{18462}{3 * \big(1 - (2 * 0.46)\big)}$$

$$K = 76925\ psi$$

Relative Contribution:

To find the relative contribution of a factor, the sum of squares for that factor is leveraged against the total sum of squares. Here, the contribution of the temperature variable will be calculated based on the results from Phase 3. The sum of squares values are shown in the table below.

Table 29: Sample ANOVA table

Source	*SS*	*df*	*MS*	*F*	*P*
Style (A)	0.0356	2	0.017	12.203	0.000
Material (B)	0.0056	1	0.005	3.825	0.058
Temperature (C)	0.1571	2	0.078	53.815	0.000
AB	0.0020	2	0.001	0.683	0.512
AC	0.0082	4	0.002	1.400	0.254
BC	0.0056	2	0.003	1.924	0.161
ABC	0.0035	4	0.001	0.602	0.663
Error	0.053	36	0.001		
Total	0.270	53			

$$\% = \frac{SSF}{SST} * 100$$

SS(Temperature) = 0.1571

SST = 0.270

$$\% = \frac{0.1571}{0.27} * 100$$

$$\% = 58.75\%$$

Thermal Expansion:

$\alpha=6.3*10^{-6}$

Length is limited to 1 inch as that is the contact length with the flange/load cells.

$$\Delta L = 6.3 * 10^{-6} * 500 = 0.00315"$$

Pressure vertical force:

P= 500 psi

D= 3.5”

$$F = \frac{P\pi D^2}{4} = 500 * \left(\pi * \frac{3.5^2}{4}\right) = 4810.56\ lbs.$$

Force per bolt:

$$F_B = \frac{F}{8} = \frac{4810.56}{8} = 601.32\ lbs.$$

REFERENCES

[1] ASTM (2006) “Standard Test Methods for Creep Relaxation of a Gasket Material (F-38)” American Society for Testing and Materials, West Conshohocken, PA.

[2] ASTM (1999) “Standard Test Method for Compressibility and Recovery of Gasket Materials (F-36)” American Society for Testing and Materials, West Conshohocken, PA.

[3] J. H. Bickford and H. Saunders, An Introduction to the Design and Behaviour of Bolted Joints, vol. 105. 1983.

[4] A. Y. Malkin and A. I. Isayev, “VISCOELASTICITY,” Rheol. Concepts, Methods, Appl., pp. 43–126, Jan. 2012, doi: 10.1016/B978-1-895198-49-2.50007-4.

[5] A. Alkelani, B. Housari, and S. Nassar, “A Proposed Model for Creep Relaxation of Soft Gaskets in Bolted Joints at Room Temperature,” J. Press. Vessel Technol. Asme - J Press. Vessel TECHNOL, vol. 130, Feb. 2008, doi: 10.1115/1.2826430.

[6] F. Stan and C. Fetecau, “Study of stress relaxation in polytetrafluoroethylene composites by cylindrical macroindentation,” Compos. Part B Eng., vol. 47, pp. 298–307, 2013, doi: 10.1016/j.compositesb.2012.11.008.

[7] Williams, J., and Gordon, A. P., (2015) “Constitutive Modeling of a Glass Fiber-Reinforced PTFE Gasketed-Joint Under a Re-torque” Characterization of Minerals, Metals, and Materials : 227-234.

[8] Bharadwaj, M., Claramunt, S., and Srinivasan, S. (2017) “Modeling Creep Relaxation of Polytetrafluorethylene Gaskets for Finite Element Analysis” International Journal of Materials, Mechanics, and Manufacturing, 5(2): 123-126

[9] Myers, J. L., and Well, A. D. (2003). *Research Design and Statistical Analysis*, 2nd Edition. Mahwah, New Jersey: Lawrence Erlbaum Associates, Inc.

[10] ASTM, A542/A542M-13 “Standard Specification for Pressure Vessel Plates, Alloy Steel, Quenched-and-Tempered, Chromium-Molybdenum, and Chromium-Molybdenum Vanadium” ASTM Book of Standards Volume 01.04, ASTM International, West Conshohocken, PA, 2013.

[11] P. J. Rae and D. M. Dattelbaum, “The Properties of Poly(tetrauoroethylene) (PTFE) in Compression,” 05.Lg, vol. 2035, Oct. 2004, doi: 10.1016/j.polymer.2004.08.064.

[12] Nassar, S., and Alkelani, A., 2006, “Clamp Load Loss due to Elastic Interaction and Gasket Creep Relaxation in Bolted Joints”, Journal of Pressure Vessel Technology, 128, pp.394-401.

[13] Waterland, A., F., and Frew, J. E. B. (2006) “Determination of Optimum Ambient Temperature Re-Torque Dwell Period for PTFE Based Gaskets” ASME Pressure Vessel and Piping Conference, Vancouver, British Columbia, CA, July 23rd-27th

[14] Williams, J. P., Shinde, S., and Gordon, A. P. (2017) “Gasket Relaxation and Re-Torque Optimization in Bolted Flange Systems” Glass Fiber-Reinforced PTFE Gasketed-Joint Under a Re-torque” Journal of Pressure Vessel Technology

[15] Gordon, A. P., Williams, J. P., and De Santiago, M. (2011) “Analytical Modeling of the Mechanics of Re-Torque” 2011 ASME Pressure Vessel and Piping (PVP) Conference, Baltimore, MD, July 17-21.

[16] Gordon, A. P., Drilling, B., Williams, K., Hebert, S., Kammerer, C. C., and Baldwin, F. (2011) “Optimization of Re-Torque and Relaxation Parameters of the GUCP” 2011 ASME Pressure Vessel and Piping (PVP) Conference, Baltimore, MD, July 17-21.

[17] Shinde, S., Gordon A.P., and Tasci E. (2018)“Combined Statistical-Mechanical Characterization of a Next Generation Textured PTFE for Extreme Environments”

[18] Williams, J., and Gordon, A. P., (2015) “Constitutive Modeling of a Glass Fiber-Reinforced PTFE Gasketed-Joint Under a Re-torque” Characterization of Minerals, Metals, and Materials : 227-234.

[19] L E Nielsen “Mechanical Properties of Polymers and Composites”, page 169, 2nd edition, Marcel Dekker, 1994

[20] “Thermal Degradation of Plastics,” Orangeburg, 2005.

[21] R. Loch, “PTFE - fluoroplastic, properties and characteristic data,” Velbert, 2001.

[22] P. H. Mott, J. R. Dorgan, and C. M. Roland, “The bulk modulus and Poisson’s ratio of ‘incompressible’ materials,” J. Sound Vib., vol. 312, no. 4–5, pp. 572–575, May 2008, doi: 10.1016/J.JSV.2008.01.026.

[23] Y. Rong, Y. Zheng, and H. Wang, “Contact Stiffness Study: Modelling and Identification,” in Finite Element Analysis - From Biomedical Applications to Industrial Developments, D. Moratal, Ed. Shanghai, 2012.

[24] K.S. Santhosh Kumar et al. European Polymer Journal, 43 2504–2514, (2007)

[25] K. Mazur, A. Gądek-Moszczak, A. Liber-Kneć, and S. Kuciel, “Mechanical Behavior and Morphological Study of Polytetrafluoroethylene (PTFE) Composites under Static and Cyclic Loading Condition,” Materials (Basel)., vol. 14, p. 1712, Mar. 2021, doi: 10.3390/ma14071712.

[26] S. V. Shil’ko, D. A. Chernous, and S. V. Panin, “TRANSFER PROCESSES IN RHEOLOGICAL MEDIA: METHOD OF DETERMINING THE THERMOVISCOELASTIC PARAMETERS OF POLYMERS AND ELASTOMERS,” vol. 87, no. 4, pp. 949–952, 2014.

[27] A. S. Nowick, B. S. Berry, and J. L. Katz, Anelastic relaxation in crystalline solids. 1975.